2D MXenes in the THz range: from optical conductivity to THz devices

by

Guangjiang Li

A Dissertation

Submitted to the Faculty of the

WORCESTER POLYTECHNIC INSTITUTE

in partial fulfillment of the requirements for the

Degree of Doctor of Philosophy

in

Physics

June 2021

APPROVED:

Professor Lyubov Titova, Advisor, Physics Department, WPI

Professor Douglas Petkie, Committee Member, Physics Department, WPI

Professor Yuxiang Liu, Committee Member, Mechanical Engineering, WPI

Professor Ronald Grimm, Committee Member, Department of Chemistry and Biochemistry, WPI

@ Copyright by *Guangjiang Li* 2021

All Rights Reserved

APPROVED:

Professor Lyubov Titova, ______________________________

Advisor Signature/Date

Physics Department, WPI

Professor Douglas Petkie, ______________________________

Committee Member, Signature/Date

Physics Department, WPI

Professor Yuxiang Liu, ______________________________

Committee Member, Signature/Date

Mechanical Engineering, WPI

Professor Ronald Grimm, ______________________________

Committee Member, Signature/Date

Department of Chemistry and Biochemistry, WPI

Acknowledgements

I would like to thank my advisor Professor Lyubov Titova for providing knowledge, guidance, and support during my PhD candidacy. She has passionately taught me how to be a qualified experimentalist, but also how to be a good scholar to accurately and efficiently express ideas with collaborators and other researchers. I was inspired by her to always keep a positive and cool mind, when encountering challenges in research and career. I cherish every opportunity to interact with her. The experience in Professor Titova's lab will continue to influence me in my future adventures.

I would like to express my appreciation to my lab mates Teng Shi, Kateryna Kushnir, and Erika Colin Ulloa for helping with experiments. I believe we have supported each other, inspired each other and learned from each other. Together we have overcome many experimental challenges, brainstormed for solutions and models, and successfully rebuilt our optics setup in our new lab. Still, I would like to take this opportunity to apologize to any misunderstandings due to culture differences, miscommunication etc. I enjoyed the physics department party at the end of the fall semester every year. I will miss playing basketball with Professor Qi Wen and listening to Jiazhang Chen playing piano. I will also miss listening to Edward Jarvis and Teagan Bate talking about food and cooking in Olin during lunch time. I admire Teagan's whistle too. I am grateful for the support from all of you when I was a TA. I feel like part of a big family here.

Special thanks to my dissertation committee members Professor Douglas T. Petkie, Professor Ronald Grimm and Professor Yuxiang Liu for reviewing and commenting on this thesis. Thank you Javery Mann and Andrew M. Fitzgerald for grammar correction.

I would like to thank our collaborators, Jacob Bouchard in Professor Douglas Pelkie's 5G/6G lab, Lite Zhou, Yan Tao, Maryam Masroor Shalmani, Binod Giri in Professor Pratap Rao's group and Julia L. Martin in Professor Ronald Grimm's group at WPI; Mengjing Wang, Kristie Koski from University of California, Davis; Yongchang Dong, Apparao M. Rao, Ramakrishna Podila from Clemson University; Shuohan Huang, Vadym Mochalin from Missouri University of Science and Technology; Varun Natu, Michel W. Barsoum, Kiana Montazeri, Mostafa K. Ismail, Bahram Nabet from Drexel University; Naaman Amer, David Purschke, Frank Hegmann from University Alberta, Canada, for providing samples and measurement support.

I appreciate Dr. Hassan Hafts and Professor Dmitry Turchinovich at the Max Planck Institute for Polymer (MPIP), Germany for hosting my intern research. This experience greatly extended my view of Terahertz research. I want to thank Peng Han, Eduard Unger, Keno L. Krewer， Wentao Zhang, Shumei Sun, Xiaoyu Jia, Xiaomin Liu who made my life in Mainz so enjoyable. I have expressed my deepest sympathy to the death of Eduard Unger, with whom we have very helpful discussion on understanding the Terahertz experimental principles.

I acknowledge WPI graduate student travel award, physics department of WPI for supporting my conference attendance, WPI PhD global research experience award for funding visiting research at MPIP. Special thanks to the Backlin Fund for supporting me to complete this dissertation.

Finally, with all my heart, I am deeply grateful to my father Huaimin Li, my mother Yuzhen Tian, my brother Guanghe Li. No matter how far from home, I always feel beloved and inspired by your passion, persistence of life and work.

Contents

Abstract 9

List of Figures 10

1 Introduction and background 23

1.1 Two-dimensional MXenes 23

1.1.1 Electrical properties of MXene 25

1.1.2 Optical properties and applications of MXenes 27

1.2 THz spectroscopy 31

1.2.1 THz electromagnetic radiation 31

1.2.2 THz time domain spectroscopy (THz-TDS) 35

1.2.3 THz conductivity models 37

1.2.4 Optical pump THz probe (OPTP) spectroscopy 41

2 THz study of 2D $Ti_3C_2T_z$ MXenes: intrinsic conductivity and photoexcited carrier dynamics 45

2.1 Introduction: 45

2.2 Fabrication and characterization of $Ti_3C_2T_z$ film 46

2.3 Intrinsic conductivity of $Ti_3C_2T_z$ film by THz-TDS 48

2.4 Photoexcited carrier dynamics of $Ti_3C_2T_z$ film measured by OPTP 51

2.5 Temperature dependent THz spectroscopy on photoexcited conductivity suppression of $Ti_3C_2T_z$ film 56

2.6 Conclusion 60

3 Equilibrium and non-equilibrium free carrier dynamics in 2D Mo-MXenes: $Mo_2Ti_2C_3T_z$ and $Mo_2TiC_2T_z$ 62

3.1 Introduction: 62

3.2 Mo-MXene film fabrication 67

3.3 THz TDS: intrinsic microscopic conductivity 69

3.4 OPTP: effect of photoexcitation on microscopic conductivity..... 73

3.5 Summary and Conclusions 83

4 Applications of MXenes in THz devices 86

4.1 Optical controllable EMI shielding... 86

4.2 THz Polarizers Based on 2D $Ti_3C_2T_z$ MXene 90

4.2.1 Synthesis of $Ti_3C_2T_z$ Colloidal Suspension and Pattern Production using Photolithography 91

4.2.2 Performance test: Extinction ratio and insertion loss 94

4.2.3 FDTD Simulation of $Ti_3C_2T_z$ MXene based THz polarizers on Comsol 99

4.2.4 Conclusion 104

5 Future Work and Conclusions... 106

5.1 Development of an intense THz source and Preliminary data: Nonlinear THz spectroscopy of MXenes... 106

5.2 Conclusions 114

6 Reference.. 118

Abstract

MXenes are a family of 2D transition metal carbides, carbonitrides and nitrides that are fabricated from layered MAX phases by etching out the A element, typically aluminum. Since the discovery of the first MXene, $Ti_3C_2T_z$, in 2011, MXenes have shown highly attractive properties such as high conductivity, record volumetric capacity, efficient light-to-heat conversion, saturable optical absorption, and others. Their chemical diversity and hydrophilicity facilitate the realization of novel optoelectronic and nanophotonic applications such as supercapacitors, electromagnetic interference (EMI) shielding, transparent conducting electrodes, and mode-locked fiber lasers MXene-based applications and further commercialization require understanding of the electronic and optical properties of MXenes as a function of their chemistry and structure. In many cases, applications call for nanometer to micrometer-thick MXene films that consist of multiple overlapping single-layer flakes. Conventional electrical transport measurement could only yield the overall conductivity of the MXene film. Terahertz (THz) spectroscopy enables probing carrier transport over microscopic distances, decoupling the inter- and intra-nanoflakes contributions and providing insight necessary to engineer and optimize their structure and morphologies for specific applications. Here, ***we use time-resolved THz spectroscopy to systematically study the carrier dynamics and photoexcitation of three MXenes: $Ti_3C_2T_z$, $Mo_2Ti_2C_3T_z$ and $Mo_2TiC_2T_z$. Based on the properties of MXenes in the THz range, we propose their applications in THz photonic devices, an optically-switchable THz EMI shielding and MXene-based THz polarizer. Finally, our first measurements of saturable absorption of $Ti_3C_2T_z$ in the THz range suggest that MXenes can be used in nonlinear THz photonics.***

List of Figures

Figure 1-1 (a) to (i) MXene taxonomy. (j) Potential MXene compositions. Compositions colored blue, that number 30, have already been synthesized. For ordered solid solutions, i-MXene stands for in-plane, and o-MXene – for out-of-plane order. Figure courtesy M. Barsoum. 24

Figure 1-2 Schematic for the exfoliation process of MAX phases and formation of MXenes. Reprinted with permission from [1]. Copyright (2012) American Chemical Society. 24

Figure 1-3 Secondary electron scanning electron microscope (SEM) micrographs for (A) Ti_3AlC_2 particle before treatment, which is typical of unreacted MAX phases, (B) Ti_3AlC_2 after HF treatment. Reprinted with permission from [17]. Copyright (2012) American Chemical Society. 25

Figure 1-4 a–c) Procedure for preparing $Ti_3C_2T_z$ thin films with varying thicknesses (≈5–67 nm) on glass and Si substrates via the interfacial film formation technique. d) The optical photograph shows transparent $Ti_3C_2T_z$ film (right side) uniformly covering a large area of 1 × 1 cm^2 glass substrates. Bare uncoated glass slide is shown on the left for comparison. Reprinted with permission from [15]. © 2018 WILEY-VCH Verlag GmbH & Co. KGaA, Weinheim. 25

Figure 1-5 UV-VIS optical transmittance of a 25 nm thick $Ti_3C_2T_z$ film (Data taken by thesis author at MAX Plank Institute for Polymer research, 2018) (Reprinted with permission from [4], Copyright (2019) American Chemical Society) 28

Figure 1-6 THz waveforms in nitrogen environment based on ZnTe (right)/$LiNbO_3$ (left) crystals pumped with 800 nm femtosecond laser (Data taken by thesis author at MAX Plank Institute for Polymer research, 2018) 33

Figure 1-7 (a) The generated THz phase front (dashed black bold line) in the $LiNbO_3$ crystal is matched parallelly with the tilted intensity front of the 800 nm pump pulse (bold red line), (b) $LiNbO_3$ crystal based intense THz source schematic diagram. 35

Figure 1-8 THz-TDS schematic diagram, where A: femtosecond laser, B: beam splitter, C: optical chopper, D: photodetector, M: Mirror, PM: parabolic mirror, PM': parabolic mirror with a hole, TM: THz mirror, L: Lock-in amplifier, T: translational stage, 1/4: quarter waveplate, WP: Wollaston prism, PC: computer 36

Figure 1-9 (a) THz-TDS waveform transmitted through a quartz substrate and through the substrate with a $Ti_3C_2T_z$ film. (b) Frequency domain spectroscopy obtained by FFT. (c) complex THz conductivity (solid symbols represent real and open symbols imaginary conductivity components; lines show a global fit of both components to the Drude-Smith model which is discussed later in section 1.2.3. (Adapted with permission from [4], Copyright (2019) American Chemical Society) 37

Figure 1-10 OPTP schematic diagram, where A: femtosecond laser, B: beam splitter, C: optical chopper, D: photodetector, M: Mirror, PM: parabolic mirror, PM': parabolic mirror with a hole, TM: THz mirror, L: Lock-in amplifier, T:

translational stage, 1/4: quarter waveplate, WP: Wollaston prism, PC: computer 41

Figure 1-11 Decay curves of photoinduced changes in complex THz conductivity in $Mo_2Ti_2C_3T_z$ and $Ti_3C_2T_z$ after excitation with 100 fs, 800 nm pulses. Here, the conductivity of in $Mo_2Ti_2C_3T_z$ is enhanced while the conductivity of $Ti_3C_2T_z$ is suppressed. 42

Figure 1-12 Photoinduced changes in complex THz conductivity in $Mo_2Ti_2C_3T_z$ at 5 ps after excitation with ~256 μJ/cm^2, 100 fs, 800 nm pulse. Lines are fits of experimental data to the Drude–Smith model. Adapted with permission from [4], Copyright (2019) American Chemical Society 43

Figure 2-1(a) chemical structure of $Ti_3C_2T_z$ (b) 2 μm by 2 μm AFM image (c) Profilometer (P-7 stylus profiler, KLA Tencor) scan over a region where the film was removed down to the substrate. Average film thickness is 25 nm. Adapted with permission from [4], Copyright (2019) American Chemical Society 47

Figure 2-2 (a) XPS survey for $Ti_3C_2T_z$ MXene. High-resolution XPS spectra of $Ti_3C_2T_z$ MXene for (b) Ti 2p and (c) O 1s. Adapted with permission from [22], Copyright (2019) American Chemical Society 48

Figure 2-3 2 μm by 2 μm AFM images of sample 1 (a) (fabricated by Yunchang Dong from Clemson Univercity) and sample 2 (b), where sample 2 is more continuous. It is consistent with c factor fitted from THz conductivity. (c), (d) are experimental conductivity spectra for samples 1 and 2 (symbols), along with their fits to the Drude-Smith model (Eq. 11). Adapted with permission from [4], Copyright (2019) American Chemical Society 50

Figure 2-4 (a) Photoinduced change in the THz peak transmission as a function of time after photoexcitation with 800 nm (a, b) and 400 nm (c, d) pulses with excitation fluence values given in the legends. Panels (b) and (d) show expanded views of the initial decay profiles in (a) and (c). Thick solid lines are fits of the experimental data to the multi-exponential decays. (Data taken by thesis author at MAX Plank Institute for Polymer research, 2018) Reprinted with permission from [4], Copyright (2019) American Chemical Society 51

Figure 2-5 Photoinduced change in real (solid symbols) and imaginary (open symbols) conductivity as different times after excitation with 800 nm, 950 μJ/cm^{2}pulse at 290 K. (Data taken by thesis author at MAX Plank Institute for Polymer research, 2018) Reprinted with permission from [4], Copyright (2019) American Chemical Society 52

Figure 2-6 Fitting parameters resulting from fitting transient photoinduced THz probe peak transmission enhancement to a three exponential decay function: peak and decay times for 800 nm excitation (left, red symbols) and 400 nm excitation (right, blue symbols). Reprinted with permission from [4], Copyright (2019) American Chemical Society.. 53

Figure 2-7 Complex THz conductivity (solid symbols represent real and open symbols – imaginary conductivity components; lines show a global fit of both components to the Drude-Smith model) at 290 K (red) and 95 K (blue). (Data taken by Naaman Amer at University of Alberta) Reprinted with permission from [4], Copyright (2019) American Chemical Society... 57

Figure 2-8 Transient change in transmission of THz probe pulse peak after excitation with 800 nm, 950 μJ/cm^{2}pulse at 290 K and 95 K. (Data taken by Naaman Amer at University of Alberta) Reprinted with permission from [4], Copyright (2019) American Chemical Society 57

Figure 3-1. Schematic depiction of (a) Mo_2TiC_2Tz and (b) $Mo_2Ti_2C_3T_z$ structure. (c) Effect of vacuum annealing on a film structure and inter-nanosheet distance. Reprinted with permission from [3], Copyright (2020) American Chemical Society 65

Figure 3-2 Representative SEM images for (a) spin coated $Mo_2Ti_2C_3T_z$ and (b, c) drop case $Mo_2TiC_2T_z$ films. For each sample, multiple images were analyzed and the average thickness was determined to be 80 ± 20 nm for $Mo_2Ti_2C_3T_z$ and 1300 ± 500 nm for $Mo_2TiC_2T_z$. Reprinted with permission from [3], Copyright (2020) American Chemical Society 67

Figure 3-3 XRD diffraction patterns of Mo-based films before and after annealing at 200 °C. Reprinted with permission from [3], Copyright (2020) American Chemical Society.. 68

Figure 3-4 UV-VIS spectroscopy of MXene films. Optical penetration depth at 800 nm was used in TRTS analysis to estimate the photoexcited layer thickness. For the Mo2Ti2C3Tz film, the optical penetration depth is larger than the average film thickness, and therefore the film thickness was used. Reprinted with permission from [3], Copyright (2020) American Chemical Society 68

Figure 3-5 (a) Probing motion of photoexcited carriers in the $Mo_2Ti_2C_3T_z$ MXene nanosheet by THz probe pulses. (b) THz waveforms transmitted through the substrate, through a MXene film on a quartz substrate, and the photoinduced change in the transmitted waveform 2 ps after excitation with ~ 256 μJ/cm^2, 800 nm pulse. Comparing in the frequency domain the magnitude and phase (c) of THz pulses transmitted through the substrate with and without a MXene film yields a complex conductivity $\sigma\omega = \sigma 1 + i\sigma 2$. Adapted with permission from [3], Copyright (2020) American Chemical Society 69

Figure 3-6 THz TDS of $Mo_2Ti_2C_3T_z$**,** (a) as deposited and (b) after a 200 °C vacuum annealing. (c) same as (a) but for $Mo_2TiC_2T_z$, (d) same as (b) but for $Mo_2TiC_2T_z$. Solid symbols represent real, and open symbols – imaginary conductivity, with lines showing global fits of the experimental data to the Drude-Smith model (Eq. 1) with parameters σ_{DC}, τ_{DS}, and c indicated on individual panels. Reprinted with permission from [3], Copyright (2020) American Chemical Society. 70

Figure 3-7 Transient photoconductivity in $Mo_2Ti_2C_3T_z$ ($-\Delta T/T \propto \Delta\sigma$) : photoconductivity decays following excitation with 800 nm, 100 fs pulses with different fluence values, as indicated in the legend, for (a) un-annealed, as-deposited film and (b) film annealed in vacuum at 200°C. Experimental data are fitted to a multi-exponential decay, and resulting decay times, which are fluence-independent, are given in panels. (c) Comparison of the transient photoconductivity decay for un-annealed and annealed films. Reprinted with permission from [3], Copyright (2020) American Chemical Society 74

Figure 3-8 Transient photoconductivity in $Mo_2TiC_2T_z$ ($-\Delta T/T \propto \Delta\sigma$) : photoconductivity decays following excitation with 800 nm, 100 fs pulses with different fluence values, as indicated in the legend, for (a) un-annealed, as-deposited film and (b) film annealed in vacuum at 200°C. Experimental data are fitted to a multi-exponential decay, and resulting decay times are given in the graphs. (c) Comparison of the transient photoconductivity decay for un-annealed and annealed films. Reprinted with permission from [3], Copyright (2020) American Chemical Society 76

Figure 3-9 Photoinduced change in complex THz conductivity in $Mo_2Ti_2C_3T_z$ at different times after excitation with excitation with ~ 256 μJ/cm^2, 100 fs, 800 nm pulses for an un-annealed (left) and annealed (right) films. Solid and open symbols show real, and imaginary conductivity components, respectively. Lines are fits of experimental data to Drude-Smith model. Reprinted with permission from [3], Copyright (2020) American Chemical Society.................................. 77

Figure 3-10 Photoinduced change in complex THz conductivity in $Mo_2TiC_2T_z$ at different times after excitation with excitation with ~ 512 μJ/cm^2, 100 fs, 800 nm pulses for an un-annealed (left) and annealed (right) films. Solid and open symbols show real, and imaginary conductivity components, respectively. Lines are fits of experimental data to Drude-Smith model. Reprinted with permission from [3], Copyright (2020) American Chemical Society 78

Figure 3-11 Scattering time τDS as a function of photoexcited carrier density in $Mo_2Ti_2C_3T_z$ scaled by the effective mass, extracted by fitting the complex photoconductivity spectra at different times after excitation and different excitation fluence values for un-annealed (open symbols) and annealed (solid symbols) samples. Reprinted with permission from [3], Copyright (2020) American Chemical Society 80

Figure 4-1 Schematic graph of optically controlable EMI shielding mechanism (left), THz transmissiom through $Ti_3C_2T_z$ MXene film is enhanced by ultrafast optical pump, this enhancement last more than 800 ps (right). Reprinted with permission from [4], Copyright (2019) American Chemical Society 86

Figure 4-2. EMI SE calculated from data in Figure 1-9 (b). Adapted with permission from [4], Copyright (2019) American Chemical Society 87

Figure 4-3 THz absorbance (left) and corresponding specific EMI shielding per unit thickness, defined as SE divided by density and thickness (right) for a $Ti_3C_2T_z$ film. Reprinted with permission from [4], Copyright (2019) American Chemical Society 88

Figure 4-4 Photoinduced change in EMI SE at different times following excitation with 800 nm, 950 μJ/cm^{2}pulse. Reprinted with permission from [4], Copyright (2019) American Chemical Society 89

Figure 4-5 Fabrication process of MXene wire-grid polarizer. (a, b) Preparation of MXene colloidal suspension. In (c) and (d), conventional photolithography is performed resulting in exposed areas for striations. (e) MXene aqueous colloidal suspension is spin-coated, and (f) lifted off by immersion in acetone. (g) AFM of a striation edge. (h) optical image of the final device and SEM close-up of striations. Copyright 2020 The Authors of [2]. Published by Wiley-VCH GmbH 93

Figure 4-6 Optical Images of four polarizer patterns tested herein. Copyright 2020 The Authors of [2]. Published by Wiley-VCH GmbH 93

Figure 4-7 (a) Schematic diagram of experiment: Incident THz pulse is focused to a ~ 1.5 mm spot on the polarizer using an off-axis polarizer; another polarizer collects the transmitted pulse, which goes through a commercial wire-grid polarizer before being detected. (b) A linearly polarized THz pulse is normally incident on a MXene polarizer, which can be rotated around the normal; only a component that is parallel to the incident pulse polarization is detected. Copyright 2020 The Authors of [2]. Published by Wiley-VCH GmbH.............. 94

Figure 4-8 (a) Reference THz waveform (transmitted through air), and THz waveforms transmitted through quartz substrate and through one of the polarizer devices (K4) with lines oriented along incident THz polarization. (b) Corresponding THz amplitude as a function of frequency. Dips in frequency are due to absorption by water vapor. Copyright 2020 The Authors of [2]. Published by Wiley-VCH GmbH.. 95

Figure 4-9 Peak of transmitted THz pulses, normalized to its value for $\theta = 0°$, as a function of θ, for polarizer structures (a) K1, (b) K2 (c) K3 and (d) K4. Symbols show experimental data, and lines – Malus's law fits. Copyright 2020 The Authors of [2]. Published by Wiley-VCH GmbH.. 95

Figure 4-10 Insertion loss of a quartz substrate. Symbols – experimental points calculated from data in Fig. 2(b), line – guide to the eye. At 1 THz, the insertion loss is ~ 0.6 dB, in agreement with predicted value due to air-quartz reflection, given n_{quartz}=2.156. At frequencies > 1.8 THz, impurity absorption and higher-lying phonon modes contribute to the measured insertion loss. Copyright 2020 The Authors of [2]. Published by Wiley-VCH GmbH 96

Figure 4-11 Transmitted THz pulses in time domain for incident THz pulse polarization parallel and perpendicular to the lines, for polarizer structures K1 (a), K2 (b), K3 (c), and K4 (d). Reference THz pulses transmitted through the quartz substrate are also shown. Copyright 2020 The Authors of [2]. Published by Wiley-VCH GmbH 97

Figure 4-12(a) Electric field extinction ratios, and (b) insertion losses for four THz polarizer devices. Copyright 2020 The Authors of [2]. Published by Wiley-VCH GmbH 98

Figure 4-13 Complex THz conductivity (solid symbols represent real and open symbols – imaginary conductivity components; lines show a global fit of both components to the Drude-Smith model with fit parameters given in the legend. Copyright 2020 The Authors of [2]. Published by Wiley-VCH GmbH............ 100

Figure 4-14 (a) FDTD simulation geometry of MXene polarizer. PML is perfect matched layer. PML 1 acts as a THz wave input, and PML 2 as THz wave output. (b), (c) Electrical field distribution in x-y plane (b) and x-z plane (c) when the polarization of the incident THz wave incident makes 45^{O} angle with the x-axis. Copyright 2020 The Authors of [2]. Published by Wiley-VCH GmbH............ 101

Figure 4-15. Simulated ER (a, c, e) and IL (b, d, f) at 1 THz as a function of fill factor (a, b), period (c,d) and thickness (e,f). Parameters that were fixed in a simulation are given in the top panels (a, d, e). Copyright 2020 The Authors of [2]. Published by Wiley-VCH GmbH 102

Figure 4-16 Frequency-resolved extinction ratios, and insertion losses for THz polarizer K1, the red and blue lines are the simulation results. 102

Figure 4-17. Spin-casting and lifting off of various concentration of solids in $Ti_3C_2T_z$, (a) Spin cast was performed in 30 seconds with 800 rpm rotation speed. SEM images of the resulting striations with spacing s=4μm spacing between the lines for (b) 3.4 g/L, (c) 6 g/L, (d) 8 g/L, (e) 15.1 g/L, and (f) 23 g/L concentration. Copyright 2020 The Authors of [2]. Published by Wiley-VCH GmbH 103

Figure 5-1 optical path of Intense THz attenuated by silicon wafers before detection 108

Figure 5-2 THz electrical field measured by opto-electrical sampling technique 108

Figure 5-3 The profile of THz focus spot is captured by the Flir A35 thermographic camera with a 320 × 256 pixels (pixel pitch of 2.5 μm) sensor, the sensor dimension is 8.0 mm X 6.4 mm. The diameter of focused THz spot is estimated to be 1.5 mm. 109

Figure 5-4 (a) The waveform of THz pulse attenuated by ten silicon wafers and one silicon mirror (45 degree). After the primary pulse, the later higher pulses are due to the interference between multireflection. (b) (c) are the first/primary THz pulse waveform in time domain and frequency domain by FFT. 110

Figure 5-5 Intense THz transmission of $Ti_3C_2T_z$, the insert shows the transmission at 0.8 THz depending on THz electrical field (Data taken by thesis author at MAX Plank Institute for Polymer Research, 2018)........................ 111

Figure 5-6 (a) Collinear THz pump THz probe setup, (b) (c) show the silicon mirror is optimized for reflecting THz probe pulse, where the reflection from it is about half of the reflection from original gold mirror.. 112

Figure 5-7 THz Z-scan schematic graph 113

1 Introduction and background

1.1 Two-dimensional MXenes

MXenes are a family of 2D transition metal carbides, carbonitrides and nitrides with a general formula $M_{n+1}X_nT_z$ (n=1-3), where M represents an early transitional metal (such as Sc, Ti, Zr, Hf, V, Nb, Ta, Cr, Mo and others), X is carbon and/or nitrogen, and T_z stands for the surface terminations, such as hydroxyl, oxygen, or fluorine. The first MXene, $Ti_3C_2T_z$, was discovered in 2011 by Michael Naguib *et al* at Drexel University[5]. In 2014, MXene solid solutions with a formula $(M'M'')_{n+1}X_nT_z$ were first synthesized. Here, M' and M'' are the two different transition metals and n = 2 or 3. This development has greatly increased the chemical variety of MXenes (Figure 1-1)[6]. Currently, over 70 stable MXenes have been predicted, and more than 30 have been synthesized, including $Ti_3C_2T_z$, Ti_2CT_z, $Mo_2TiC_2T_z$, $Zr_3C_2T_z$ [7,8,9,10]. MXenes are typically fabricated by selective etching of "A" atomic layers from the MAX phase precursors using HF or solutions of HCl and LiF. For example, when Ti_3AlC_2 is immersed in HF, the following sequentially occurred reactions result in 2D Ti_3C_2 exfoliated layers with OH and/or F surface groups.

$$\mathrm{Ti_3AlC_n + 3HF \longrightarrow AlF_3 + Ti_3C_2 + 1.5H_2}$$

$$\mathrm{Ti_3C_2 + 2H_2O \longrightarrow Ti_3C_2(OH)_2 + H_2}$$

$$\mathrm{Ti_3C_2 + 2HF \longrightarrow Ti_3C_2F_2 + H_2}$$

Furthermore, $Ti_3C_2(OH)_2$ is prone to oxidation in air, which results in oxygen-terminated MXene Ti_3C_2O. As a result of these processes, typical Ti_3C_2Tz flakes have mixed terminations Tz = -OH, =O and -F. After etching and washing, a

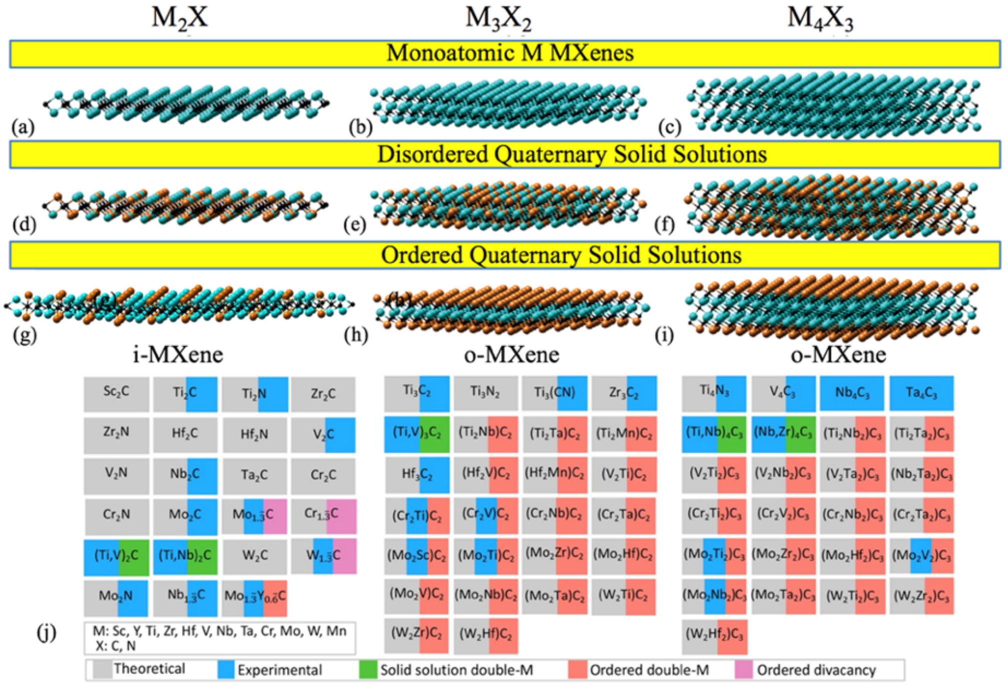
M_2X
M_3X_2
M_4X_3
Monoatomic M MXenes
(a)
(b)
(c)
Disordered Quaternary Solid Solutions
(d)
(e)
(f)
Ordered Quaternary Solid Solutions
(g)
(h)
(i)
i-MXene
o-MXene
o-MXene
(j)

Sc_2C	Ti_2C	Ti_2N	Zr_2C	Ti_3C_2	Ti_3N_2	$Ti_3(CN)$	Zr_3C_2	Ti_4N_3	V_4C_3	Nb_4C_3	Ta_4C_3
Zr_2N	Hf_2C	Hf_2N	V_2C	$(Ti,V)_3C_2$	$(Ti_2Nb)C_2$	$(Ti_2Ta)C_2$	$(Ti_2Mn)C_2$	$(Ti,Nb)_4C_3$	$(Nb,Zr)_4C_3$	$(Ti_2Nb_2)C_3$	$(Ti_2Ta_2)C_3$
V_2N	Nb_2C	Ta_2C	Cr_2C	Hf_3C_2	$(Hf_2V)C_2$	$(Hf_2Mn)C_2$	$(V_2Ti)C_2$	$(V_2Ti_2)C_3$	$(V_2Nb_2)C_3$	$(V_2Ta_2)C_3$	$(Nb_2Ta_2)C_3$
Cr_2N	Mo_2C	$Mo_{1.\bar{3}}C$	$Cr_{1.\bar{3}}C$	$(Cr_2Ti)C_2$	$(Cr_2V)C_2$	$(Cr_2Nb)C_2$	$(Cr_2Ta)C_2$	$(Cr_2Ti_2)C_3$	$(Cr_2V_2)C_3$	$(Cr_2Nb_2)C_3$	$(Cr_2Ta_2)C_3$
$(Ti,V)_2C$	$(Ti,Nb)_2C$	W_2C	$W_{1.\bar{3}}C$	$(Mo_2Sc)C_2$	$(Mo_2Ti)C_2$	$(Mo_2Zr)C_2$	$(Mo_2Hf)C_2$	$(Mo_2Ti_2)C_3$	$(Mo_2Zr_2)C_3$	$(Mo_2Hf_2)C_3$	$(Mo_2V_2)C_3$
Mo_2N	$Nb_{1.\bar{3}}C$	$Mo_{1.\bar{3}}Y_{0.\bar{6}}C$		$(Mo_2V)C_2$	$(Mo_2Nb)C_2$	$(Mo_2Ta)C_2$	$(W_2Ti)C_2$	$(Mo_2Nb_2)C_3$	$(Mo_2Ta_2)C_3$	$(W_2Ti_2)C_3$	$(W_2Zr_2)C_3$
M: Sc, Y, Ti, Zr, Hf, V, Nb, Ta, Cr, Mo, W, Mn X: C, N				$(W_2Zr)C_2$	$(W_2Hf)C_2$			$(W_2Hf_2)C_3$			

⬜ Theoretical 🟦 Experimental 🟩 Solid solution double-M 🟥 Ordered double-M 🟪 Ordered divacancy

Figure 1-1 (a) to (i) MXene taxonomy. (j) Potential MXene compositions. Compositions colored blue, that number 30, have already been synthesized. For ordered solid solutions, i-MXene stands for in-plane, and o-MXene – for out-of-plane order. Figure courtesy M. Barsoum.

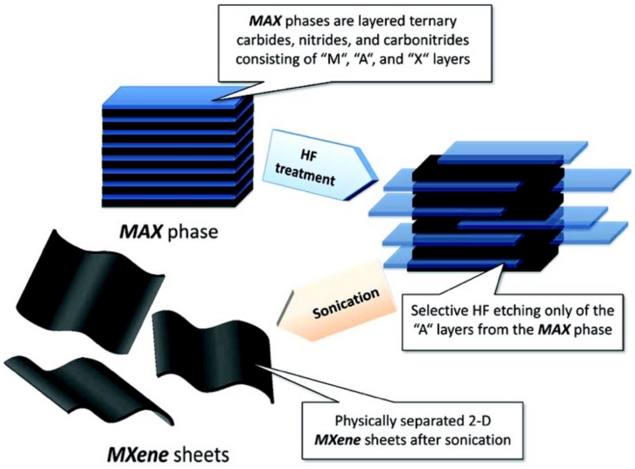
MAX phases are layered ternary carbides, nitrides, and carbonitrides consisting of "M", "A", and "X" layers
HF treatment
MAX phase
Sonication
Selective HF etching only of the "A" layers from the ***MAX*** phase
Physically separated 2-D ***MXene*** sheets after sonication
MXene sheets

Figure 1-2 Schematic for the exfoliation process of MAX phases and formation of MXenes. Reprinted with permission from [1]. Copyright (2012) American Chemical Society.

suspension of MXene flakes is obtained, as illustrated schematically Figure 1-2.

A $Ti_3C_2T_z$ film on a substrate can then be fabricated by spin coating or interfacial film assembly techniques (Figure 1-4). Recent advances in the fabrication of MXenes have resulted in improved conductivity[11], scalable production [12, 13] and, most recently, long-term stability under ambient conditions[14].

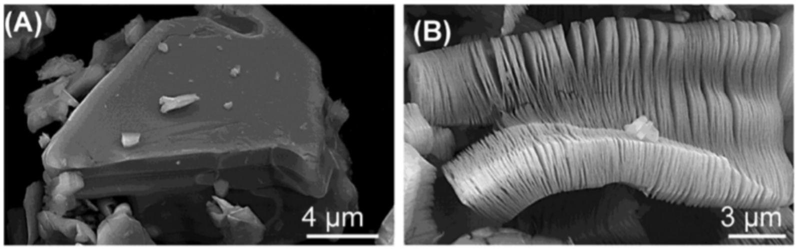

Figure 1-3 Secondary electron scanning electron microscope (SEM) micrographs for (A) Ti_3AlC_2 particle before treatment, which is typical of unreacted MAX phases, (B) Ti_3AlC_2 after HF treatment. Reprinted with permission from [17]. Copyright (2012) American Chemical Society.

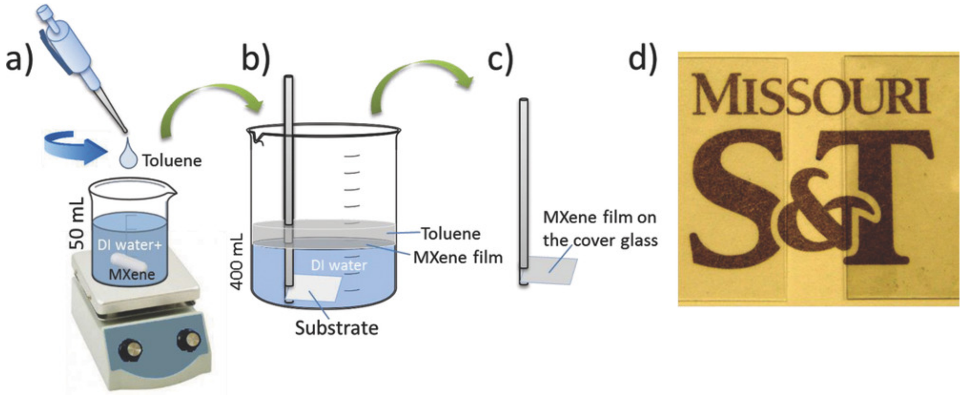

Figure 1-4 a–c) Procedure for preparing $Ti_3C_2T_z$ thin films with varying thicknesses (≈5–67 nm) on glass and Si substrates via the interfacial film formation technique. d) The optical photograph shows transparent $Ti_3C_2T_z$ film (right side) uniformly covering a large area of 1 × 1 cm^2 glass substrates. Bare uncoated glass slide is shown on the left for comparison. Reprinted with permission from [15]. © 2018 WILEY-VCH Verlag GmbH & Co. KGaA, Weinheim.

1.1.1 Electrical properties of MXene

High electrical conductivity of MXenes is one of their most important properties for applications in transparent conductive electrodes, electromagnetic interference shielding, gas sensors, and others[1, 6, 16-27]. As their parent MAX phase, bare MXenes are predicted to be metallic with a high density of states (DOS) at the Fermi level [28, 29]. However, the conductivity of MXene films depends not only on the chemical composition of MXene cores, but also on the surface termination groups [30, 31]. For example, F and OH groups can receive one electron from the MXene surface, while the O termination requires two electrons to be stabilized, resulting in different properties of MXenes with predominantly OH/F versus O surface groups.[30]

All reported experimental measurements of MXene properties confirm the metallicity of individual MXene sheets. Miranda et al reported that single MXene $Ti_3C_2T_z$ flakes demonstrate the metallic nature of their conductivities with free carrier density of $8 \pm 3 \times 10^{21}$ cm^{-3} and mobility 0.7 ± 0.2 cm^2 V^{-1} s^{-1} at room temperature.[32] Measurements performed by Lipatov et al on field-effect transistors (FETs) based on monolayer $Ti_3C_2T_z$ flakes found a field-effect electron mobility of 2.6 ± 0.7 cm^2 V^{-1} s^{-1} and a high conductivity of 4600 ± 1100 S cm^{-1}.[33] They also found that the resistivity of multilayer $Ti_3C_2T_z$ films is only one order of magnitude higher than the resistivity of individual flakes, which indicates efficient electron transport through the surface terminations of different flakes. By comparison, in graphite, a stack of 2D sheets of graphene, the resistance perpendicular and parallel to the basal plane differs by three orders of magnitude.[33] For individual single-layer $Nb_4C_3T_x$ flakes, Lipatov et al. found an electrical conductivity of 1024 ± 165 S cm^{-1}, which is two orders of magnitude higher than the previously reported values for bulk $Nb_4C_3T_x$ assemblies, and an electron mobility of 0.41 ± 0.27 $cm^2 V^{-1} s^{-1}$.[34]

In the case of MXene films, variations in thickness, preparation, and postprocessing methods such as vacuum annealing result in a large variation in conductivity even for the same material. For example, Halim et al. reported that the resistivity of as-deposited Mo-based MXene films increases with decreasing temperatures despite the metallic nature of individual flakes[35]. However, annealing the films in vacuum to release the intercalated species resulted in a typical metallic behavior, with resistivity increasing at low temperatures. They further demonstrated that the long-range conductivity of MXene films is well-described by a thermally activated variable range hopping model which has been previously applied to describe granular metals[35]. This picture has been confirmed by multiple studies. For example, James et al. found that MXene surface de-functionalization results in increased electronic conductivity, while intercalation of various species in van der Waals gaps suppresses inter-flake transport.[36]

1.1.2 Optical properties and applications of MXenes

Optical properties of MXenes also differ substantially from other mostly-semiconducting 2D materials. The most extensively studied MXene, $Ti_3C_2T_z$, is highly transparent in the visible range. As is show in Figure 1-5, the transmittance for a 25 nm-thick $Ti_3C_2T_z$ film is between 58% and 75% in the wavelength range from 400 nm to 900 nm. Studies in the broad frequency range found that it exhibits high reflectivity in the ultraviolet due to the onset of inter-band transitions[37] and a plasmon resonance in the near-infrared range, 780 nm to 1000 nm[15]. Terminations T_z are predicted to strongly affect not only the electronic but also the optical properties. For instance, Berdiyorov predicted that the oxidized sample shows larger absorption, whereas surface fluorination results in weaker absorption compared with pristine Ti_3C_2 MXene[37]. Nonlinear optical absorption in the visible and infrared range has been demonstrated and applied to laser mode-locking. Using the Z-scan method, saturable absorption was discovered in $Ti_3C_2T_x$ MXene at 1064 nm. It arises from plasmon-induced increase in the ground state absorption at photon energies above the threshold for free carrier oscillations[15]. Likewise, V_2CT_x was employed as a saturable absorber for a hybrid passively mode-locked fiber laser at 1564 nm,[38] while Ti_3CN

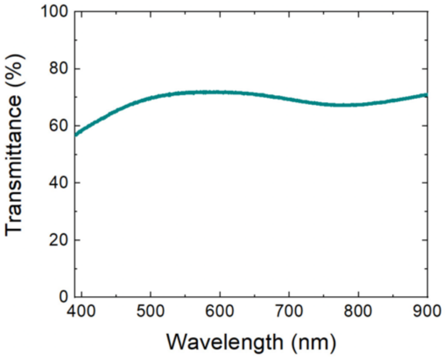

Figure 1-5 UV-VIS optical transmittance of a 25 nm thick $Ti_3C_2T_z$ film (Data taken by thesis author at MAX Plank Institute for Polymer research, 2018) (Reprinted with permission from [4], Copyright (2019) American Chemical Society)

was successfully applied to a mode-locked1557nm fiber laser, producing 660 fs pulses at a repetition rate of 15.4 MHz[39].

Finally, high intrinsic charge carrier density and high mobility of the carriers suggest that MXenes are promising for THz detection and EMI shielding in the THz range. Using density functional theory calculation of Ti_3C_2, Jhon et al. predicted that THz EMI shielding efficiency by stacks of Ti_3C_2 is comparable to that of stacked graphene layers [49]. Table 1-1 summarizes proposed photonic applications of MXenes from microwave to visible range.

Table 1-1 Proposed application of MXenes in optical devices operating in visible to microwave range. Experimental demonstration of THz EMI properties [4] and THz polarizer [2] are discussed in Chapters 4.

Spectral range	Application	MXene class	Band range
Microwave	Wi-Fi, Bluetooth[40]	$Ti_3C_2T_x$	1.5 – 3.5 GHz
	EMI[41,42],	$Ti_3C_2T_x$, $Mo_2Ti_2C_3T_x$, $Mo_2TiC_2T_x$, Ti_2CT_x	X-band(8.2−12.4 GHz)
Terahertz	EMI[4, 43, 44] Polarizer[2]	$Ti_3C_2T_x$	0.2 – 2.2 THz (Chapter 4 in this paper)
Infrared	Mode-locked fiber laser[38, 45, 46]	Ti_2CT_x	5.3 ps/1565 nm, 164 ps/1051 nm
		Ti_3CN	660 fs/1557 nm
Visible	Quantum dot light emitters[47]	V_2C	300 – 500 nm
	Photodetector[48]	Mo_2CT_x	400 – 800 nm

While much progress has been made in the past decade in uncovering unique optical and electronic properties of MXenes, fundamental relationships between MXene chemistry (represented by the choice of transition metal M and n=1-3), MXene film morphology, on the one hand, and MXene's electronic properties (viz. carrier density and mobility), nature of photoexcitations, photoconductivity, and the lifetime of optically injected charge carriers on the other, remain elusive. In particular, understanding the optoelectronic properties of MXene films requires decoupling the intrinsic, intra-nanosheet charge carrier transport that is mainly a function of MXene chemistry from inter-nanosheet transport that is affected by nanosheet size, morphology, and intercalated species present in the van der Waals gaps. The focus of this thesis is application of THz spectroscopic techniques to investigate those relationships as well as to identify possible applications of metallic 2D MXenes in THz photonics devices. THz spectroscopy is an all-optical technique that can probe both short- and long-range conductivity and dynamics of photoexcitation without the complication of electrical contracts. As such, it probes both intra- and inter-nanosheet carrier transport, and allows an understanding of the impact of different variable such as M, n, or film processing conditions, on MXene properties, to emerge. We have studied Ti-based and mixed Ti-Mo based MXenes for which the established synthesis protocols have already been developed.[3, 27] We demonstrate that controlling MXene structure, chemistry, and the film properties via post-synthesis modifications can be used to engineer optoelectronic properties of MXene films. In the future, this work can be used as a guide for continued investigation of other MXenes. From a technological standpoint, developing approaches to engineer MXene film's electronic and optical properties will enable their deployment in new technologies such as flexible transparent electrodes, electromagnetic interference shielding, THz detectors and modulators, photocatalysis, and others. Here, we provide proof-of-concept demonstrations of using MXenes in electromagnetic interference shielding and polarizers[2] in the THz spectral range.

1.2 THz spectroscopy

1.2.1 THz electromagnetic radiation

THz radiation has frequency ranging from 100 GHz to 10 THz, corresponding to 3 mm to 30 μm in wavelength, and is located between the infrared and microwave ranges. The common types of continuous wave THz sources include the backward-wave oscillator[50], travelling-wave tubes[51], gyrotrons[52], free-electron lasers[53], and THz quantum cascade lasers[54].

Picoseconds-duration broadband THz pulses, typically used in THz spectroscopy, are generated using ultrashort, ~ 100 fs duration, optical and near-infrared laser pulses. In one approach, pulsed laser excitation generates short-duration transient currents in photoconductive switches[55] or antennas[56], resulting in THz emission. Broadband THz pulses can also be generated by air or other gas plasma, excited by gas photoionization at the focus of femtosecond laser pulses of two colors, typically 400 nm and 800 nm[57].

Finally, optical rectification, a second-order nonlinear optical effect, is another common approach for generating broadband THz pulses for THz time domain spectroscopy. It is used in the experiments presented here. When intense laser light interacts with a non-centrosymmetric nonlinear medium, wave mixing between two frequencies can occur, resulting in sum and difference frequency generation.

The second-order nonlinear polarization $P^{(2)}$, induced by an optical excitation, can be represented as

$$P^{(2)}(\omega = \omega_1 \pm \omega_2) = \chi_{ijk}^{(2)}(\omega)A_1(t)A_2(t)\cos(\omega_1 t)\cos(\omega_2 t) =$$

$$\frac{1}{2}\chi_{ijk}^{(2)}(\omega)A_1(t)A_2(t)([\cos(\omega_1 - \omega_2)t] + \cos[(\omega_1 + \omega_2)\,t]) = P_\Delta^{(2)}(\omega) + P_\Sigma^{(2)}(\omega) \quad (\mathrm{Eq.}\,1)$$

Here, $\chi_{ijk}^{(2)}$ is the susceptibility tensor, $A_1(t)$, $A_2(t)$, ω_1 , ω_2 are the amplitude and frequency of the two incident waves, $P_\Delta^{(2)}(\omega)$ is the difference frequency component, and , $P_\Sigma^{(2)}(\omega)$ is the sum frequency component of the second- order polarization.

In the particular case when $\omega_1 = \omega_2$, second harmonic generation (SHG) and optical rectification (OR) occur. For $A_1 = A_2 = A$, $\omega_1 = \omega_2 = \omega$,

$$P^{(2)}(2\omega) = \frac{1}{2}\chi_{ijk}^{(2)}(2\omega)A^2(t) + \frac{1}{2}\chi_{ijk}^{(2)}(2\omega)A^2(t)\cos(2\omega\, t) = P_\Delta^{(2)}(0) + P_\Sigma^{(2)}(2\omega) \quad (\mathrm{Eq.}\,2)$$

Here, $P_\Delta^{(2)}(0)$ is OR term, independent of the carrier frequency, and $P_\Sigma^{(2)}(2\omega)$is the SHG term. Because the near-IR pulse has a duration of ~ 100 fs, and OR response follows the envelope of the optical generating pulse, it results in emission of near single-cycle electromagnetic radiation pulses with frequencies in the THz range. For example, a commonly used THz source crystal is ZnTe. ZnTe crystals have cubic symmetry ($\bar{4}3m$ space group) and a large 2nd order nonlinear susceptibility $\chi^{(2)} = 1.6 \times 10^{-7}$ esu.[58] ZnTe has a broad TA-phonon absorption line centered at 1.7 THz and one stronger at 3.7 THz in addition to a TO-phonon resonance at 5.3 THz limiting the bandwidth to below 5 THz with a typical crystal thickness of 1 mm.[59] The typical pulse energy generated by ZnTe is around 1.5 μJ [60]

Another crystal with a larger 2nd order nonlinear susceptibility $\chi^{(2)}$ (d_{33} = 27 pm/V) is $LiNbO_3$.

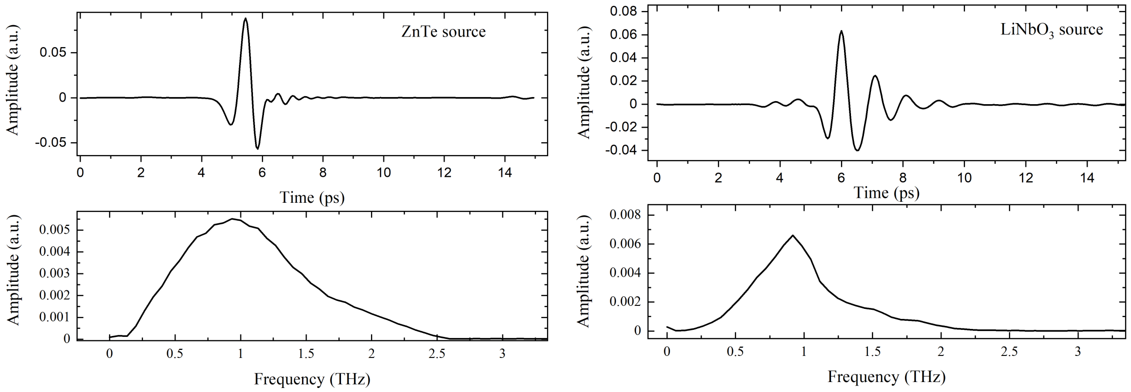

Figure 1-6 THz waveforms in nitrogen environment based on ZnTe (right)/LiNbO3 (left) crystals pumped with 800 nm femtosecond laser (Data taken by thesis author at MAX Plank Institute for Polymer research, 2018)

Its drawback is mismatch between the THz phase velocity (n_{THz} = 4.96) and the near-infrared group velocity ($n_{800\,nm}^{gr}$ = 2.25). Hebling *et al.* proposed an approach for achieving phase matching between the excitation and the generated THz radiation in $LiNbO_3$ by tilting of the intensity front of the ultrafast infrared pulse such that $n_{800\ nm}^{gr} \cos\gamma = n_{THz}$, as shown schematically in Figure 1-7 (a)[61]. The required tilt of the pulse front of the excitation to 63° to satisfy the phase matching requirements is achieved experimentally by reflecting the 800 nm pulse from a diffraction grating and focusing it on a $LiNbO_3$ prism cut to the same 63° angle Figure 1-7 (b). Such source of intense THz pulses can yield intense THz pulses with pulse energy of up to 20 μJ and peak electric field of 120 $\frac{\mathrm{kV}}{\mathrm{cm}}$. Here, it is used to study nonlinear properties of MXenes in the THz range.

The free space electrooptic sampling method is typically used to detect of THz pulses. The electric field of a THz pulse induces a small birefringence in an electro-optic crystal (such as ZnTe or GaP) due to the Pockels effect[62]. In the presence of applied THz electric field, an initially linearly polarized optical probe beam going through this crystal becomes elliptically polarized, with ellipticity is proportional to the electric field of the THz pulse in the limit of small ellipticity angles. By varying the time delay of the sampling 800 nm beam with respect to the THz pulse, it is possible to reconstruct the entire THz waveform. This way, THz pulses are detected coherently, retaining information about both their amplitude and the phase. Analysis of the changes in both the amplitude and the phase of the THz pulses as a result of their interaction with the material allows extraction of complex, frequency-dependent dielectric function, or, equivalently, complex optical conductivity, as described below. Complex optical conductivity in the THz range contains information about various phenomena that have characteristic energies in the THz range (~meV), such as free carrier absorption[63, 64], transitions between ground and excited states of excitons in semiconductors[65, 66], spin waves in magnetic materials[67, 68], intermolecular vibrational modes in solutions[69], phonons[70, 71], polarons[72] and others. Here, we use broadband THz pulses to study these low energy phenomena in MXenes.

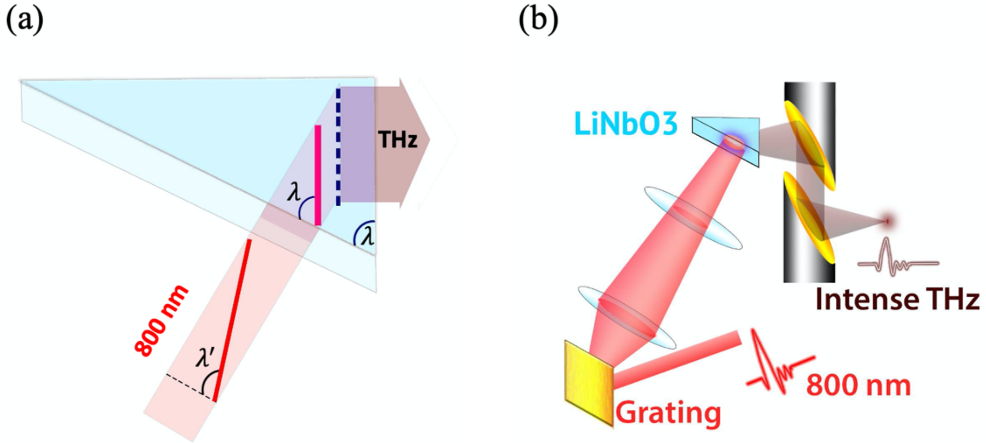

Figure 1-7 (a) The generated THz phase front (dashed black bold line) in the $LiNbO_3$ crystal is matched parallelly with the tilted intensity front of the 800 nm pump pulse (bold red line), (b) $LiNbO_3$ crystal based intense THz source schematic diagram.

1.2.2 THz time domain spectroscopy (THz-TDS)

In THz-TDS setup used in this project**,** a picosecond-duration THz pulse is generated by optical rectification of 800 nm femtosecond optical pulse in [100] ZnTe crystal. It is detected in a second ZnTe crystal by free-space electro-optic sampling as in depicted in Figure 1-8. The bandwidth of generated THz pulse is

0.25–2.0 THz, or 1–10 meV. Figure 1-9 shows an example of a THz pulse transmitted through quartz substrate and a THz pulse transmitted through a 25-nm thick $Ti_3C_2T_z$ MXene film deposited on a substrate. Applying the Fast Fourier Transformation (FFT) to both waveforms yields both the amplitude and phase of the transmitted THz pulses. Within a thin film approximation, the complex, the frequency-dependent conductivity $\tilde{\sigma}(\omega)$ in the THz is then calculated using the following relationship:

$$\frac{\tilde{E}_{sample}(\omega)}{\tilde{E}_{substrate}(\omega)} = \frac{n+1}{n+1+Z_0\tilde{\sigma}(\omega)d} \quad (\mathrm{Eq.}\,3)$$

where $Z_0 = 377\ \Omega$ and n are the free space impedance, the refractive index of the substrate in THz range, d is the thickness of the target film, $\tilde{E}_{sample}$ is the

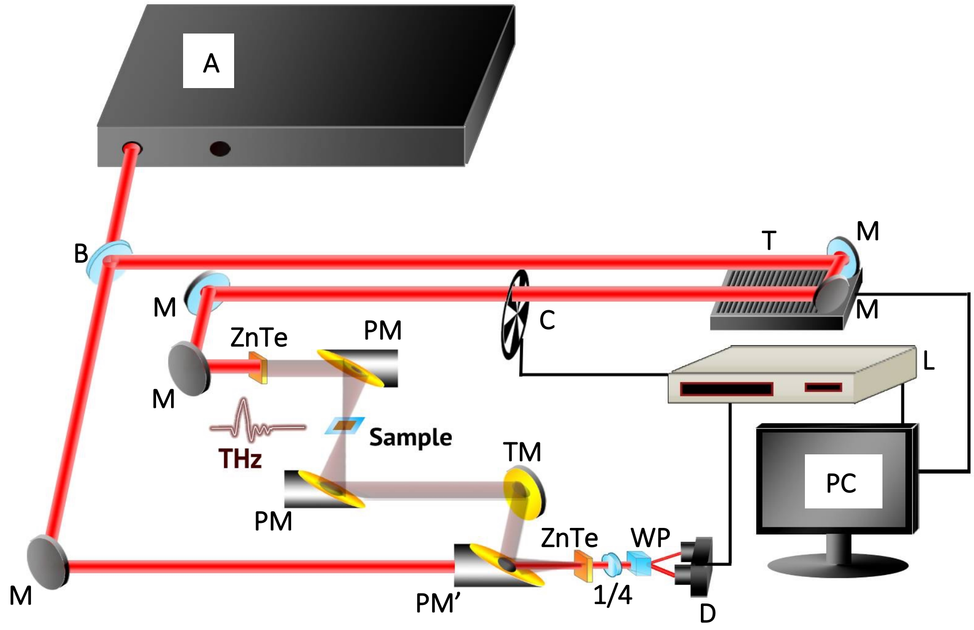

Figure 1-8 THz-TDS schematic diagram, where A: femtosecond laser, B: beam splitter, C: optical chopper, D: photodetector, M: Mirror, PM: parabolic mirror, PM’: parabolic mirror with a hole, TM: THz mirror, L: Lock-in amplifier, T: translational stage, 1/4: quarter waveplate, WP: Wollaston prism, PC: computer

electrical field of THz pulse transmitted through sample and substrate, while $\tilde{E}_{substrate}$ is its counterpart transmitted through substrate alone, which serves as a reference signal[73]. Both $\tilde{E}_{substrate}$ and $\tilde{E}_{sample}$ are complex and yield the complex conductivity of the film, containing both the real and imaginary components. In Figure 1-8, the extracted frequency resolved conductivity could be fitted with Drude Smith model which will be discussed in later section 1.2.3.

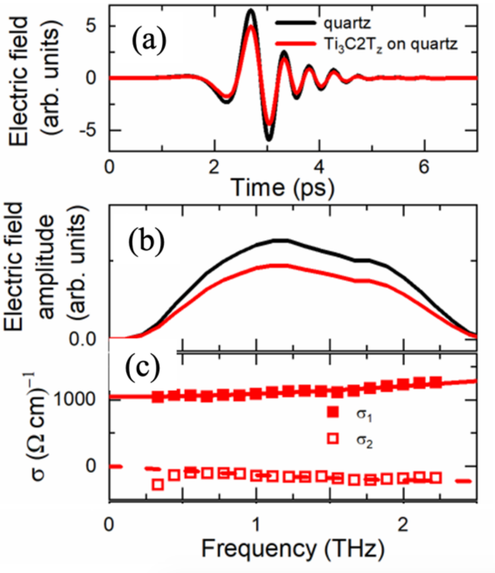

Figure 1-9 (a) THz-TDS waveform transmitted through a quartz substrate and through the substrate with a $Ti_3C_2T_z$ film. (b) Frequency domain spectroscopy obtained by FFT. (c) complex THz conductivity (solid symbols represent real and open symbols imaginary conductivity components; lines show a global fit of both components to the Drude-Smith model which is discussed later in section 1.2.3. (Adapted with permission from [4], Copyright (2019) American Chemical Society)

1.2.3 THz conductivity models

Fitting the experimentally extracted conductivity spectra to an appropriate model that captures the basis physics of the studied material allows extracting crucial parameters such as the free carrier density, carrier mobility, plasmon or phonon frequency, and others. Phenomenological Drude model, and its various modifications are often used to analyze free carrier response.

Drude model

In the steady state (DC) or at low frequencies, the Drude model assumes that non-interacting charge carriers are free to move in an electric field with drift velocity $v_D = \mu E$, where μ is the carrier mobility and E is the electric field. The carrier mobility is given by

$$\mu = \frac{e\tau}{m^*} \quad (\mathrm{Eq.}\,4)$$

where e is the electric charge, m* is the effective mass of the carrier and τ is the Drude relaxation time associated with scattering of the charge carriers and is assumed to be independent of carrier energy. Since the current density is $J = \sigma_{DC}E = nev_D$, where n is the carrier concentration (carrier density) and σ_{DC} is the steady-state conductivity of the materials, then

$$\sigma_{DC} = ne\mu = \frac{ne^2\tau}{m^*} = \epsilon_0\omega_p^2\tau \quad (\mathrm{Eq.}\,5)$$

where ω_p is the plasma frequency for the charge carrier density in the material ($\omega_p^2 = \frac{ne^2}{\epsilon_0 m^*}$). Scattering of charge carriers, as determined by the Drude relaxation time, introduces a damping term to the equations of motion for the charge carriers. When the applied electric field is time-dependent, the dependence of the Drude conductivity is then given by:

$$\tilde{\sigma} = \sigma_1 + i\sigma_2 = \frac{\sigma_{DC}}{1 - i\omega\tau} \quad (\text{Eq. 6})$$

$$\sigma_1 = \frac{\sigma_{DC}}{1 + (\omega\tau)^2} \quad (\text{Eq. 7})$$

$$\sigma_2 = \frac{\sigma_{DC}\omega\tau}{1 + (\omega\tau)^2} \quad (\text{Eq. 8})$$

Drude–Lorentz model with a restoring force.

If the charge carriers experience a restoring force, their motion under the action of an external electromagnetic wave can be approximated by the equation of motion of a damped, driven simple harmonic oscillator. Drude-Lorentz complex conductivity is given by

$$\sigma(\omega) = \frac{Ne^2}{m^*} \frac{\tau}{1 - \left(i\tau \left(\omega - \frac{\omega_0^2}{\omega} \right) \right)} \quad (\text{Eq. 9})$$

This model is applicable to plasmons, or collective excitations of free carrier plasma experiencing a restoring force due to Coulombic interaction with ion cores, as well as to infrared-active phonon modes[74].

Drude-Smith model.

Another phenomenological modification to the Drude model is **Drude-Smith model[75]**. It accounts for carrier localization over the length scales comparable with the carrier mean free path[76-85]. It has been applied extensively to analyze THz conductivity in poly- and nanocrystalline materials[86], nanowires[73], nanotubes[87] and 2D nanostructures[88]. In its original formulation by N.V. Smith, complex conductivity is affected by multiple elastic scattering events, with grain boundaries or disorder acting as scattering centers:

$$\sigma(\omega) = \frac{Ne^2\tau_{DS}}{m^*}\frac{1}{1-i\omega\tau_{DS}}\left(1+\sum_{p=1}^{\infty}\frac{c_p}{(1-i\omega\tau_{DS})^p}\right)(\text{Eq. }10)$$

Here, the parameter c_p is the expectation value $\langle \cos\theta \rangle$, for scattering angle θ after p^{th} scattering event relative to the initial carrier momentum. Commonly, the infinite series in this equation is truncated at $p = 1$, which assumes that the carrier retains part of its initial momentum during the first scattering event, but in every subsequent scattering event the velocity is randomized:

$$\sigma(\omega) = \frac{Ne^2\tau_{DS}}{m^*}\frac{1}{1-i\omega\tau_{DS}}\left(1+\frac{c}{1-i\omega\tau_{DS}}\right) (\text{Eq. }11)$$

In this case, $c = 0$ corresponds to the Drude free carrier response, and $c = -1$ describes the situation where the carriers are confined over mesoscopic distances due to complete backscattering at grain boundaries or similar structures. In a recent first principles and Monte Carlo simulation study, Cocker et al. clarified that the microscopic origin of the Drude-Smith model is a diffusive restoring current as applied time-varying electric field creates an average local carrier density gradient inside an ensemble of weakly confining nanoparticles or grains[89].

MXene films studied here consist of micrometer-sized single layer flakes (Figure1-3). Free carriers within the flakes can scatter off flake edges and grain boundaries. Drude- Smith model provides an adequate yet simple description of the complex THz conductivity in MXene films, allowing us to determine carrier density and mobility, and providing insight into the inter-flake carrier hopping[75, 89, 90]. Analyzing conductivity spectra obtained by THz-TDS within this framework sheds light on not only the macroscopic conductivity but also the microscopic conductivity of the target film.

1.2.4 Optical pump THz probe (OPTP) spectroscopy

OPTP is a THz-TDS based technique that enables measurement of the transient

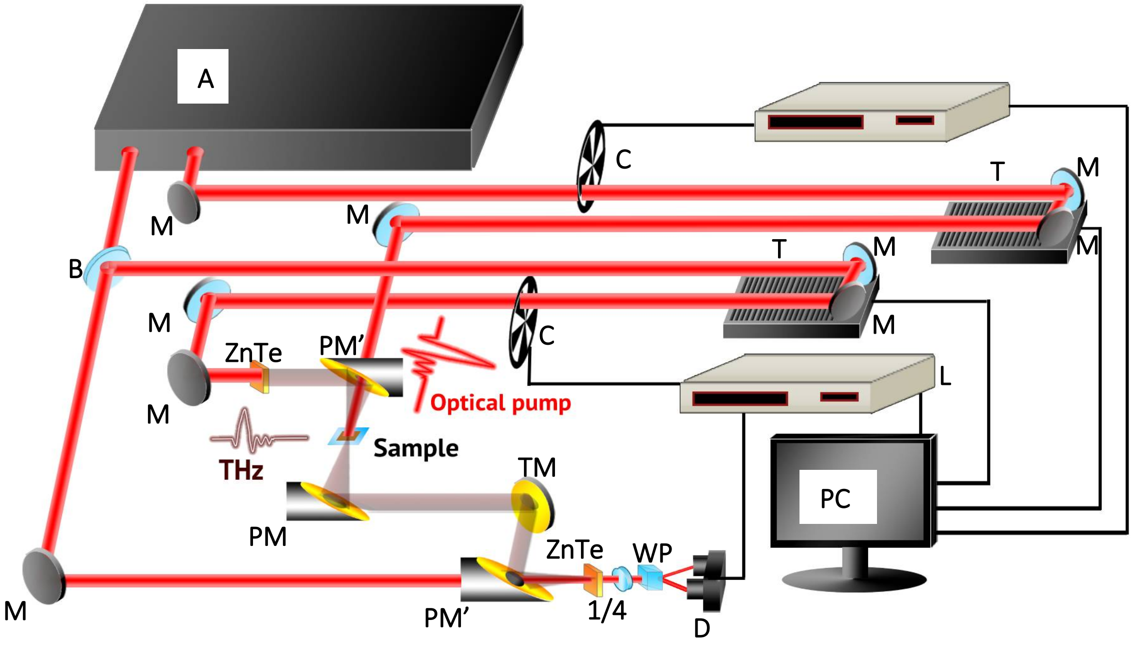

Figure 1-10 OPTP schematic diagram, where A: femtosecond laser, B: beam splitter, C: optical chopper, D: photodetector, M: Mirror, PM: parabolic mirror, PM': parabolic mirror with a hole, TM: THz mirror, L: Lock-in amplifier, T: translational stage, 1/4: quarter waveplate, WP: Wollaston prism, PC: computer

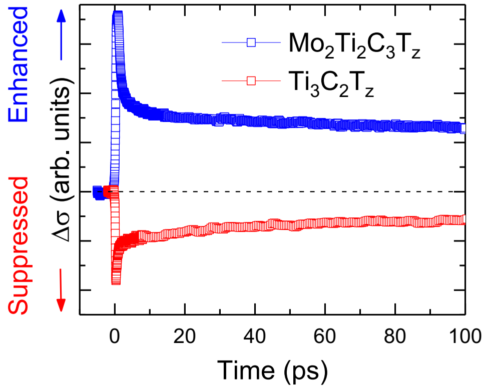

Figure 1-11 Decay curves of photoinduced changes in complex THz conductivity in $Mo_2Ti_2C_3T_z$ and $Ti_3C_2T_z$ after excitation with 100 fs, 800 nm pulses. Here, the conductivity of in $Mo_2Ti_2C_3T_z$ is enhanced while the conductivity of $Ti_3C_2T_z$ is suppressed.

THz conductivity of a sample after photoexcitation. In TRTS, instead of comparing THz pulse transmission through the sample to the reference THz pulse, we monitor the changes in the sample induced by the ultrashort optical pump pulse (400 nm/800 nm) by detecting the differences of THz transmission. Schematic of the experimental OPTP setup is shown in Figure 1-10. By changing pump-probe delay time, we can analyze the photoconductivity relaxation processes such as carrier-carrier interaction, carrier trapping, Auger recombination, carrier recombination, and correlate them to the energy band structure as well as to the film morphology. For example, although both single layer sheets of $Ti_3C_2T_z$ and $Mo_2Ti_2C_3T_z$ are metallic, the photoconductivity decay for $Ti_3C_2T_z$ and Mo-MXene show different sign (see Figure 1-11), with photoexcitation transiently suppressing conductivity in $Ti_3C_2T_z$ and increasing it in $Mo_2Ti_2C_3T_z$. The detailed discussion of transient photoconductivity in these materials in presented in Chapters 2 and 3. Finally, the complex, frequency-resolved photoconductivity at a given time after photoexcitation is calculated as[73]

$$\Delta\sigma(\omega, \Delta t) \approx -\frac{n+1}{Z_0}\frac{\Delta E(\omega, \Delta t)}{E(\omega)}. \text{ (Eq. 12)}$$

An example of the photoinduced change in complex THz conductivity in $Mo_2Ti_2C_3T_z$ at 5 ps after excitation with ~256 μJ/cm^2, 100 fs, 800 nm pulses is given in Figure 1-12. Analyzing the frequency-resolved transient photoconductivity spectra of MXene films using the Drude-Smith model [3, 89], we learn about the relaxation channels and dynamics of photoexcited carriers. This information is crucial for designing the optoelectronic application such as optical switches, light sensors, solar cells, and others.

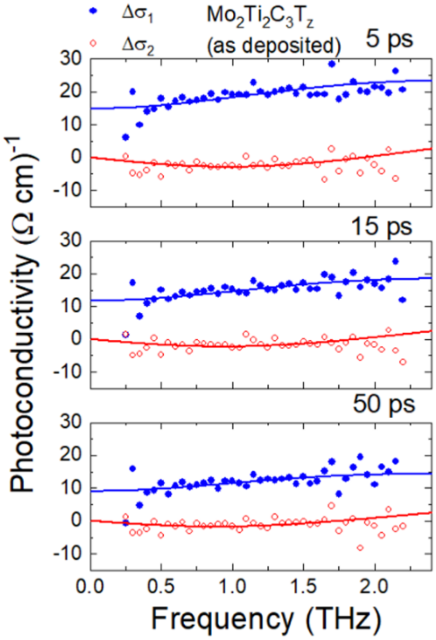

Figure 1-12 Photoinduced changes in complex THz conductivity in $Mo_2Ti_2C_3T_z$ at 5 ps after excitation with ~256 μJ/cm^2, 100 fs, 800 nm pulse. Lines are fits of experimental data to the Drude–Smith model. Adapted with permission from [4], Copyright (2019) American Chemical Society

The following chapters describe applications of THz TDS and OPTP spectroscopy to study MXene electronic and optical properties. Specifically, there different MXenes with different structures and chemistries have been investigated. Chapter 2 focuses on THz spectroscopy studies of $Ti_3C_2T_z$, the MXene with the highest conductivity that has been fabricated to date. Chapter 3 explores the effect of replacing some of Ti by Mo in MXene structure and the role played by the intercalated species on THz photoconductivity. Chapter 4 discusses possible applications of $Ti_3C_2T_z$ MXene in THz photonic devices. Finally, Chapter 5 presents preliminary nonlinear THz spectroscopy measurements and presents the future directions for this work.

2 THz study of 2D $Ti_3C_2T_z$ MXenes: intrinsic conductivity and photoexcited carrier dynamics

2.1 Introduction:

Even as thirty new MXenes have been fabricated since 2011, the first discovered member of MXene family, $Ti_3C_2T_z$, remains the most conductive, with film conductivity up to 20,000 $(\Omega\ cm)^{-1}$ recently achieved[91], showing promise for precious-metal-free flexible conductor applications. It is also characterized by high, ≈70 $mJ\ cm^{-2}$ threshold for light-induced damage with up to 50% modulation depth, ideal for femtosecond mode locking and optical isolation applications[38, 45, 46], and volumetric capacitance up to 900 F/cm^3,[92] promising for electrochemical energy storage applications. It has also been recently demonstrated to be an efficient photothermal convertor, with efficiency of light-to-heat conversion in MXenes including $Ti_3C_2T_z$ reaching 100%, applicable in photothermal solar energy conversion devices as well as in novel photothermal tumor ablation approaches in oncology[7]. High electrical conductivity of $Ti_3C_2T_z$ results in a strong absorption across the microwave and terahertz (THz) range and makes it a promising new material for electromagnetic shielding[25, 44]. Combined with thermoelectric properties of $Ti_3C_2T_z$ MXenes, large THz absorption also suggests potential application in THz detectors[24]. Considering a wide range of potential photonic, electronic and electrochemical applications of $Ti_3C_2T_z$, it is necessary to elucidate intrinsic electronic properties of this material and understand the effects of photoexcitation on conductivity and ultrafast nonequilibrium dynamics of photoexcited carriers.

Here, we used THz-TDS and OPTP spectroscopy to study both equilibrium and non-equilibrium free carrier dynamics in $Ti_3C_2T_z$ MXene films. As described in detail below, we find that $Ti_3C_2T_z$ is metallic, with ahigh, ~ 10^{21} cm^{-3} density of highly mobile intrinsic carriers, with short range mobility of carriers within the individual metallic $Ti_3C_2T_z$ nanoflakes reaching ~ 110 cm^2/Vs. We also find that the long-range mobility within the film to be strongly suppressed by grain boundaries between the nanoflakes. Finally, we discover that photoexcitation with optical pulses results in a transient suppression of conductivity that persists for hundreds of picoseconds, and potentially longer. These properties suggest applications of $Ti_3C_2T_z$ in THz photonic devices, as discussed in Chapter 4.

2.2 Fabrication and characterization of $Ti_3C_2T_z$ film

$Ti_3C_2T_z$ was synthesized by selective etching of aluminum atomic layers in Ti_3AlC_2 MAX phase by the MILD etching method as described previously in §1-1 at Missouri Missouri University of Science and Technology by Shuohan Huang in Vadym Mochalin group. MXene thin film on quartz was fabricated from a concentrated $Ti_3C_2T_z$ colloidal solution via the interfacial film deposition method. About 100 μL of $Ti_3C_2T_z$ colloidal solution were mixed in 50 mL of DI water together with 5 mL of toluene added dropwise over 5−10 min of stirring. The dispersion was then poured directly into a beaker filled with 400 mL of DI water, and a piece of quartz substrate, hydrophilized using Piranha solution (3 mL of 30% H_2O_2 + 9 mL of 98% H_2SO_4), was placed at the bottom. After ~15 min, MXene film self-assembled between water and toluene. Quartz substrate was slowly lifted from the solution through the interface, forming a 25 ± 5 nm-thick film, as determined by profilometry (Figure 2-1 (c)). A representative atomic force microscopy (AFM) image of the film (Figure 2-1 (b)) shows that the film is continuous and consists of overlapping nanoflakes of sub μm lateral dimensions. The AFM image was acquired using Park NX20 AFM operated in tapping mode. Optical transmission of the film varies between 60% and 70% in the 400−900 nm range, suggesting a significant absorption despite the small thickness (Figure 1-5).

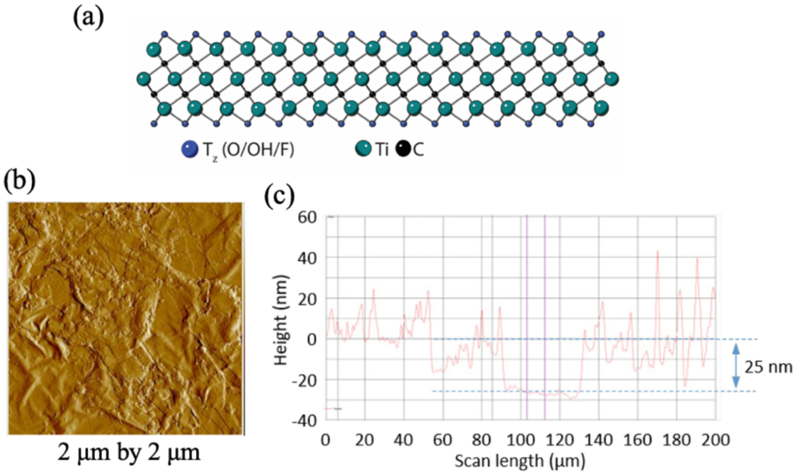

Figure 2-1(a) chemical structure of $Ti_3C_2T_z$ (b) 2 μm by 2 μm AFM image (c) Profilometer (P-7 stylus profiler, KLA Tencor) scan over a region where the film was removed down to the substrate. Average film thickness is 25 nm. Adapted with permission from [4], Copyright (2019) American Chemical Society

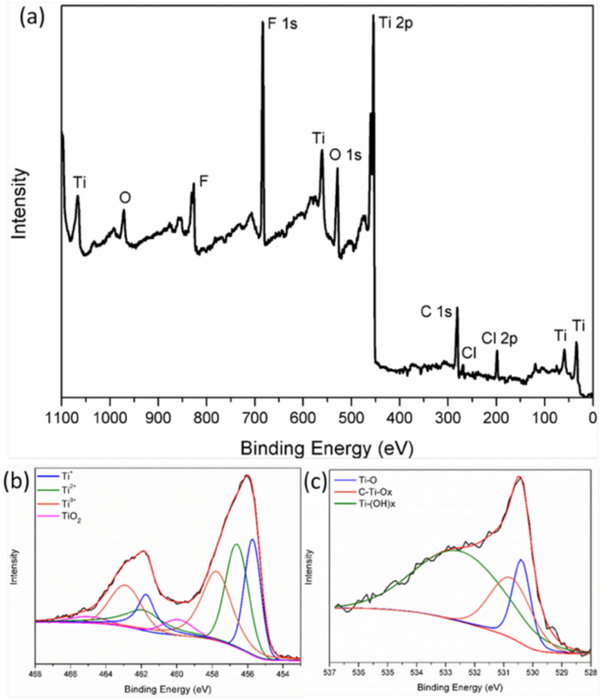

Figure 2-2 (*a) XPS survey for* $Ti_3C_2T_z$ *MXene. High-resolution XPS spectra of* $Ti_3C_2T_z$ *MXene for (b) Ti 2p and (c) O 1s. Adapted with permission from [22], Copyright (2019) American Chemical Society*

X-Ray photoelectron spectroscopy (XPS) using a KRATOS AXIS 165 X-ray photoelectron spectrometer with a monochromatic Al X-ray source was performed to characterize the surface chemistry of the $Ti_3C_2T_z$ MXene. The survey spectrum in Figure 2-2 (a) shows the a mix of -O, -OH, and -F terminations.

2.3 Intrinsic conductivity of $Ti_3C_2T_z$ film by THz-TDS

We used the THz-TDS in the transmission configuration (Figure 1-8). Comparing the amplitude and the phase of the THz pulses transmitted through the substrate alone and the sample on a substrate in the frequency domain, we calculate the complex THz conductivity ($\tilde{\sigma}(\omega)$) of the film using the relation Eq. 3 , where $Z_0 = 377\ \Omega$, and n is the refractive index of the quartz substrate is 2.156 in the THz range.[93] A comparison of the complex conductivity spectra of two MXene films, a continuous, 25 nm-thick film and a discondinous, ~ 16 nm-thick film composed of smaller nanoflakes[27] is shown in Figure 2-4. In both films, suppression of conductivity at low frequencies is consistent with long-range carrier transport impeded by the inter-flake boundaries. The Drude-Smith model (Chapter 1.2.3) captures this influence of the inter-flake boundaries and allows us to determine the density and mobility of the free carriers and characterize the impact of barriers such as nanoflake edges and defects on long-range carrier transport. Using zone-center electron effective mass of $0.2845m_e$, [28] we find that both films have the same large intrinsic carrier density, ~ $2\text{x}10^{21}$ cm^{-3}, in agreement with the value determined from electrical measurements on $Ti_3C_2T_z$ films.[94] However, the continuous film consisting of larger overlapping flakes has a much less negative *c*-parameter (-0.68 vs -0.97) and a approximately four times larger DC conductivity σ_{DC}~1100 (Ω cm)$^{-1}$. The Drude-Smith scattering time is also impacted by flake boundaries as it takes into account both the bulk scattering τ_{bulk} and characteristic time associated with grain boundary scattering $\tau_{boundary}$ as $1/\tau_{DS} = 1/\tau_{bulk} + 1/\tau_{boundary}$. We find that τ_{DS} decreases from 19±1 fs in a continuous film to 6±1 fs in a discontinuous one. From the scattering time, we can calculate the intrinsic carrier mobility, or mobility of carriers over the mesoscopic length scales within individual flakes, to be $\mu_{intrinsic} = \frac{e\tau_{DS}}{m^*} \approx 110$

cm^2/Vs in a continuous film, vs ≈34 cm^2/Vs in the discontinuos. The long range film mobility is further influenced by the inter-flake transport: $\mu_{long-range} = \mu_{intrinsic}(1+c) \approx 35$ cm^2/Vs in a continuos, and only ≈ 1cm^2/Vs in a discontinuous film. This comparison demonstrates that while $Ti_3C_2T_z$ is intrinsically metallic material with high carrier density, the film morphology viz. the size and overlap of individual flakes plays a critical role in film conductivity. Applications leveraging high MXene conductivity call for uniform films with large nanoflakes.

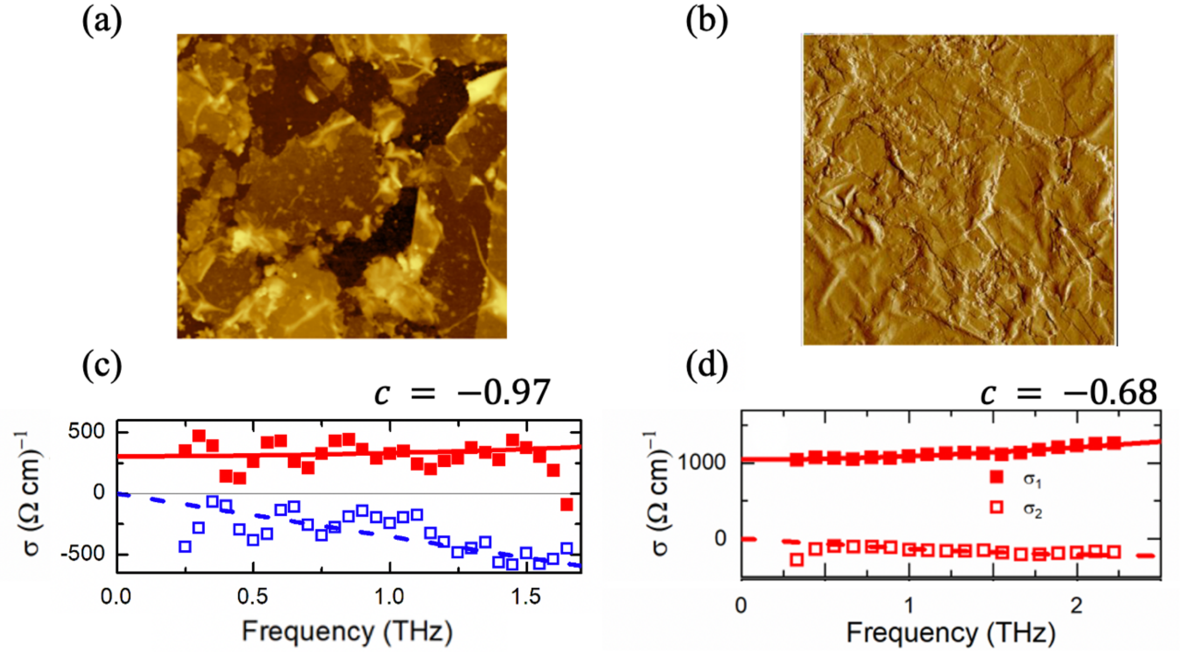

Figure 2-3 2 μm by 2 μm AFM images of sample 1 (a) (fabricated by Yunchang Dong from Clemson Univercity) and sample 2 (b), where sample 2 is more continuous. It is consistent with c factor fitted from THz conductivity. (c), (d) are experimental conductivity spectra for samples 1 and 2 (symbols), along with their fits to the Drude-Smith model (Eq. 11). Adapted with permission from [4], Copyright (2019) American Chemical Society.

2.4 Photoexcited carrier dynamics of $Ti_3C_2T_z$ film measured by OPTP

Using the OPTP setup in Figure 1-10, we find that both 800 and 400 nm light pulses enhance transmission of the THz pulses (Figure 2-4). According to Eq 12, the change of conductivity $\Delta\sigma$ is proportional to the negative change of THz transmission (– ΔT), thus the conductivity is suppressed by the optical excitation. The frequency-resolved transient change in conductivity at different times after excitation with 800 nm pulse in reveals that this suppression covers over the entire bandwidth of the THz probe, 0.25–2.25 THz, as shown in Figure 2-5 for 800 nm excitation.

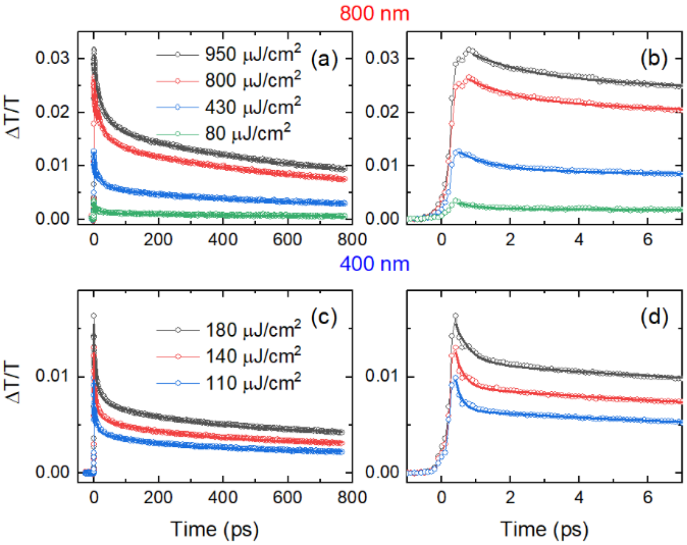

Figure 2-4 (a) Photoinduced change in the THz peak transmission as a function of time after photoexcitation with 800 nm (a, b) and 400 nm (c, d) pulses with excitation fluence values given in the legends. Panels (b) and (d) show expanded views of the initial decay profiles in (a) and (c). Thick solid lines are fits of the experimental data to the multi-exponential decays. (Data taken by thesis author at MAX Plank Institute for Polymer research, 2018) Reprinted with permission from [4], Copyright (2019) American Chemical Society

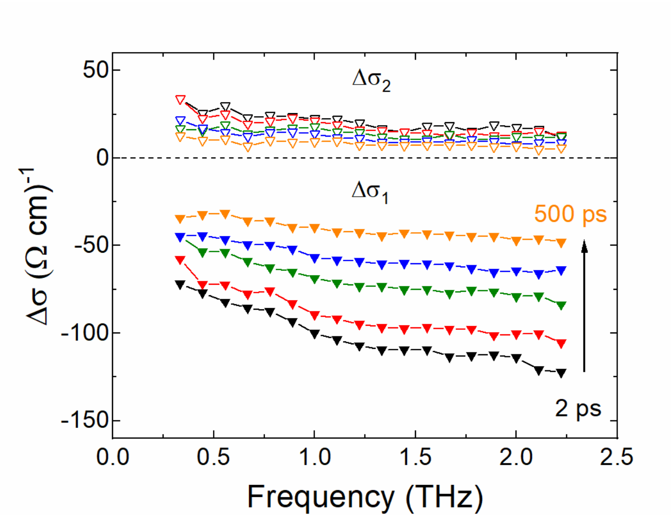

Figure 2-5 Photoinduced change in real (solid symbols) and imaginary (open symbols) conductivity as different times after excitation with 800 nm, 950 μJ/cm²pulse at 290 K. (Data taken by thesis author at MAX Plank Institute for Polymer research, 2018) Reprinted with permission from [4], Copyright (2019) American Chemical Society

The time-resolved dynamics of the observed suppression of conductivity (Figure 2-4) show a rapid onset of a photoinduced THz transparency immediately after the optical excitation at t=0, followed by its decay over the next hundreds of picoseconds.

We also observe that the decay dynamics differ for 800 nm and 400 nm excitation. To compare the effects of the two excitation wavelengths, we fit the experimental data in Figure 2-4 to a multi-exponential decay function. We find that including three decaying terms and a constant adequately captures the dynamics of the transient change in transmission in the experimental time window. Thus, the solid lines in Figure 2-4 are fits of the experimental data using the function $\frac{\Delta T(t)}{T} =$

$A_0 + A_1 \exp\left(-\frac{t}{t_1}\right) + A_2 \exp\left(-\frac{t}{t_2}\right) + A_3 \exp\left(-\frac{t}{t_3}\right)$, where, t_1, t_2, and t_3 are decay times, A_1, A_2, and A_3 are the corresponding amplitudes, and A_0 is the amplitude of transient component or components with long, > 1 ns decay times that cannot be accurately determined from our data. A summary of the fitting results for both excitation wavelengths is presented in Figure 2-6. The following observations can be made:

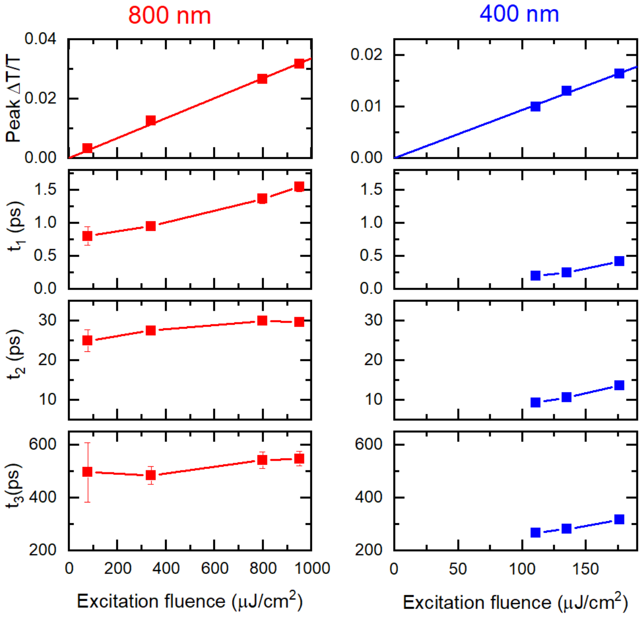

Figure 2-6 Fitting parameters resulting from fitting transient photoinduced THz probe peak transmission enhancement to a three exponential decay function: peak and decay times for 800 nm excitation (left, red symbols) and 400 nm excitation (right, blue symbols). Reprinted with permission from [4], Copyright (2019) American Chemical Society

- For both 800 nm and 400 nm pump excitations, the peak of transmission enhancement is linearly dependent on the excitation fluence in the fluence range studied here.
- The three decay times, t_1, t_2, and t_3, become longer with increasing excitation fluence.

- The three measured decay times are shorter for 400 nm excitation compared to 800 nm.

To understand the mechanism responsible for this long-lived suppression of conductivity in a thin MXene film, we look to other metallic systems that exhibit similar phenomena. Response of metals and semiconductors to an ultrafast optical excitation is qualitatively different. In semiconductors, positive photoconductivity is observed due to an increase in carrier density.[95] Transient conductivity changes in metals result from a combined effect of intra-band and inter-band transitions, with inter-band excitations playing a dominant role for photon energy above the inter-band transition threshold.[96-98] However, the inter-band excitation of a metal often does not lead to a significant change in the free carrier density. In this case, the sign of the photoinduced conductivity change is typically negative as it is dominated by a reduction of carrier mobility in response to the increase in carrier and lattice temperature.[83, 99] Ultrafast optical excitation generates a highly nonequilibrium population of electrons which rapidly (over sub-picosecond time scales) equilibrate by electron-electron scattering and form a Fermi distribution with a collective hot electron temperature T_e that can reach thousands of Kelvin above the lattice temperature.[96, 97, 100] Over the next ~ 1-10 ps time period, hot carrier bath cools and equilibrates with the lattice by carrier-phonon scattering, resulting in reduction of the electrical conductivity. The final stage of the recovery after ultrafast optical excitation is significantly slower (time scale ~ hundreds of picoseconds)[96, 97] as it is driven by sample cooling and is limited by the phonon diffusion and/or the thermal boundary resistance between the film and the substrate that supports it. Among 2D materials, reduction of conductivity after inter-band excitation with ultrashort optical pulses has been observed in highly doped or gated graphene, and explained by redistribution of energy from photoexcited electron-hole pairs to initially unexcited free electrons, resulting in their heating *via* either the direct conversion of excess energy into electronic heat or its dissipation into optical phonons.[101-103] The resulting reduction in conductivity recovers in ~ 2 ps, several orders of magnitude faster than the recovery time we observe in $Ti_3C_2T_z$ film.

For the ~ 25 nm thick MXene film composed of metallic $Ti_3C_2T_z$ nanoflakes, the transient conductivity suppression with excitation energies of 1.55 eV (800 nm) and 3.1 eV (400 nm) results in both intra- and inter-band carrier excitation that contribute to hot carrier generation by promoting carriers from the Fermi energy E_F into higher energy states (former) or by generating new electron-hole pairs (latter). Carrier-carrier scattering then establishes a hot carrier distribution with carrier temperature T_C that is higher than the lattice temperature T_L, followed by a rapid (~ picoseconds) equilibration of carrier and lattice temperature via the carrier-phonon scattering. The typical time scales for these processes are commensurate with the observed fast relaxation process t_1, suggesting that the initial fast recovery of conductivity suppression might indeed be due to the combined effect of these processes, i.e., carrier-carrier and carrier-lattice thermalization. Difference in t_1 for 400 nm and 800 nm excitation may then be explained by the dependence of the scattering rates on carrier excess energy, while lower t_1 at increased fluence may result from a more efficient screening of carrier-lattice interactions at higher carrier density.[104]

Ultimately, the end result of carrier-carrier and carrier-lattice equilibration, occurring over the first few picoseconds following ultrafast optical excitation, is an increased lattice temperature. Is this laser-induced transient heating responsible for the observed long-lived conductivity suppression in a $Ti_3C_2T_z$ film? Temperature-dependent measurements are needed to provide an answer.

2.5 Temperature dependent THz spectroscopy on photoexcited conductivity suppression of $Ti_3C_2T_z$ film

The thermal properties of $Ti_3C_2T_z$ films are still largely unexplored. A specific heat in the range of 1.1 – 1.5 MJ m^{-3} K, depending on termination T_z, has only been theoretically calculated for an isolated monolayer.[105] Measurements of thermal conductivity, which determines how quickly the photoexcited area would cool to ambient temperature, vary from 2.84 to 55.8 W m^{-1} K^{-1}.[106, 107] Thermal boundary conductance at ambient temperature between a $Ti_3C_2T_z$ film and a substrate, which governs heat flow from the photoexcited film to a substrate, has been recently reported for $Ti_3C_2T_z/SiO_2/Si$ interface to vary from 10 to 27 MW m^{-2} K^{-1} depending on the presence of absorbents.[108]

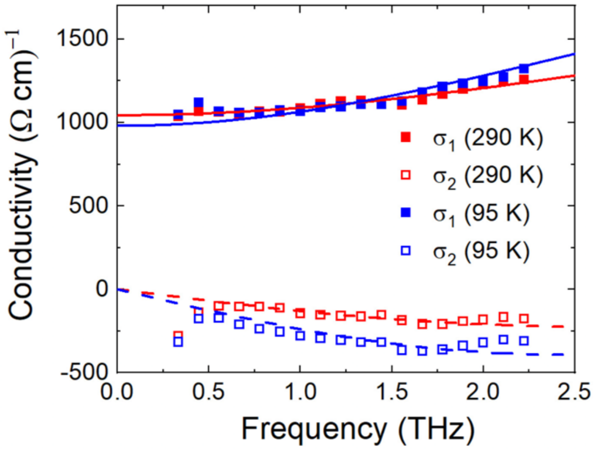

Figure 2-7 Complex THz conductivity (solid symbols represent real and open symbols – imaginary conductivity components; lines show a global fit of both components to the Drude-Smith model) at 290 K (red) and 95 K (blue). (Data taken by Naaman Amer at University of Alberta) Reprinted with permission from [4], Copyright (2019) American Chemical Society

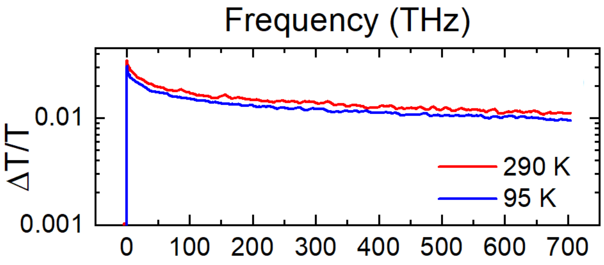

Figure 2-8 Transient change in transmission of THz probe pulse peak after excitation with 800 nm, 950 μJ/cm²pulse at 290 K and 95 K. (Data taken by Naaman Amer at University of Alberta) Reprinted with permission from [4], Copyright (2019) American Chemical Society

Temperature-dependent measurements of electrical conductivity of $Ti_3C_2T_z$ films have shown that conductivity either remains unchanged when the temperature is varied from 80 K to room temperature, or increases by only a few percent with increasing temperature.[106, 109, 110] Here, THz-TDS and optical (800 nm) pump-THz probe spectroscopy measurements at 95 K were carried out at University of Alberta by Naaman Amer in Frank Hegmann group. First, we find that the complex THz conductivity exhibits very little change when the film temperature is reduced from 290 K to 95 K (Figure 2-7), with the real conductivity component being unchanged. This finding agrees with conventional temperature-dependent measurements of $Ti_3C_2T_z$ DC conductivity.[106, 109, 110]

Secondly, we observe that the relaxation dynamics of the optical excitation-induced reduction in conductivity is not sensitive to a temperature change from 290 K to 95 K (Figure 2-8). This result effectively rules out the slow cooling of the photoexcited film by transferring heat to the substrate or laterally, to unexcited portions of the film, as a reason for the slow relaxation of the optically-induced THz transparency. Parameters such as thermal conductivity and thermal boundary conductance are expected to be temperature dependent, and in fact, the study that found little to no change in the electrical conductivity between 95 K and 290K, also found that the thermal conductivity changes by more than a factor of 2.[106] We therefore conclude that, while the lattice temperature must be increased by the photoexcitation, it does not play a major role in conductivity suppression in metallic MXenes, unlike conventional metals, and cannot explain the observed phenomenon of transient conductivity suppression by optical pulses.

Additional experiments as well as theoretical investigations of the ultrafast photoexcitations in metallic MXenes are necessary to uncover the mechanisms reponsible for this remarkably long-lived conductivity suppression. With future studies in mind, we put forth the following hypothesis: the complete picture of the photoinduced effects in MXenes must necessarily consider the role played by the terminations, T_z (F, OH, O, and their combinations). Multiple studies conclusively showed that MXene surface chemistry plays an important role in transport properties.[29, 110-114] Specifically, fluorine enhances conductivity compared to the bare Ti_3C_2 by introducing additional extended electronic states outside titanium carbide cores, while the termination of the surface by the oxygen introduces localized states near the oxygen and carbon and reduces overall conductivity.[29, 111, 113] Moreover, since MXenes are reactive towards water, their surface chemistry and composition may change over time.[115] DFT calculations have also shown that optical absorption in the 1.0 – 4.5 eV range is significantly lower in F and OH terminated Ti_3C_2 compared to the bare and O-terminated one.[116] Typically, $Ti_3C_2T_z$ features a combination of all of these terminations. It is then possible that optical excitation with 1.55 eV (800 nm) or 3.1 eV (400 nm) photons excites some of the localized states associated with specific surface terminating groups. The resulting localized charges on the nanoflake surface change the electrostatic potential profile within the conductive cores, which has been theoretically predicted to impact transport properties.[111] The origin of the long-lived conductivity suppression may be the relaxation of those localized surface excitations occuring over hundreds of picosecond or longer. Differences in optical absorption at 400 nm and 800 nm for different surface-related localized states may then explain the variation in relaxation dynamics of conductivity suppression for these two excitation wavelengths, while the slowing of the relaxation at higher excitation fluence may turn out to result from saturation of the intermediate states that take part in relaxation. Future experimental studies with $Ti_3C_2T_z$ films with specific, well-defined surface terminations, as well as more detailed theoretical investigations of their optical and transport properties, will resolve these unanswered questions.

2.6 Conclusion

We have investigated equilibrium and non-equilibrium dynamics of charge carriers in $Ti_3C_2T_z$ nanoplatelets. We find that the nanoplatelets are metallic, with a high (~ 2×10^{21} cm^{-3}) intrinsic charge carrier density and can reach high (~ 110 cm^2/Vs) mobility of carriers within individual nanoplatelets. High carrier density gives rise to exceptionally large, ~ 2.2×10^5 cm^{-1} absorption in the THz range, putting $Ti_3C_2T_z$ forth as a potential THz detector material. The ultrashort 400 nm and 800 nm optical pulses can suppress the conductivity of $Ti_3C_2T_z$ up to nanoseconds and that is independent of temperature from at least 95 K to the room temperature. These unique properies makes this new 2D material an attractive candidate for THz modulation devices and variable electromagnetic shielding applications, which will be discussed in Chapter 4.

Acknowledgements:

MXene films for this work were provided by S. Huang and V.M. Mochalyn at Missouri University of Science and Technology. G.L. thanks Worcester

Polytechnic Institute PhD Global Research Experience Award that allowed investigations of $Ti_3C_2T_z$ conductivity in collaboration with Dr. H. Hafez in the laboratory of Dr. D. Turchinovich in Max Plank Institute for Polymer Research. We thank Helma Burg for help with profilometer measurements and Uwe Rietzler for help with AFM measurements, and Dr. Y. Gogotsi at Drexel University for helpful discussions. Work at Turchinovich lab was partly supported by the project “Nonequilibrium dynamics in solids probed by terahertz fields” funded by the Deutsche Forschungsgemeinschaft (DFG, German Research Foundation) – Project nummer 278162697 – SFB 1242. Low temperature measurements were carried out by Dr. N. Amer in Dr. F.A.Hegmann’s laboratory at the University of Alberta, and were supported by funding from NSERC, CFI, and the Alberta Innovates Strategic Chairs Program, and technical support from B. Shi.

3 Equilibrium and non-equilibrium free carrier dynamics in 2D Mo-MXenes: $Mo_2Ti_2C_3T_z$ and $Mo_2TiC_2T_z$

3.1 Introduction:

The first discovered MXene, $Ti_3C_3T_z$, is metallic, with a high density of free carriers and conductivity, as discussed in Chapter 2. However, MXene electronic properties have been theoretically predicted to span the range from highly conductive metallic to semimetallic, semiconducting, and even topological insulator[29, 35, 110, 117-120]. This wide variety of anticipated properties and potential applications underscores the need to understand the mechanisms of carrier transport in MXenes as a function of their chemical composition, terminations, and processing method. Here, we have focused our attention on two Mo-based MXenes: $Mo_2Ti_2C_3T_z$ and $Mo_2TiC_2T_z$ for which synthesis has been well established in the laboratory of our collaborators, group led by M.W. Barsoum at Drexel University[35, 117]. Their structure is similar to that of $Ti_3C_3T_z$, but with some of the Ti atoms replaced with Mo. In $Mo_2Ti_2C_3T_z$, Mo to Ti ratio is 1:1, and in $Mo_2TiC_2T_z$ it is 2:1 (Figure 3-1 a, b). In addition, $Mo_2Ti_2C_3T_z$ has n=3, and therefore an additional layer of atoms is present. This way, comparing the THz conductivity in $Ti_3C_3T_z$, $Mo_2Ti_2C_3T_z$, and $Mo_2TiC_2T_z$ allows drawing conclusions about the role of both M and *n* on optoelectronic properties. Using THz spectroscopy, we find that both Mo-containing MXenes have high, albeit lower $Ti_3C_3T_z$, intrinsic carrier densities (~ 10^{20} cm^{-3} in $Mo_2Ti_2C_3T_z$ and ~ 10^{19} cm^{-3} in $Mo_2TiC_2T_z$) and mobilities, and exhibit high conductivities within individual nanosheets. Optical excitation results in a transient conductivity increase in both Mo-based MXenes, in stark contrast with the $Ti_3C_2T_z$ where photoexcitation suppresses conductivity for nanoseconds (Chapter 2). We also discover that microscopic conductivity and the lifetime of photoexcited carriers in these materials are highly sensitive to the presence of water and other species in van der Waals gaps between the nanosheets forming MXene films. Deintercalation of those species by mild vacuum annealing (Figure 3-1, c) improves the long-range, inter-nanosheet transport of the photoexcited carriers and increases their lifetime. The possibility of engineering intrinsic and photoinduced conductivity by substituting Mo for Ti renders Mo-based MXenes attractive for a variety of optoelectronic, sensing, and photoelectrochemical applications.

In MXene films, water molecules and cations occupy the space between individual MXene nanosheets and can affect transport properties, such that removing them by annealing often can lead to dramatic changes in transport properties[35, 110]. The transport properties of MXene films result from a complicated interplay of intra-nanosheet carrier transport determined mainly by the properties of the $M_{n+1}X_n$ cores and affected by their point and other defects, and long-range, inter- nanosheets transport. Inter-nanosheet carrier motion is sensitive not only to the nature of the T_z, but also to the properties of the nanosheet edges and any species intercalated between the nanosheets.

Studies have demonstrated that not only are individual $Ti_3C_2T_z$ MXenes metallic with a high carrier density and mobility, consistent with DFT calculations that predict high density of states at the Fermi level E_F, but macroscopic $Ti_3C_2T_z$ films retain metallic-like conductivity with positive dR/dT over a broad temperature range[110, 118](Chapter 2). The metallicity is also evidenced by single nanosheet measurements[94]. However, the situation is more complicated in molybdenum, Mo-based MXenes. While non-spin-polarized DFT calculations predict that Mo-Ti MXenes are metallic with significant DOS at the E_F,[6] accounting for spin polarization opens of a small (tens of meV) gap in -OH and -F terminated Mo-MXenes but not in O-terminated Mo-MXenes[118]. Experiments have shown that replacing some or all of Ti with Mo in a MXene structure results in a lower carrier density, and a semiconductor-like behavior has been reported in several studies of multi-layer Mo-MXene films as resistivity showed a slow increase at lower temperatures ($dR/dT<0$)[6, 35, 110, 118]. Systematic temperature-dependent magneto-transport measurements of Mo-based MXenes revealed that they behave like disordered systems, unlike granular metals. Their long-range conductivity is limited by the inter-nanosheet carrier transfer which occurs mainly by variable range hopping (VRH), with a contribution from a thermally-activated mechanism at higher temperatures[35]. These experiments also demonstrated that conductivity is strongly dependent on inter-nanosheet distance, and increases by orders of magnitude when annealing reduces this distance by releasing the water and other intercalants from the inter- nanosheet spaces. Finally, vacuum annealing $Mo_2TiC_2T_z$ at temperatures that are sufficiently high to eliminate most intercalated species (up to 775 °C) was found to reverse the sign of dR/dT from negative to positive (metallic-like), establishing the intra-nanosheet metallicity of $Mo_2TiC_2T_z$, and demonstrating that the dR/dT <0 behavior of multi-layer Mo-MXenes is most probably caused by the inter-nanosheet species.[110] Yet, an exact picture of the microscopic conductivity and charge carrier dynamics in Mo-MXenes, remains incomplete. we exploit the ability of THz spectroscopy to glean information about both inter-nanosheet and intra-nanosheet contribution to conductivity to investigate the microscopic conductivity and carrier dynamics in two Mo-based MXene, $Mo_2Ti_2C_3T_z$ and $Mo_2TiC_2T_z$ (Figure 3-1 (a, b)) films. Earlier transport measurements

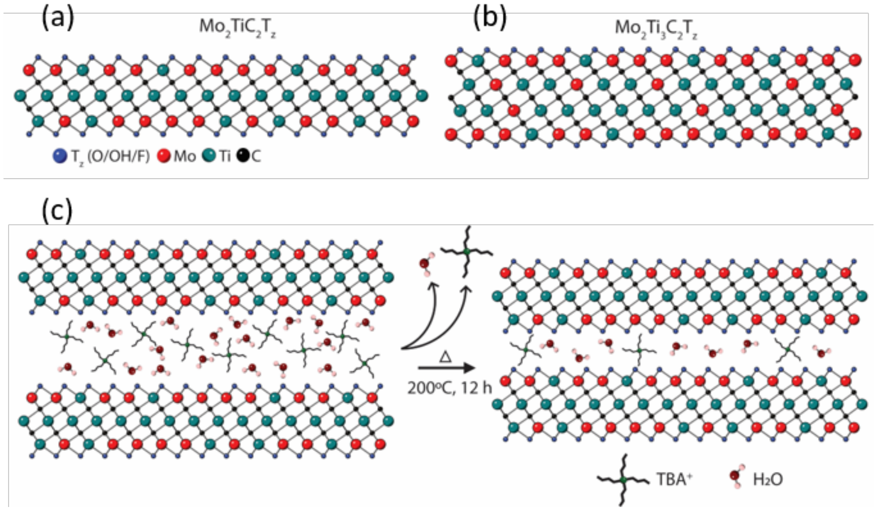

Figure 3-1. Schematic depiction of (a) Mo_2TiC_2Tz and (b) $Mo_2Ti_2C_3T_z$ structure. (c) Effect of vacuum annealing on a film structure and inter-nanosheet distance. Reprinted with permission from [3], Copyright (2020) American Chemical Society

demonstrated that intercalation of water and tetrabutylammonium cations (TBA^+) between the nanosheets that occurs during film preparation increases the inter-nanosheet spacing and electrical resistance, resulting in negative dR/dT values.[35] Vacuum annealing has been found to increase conductivity and reduce the inter-nanosheet distances by releasing some of the intercalants (Figure 3-1 (c))[35, 110]. In this study, we investigated how a mild (200 °C) vacuum annealing impacts the transport property of the two Mo-based MXenes. The main finding of this work is a dramatically different response of metallic Mo- based MXenes to photoexcitation compared to that in $Ti_3C_2T_z$. Unlike $Ti_3C_2T_z$., where optical excitation suppresses conductivity, it results in a long-lived positive photoconductivity in both $Mo_2Ti_2C_3T_z$ and $Mo_2TiC_2T_z$. We hypothesize that over an order of magnitude lower intrinsic carrier density (~ 10^{20} cm^{-3} vs ~ 10^{21} cm^{-3} in $Ti_3C_2T_z$) makes the inter-band carrier excitation the most pronounced effect of photoexcitation on conductivity in Mo-based MXenes. An ultrafast 800 nm optical pulse injects a population of electrons (holes) into delocalized bands at the energies above (below) the Fermi level, E_F. We find that these extrinsic carriers are less affected by the inter-nanosheet boundaries compared to the intrinsic carriers at E_F. Transient photoconductivity then decays over tens and hundreds of ps, as injected carriers are trapped at defect states, thermalize with the intrinsic carriers and recombine. Annealing further improves the long-range, inter-nanosheet transport of the photoexcited carriers and increases their lifetime. These findings highlight the broad range of optoelectronic properties of metallic MXenes, where substituting Ti for Mo at some of the transition metal sites and changing the inter-layer spacing by annealing can be used to engineer transient photoconductive response.

3.2 Mo-MXene film fabrication

The samples for this study were provided by V. Natu and M.W. Barsoum at Drexel University. Precursor MAX powders (Mo_2TiAlC_2 and $Mo_2Ti_2AlC_3$) were ball milled and heated under flowing argon (Ar) at 1600°C to achieve loosely sintered blocks. Blocks were ground using a milling bit on a drill press and the resulting powders passed through a 400 mesh (particle size < 38 μm) sieve[6]. The resulting MAX phases were etched in 50% HF solution to remove Al layers, resulting in a MXene-containing slurry, which was washed repeatedly in de-ionized water, ethanol, and tetrabutylammonium hydroxide to disperse the nanosheets. Detailed fabrication procedure is described in [3]. For the THz measurements, a ~ 80 nm thick film of $Mo_2Ti_2C_3T_z$ was spin-coated onto 1 mm thick quartz substrates (Figure 3-2). XRD patterns of this film showed that the d-spacing between nanosheets was 3.2 nm. Since we could not achieve a sufficiently

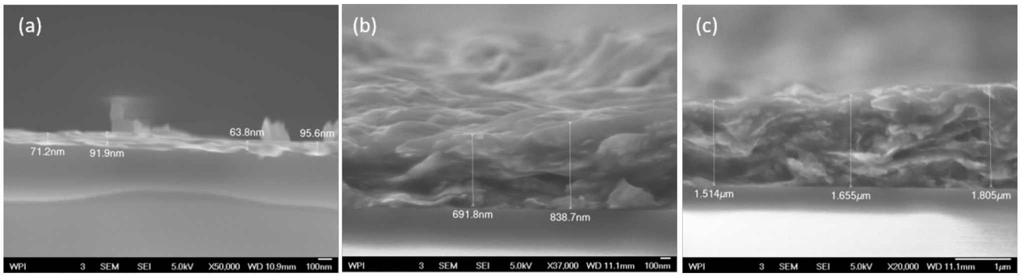
(a)
71.2nm
91.9nm
63.8nm
95.6nm
WPI 3 SEM SEI 5.0kV X50,000 WD 10.9mm 100nm
(b)
691.8nm
838.7nm
WPI 3 SEM SEI 5.0kV X37,000 WD 11.1mm 100nm
(c)
1.514μm
1.655μm
1.805μm
WPI 3 SEM SEI 5.0kV X20,000 WD 11.1mm 1μm

Figure 3-2 Representative SEM images for (a) spin coated $Mo_2Ti_2C_3T_z$ and (b, c) drop case $Mo_2TiC_2T_z$ films. For each sample, multiple images were analyzed and the average thickness was determined to be 80 ± 20 nm for $Mo_2Ti_2C_3T_z$ and 1300 ± 500 nm for $Mo_2TiC_2T_z$. Reprinted with permission from [3], Copyright (2020) American Chemical Society

concentrated colloid for the $Mo_2TiC_2T_z$ composition for spin coating, we drop-

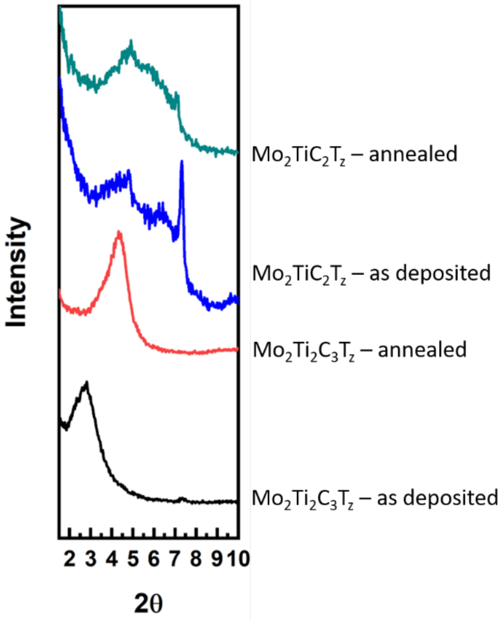

Figure 3-3 XRD diffraction patterns of Mo-based films before and after annealing at 200 °C. Reprinted with permission from [3], Copyright (2020) American Chemical Society

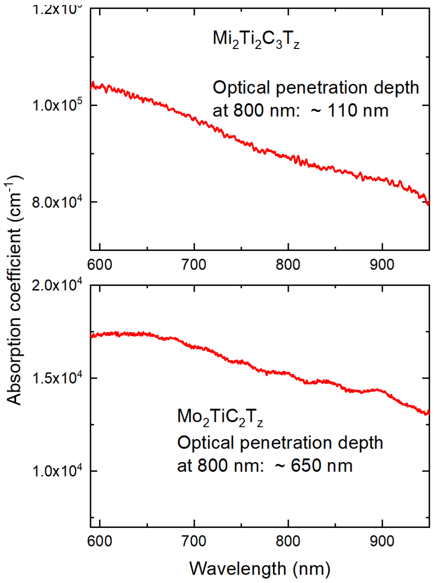

Figure 3-4 UV-VIS spectroscopy of MXene films. Optical penetration depth at 800 nm was used in TRTS analysis to estimate the photoexcited layer thickness. For the $Mo_2Ti_2C_3T_z$ film, the optical penetration depth is larger than the average film thickness, and therefore the film thickness was used. Reprinted with permission from [3], Copyright (2020) American Chemical Society

cast the colloidal suspension directly onto a quartz substrate to yield a thicker (~ 1300 nm Figure 3-2 (b), (c)) which XRD diffraction indicated contained some un-reacted Ti_3AlC_2 (see Figure 3-2). The optical absorption coefficient (Figure 3-4) for this composition is lower than that for $Mo_2Ti_2C_3T_z$. Samples were cut in half, and one part of each sample was annealed for 12 h in a vacuum (< 20 mTorr) at 200 °C to study the effect of annealing on the films. XRD patterns were obtained after annealing and compared to those before annealing. They show that upon annealing the d-spacing of the $Mo_2Ti_2C_3T_z$ sample decreased from 3.2 nm to 2.0 nm, while the $Mo_2TiC_2T_z$ films did not show a clear change in spacing.

3.3 THz TDS: intrinsic microscopic conductivity

THz TDS measurements were performed as described in Chapter 1. At normal incidence, THz pulses probe conductivity parallel to the substrate, and therefore

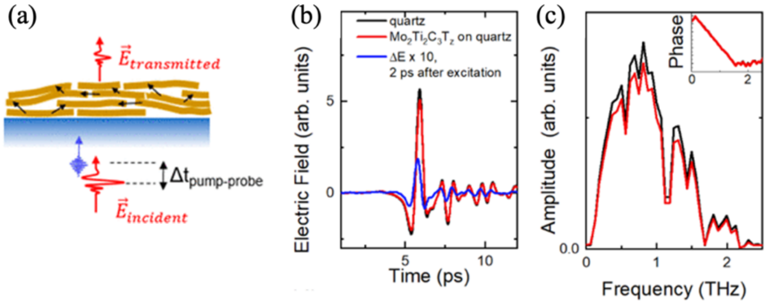

Figure 3-5 (a) Probing motion of photoexcited carriers in the $Mo_2Ti_2C_3T_z$ MXene nanosheet by THz probe pulses. (b) THz waveforms transmitted through the substrate, through a MXene film on a quartz substrate, and the photoinduced change in the transmitted waveform 2 ps after excitation with ~ 256 μJ/cm², 800 nm pulse. Comparing in the frequency domain the magnitude and phase (c) of THz pulses transmitted through the substrate with and without a MXene film yields a complex conductivity $\tilde{\sigma}(\omega) = \sigma_1 + i\sigma_2$. Adapted with permission from [3], Copyright (2020) American Chemical Society mainly in the basal plane of nanosheets comprising the MXene films (Figure 3-5 (a)), which is particularly relevant electronic as transport in MXenes predominantly occurs within the conductive cores of 2D sheets.[121] Example THz TDS experimental data for $Mo_2Ti_2C_3T_z$ MXene film is shown in Figure 3-5 (b) and (c). THz probe pulses transmitted through the film on the quartz substrate are attenuated compared to the pulses transmitted through the substrate alone (Figure 3-5 (b)), and the THz amplitude in the frequency domain (Figure 3-5 (c)) is lower.

Complex, frequency-resolved THz conductivity for both MXenes before and after a mild (200 °C) anneal in vacuum are shown in Figure 3-6. Comparing the

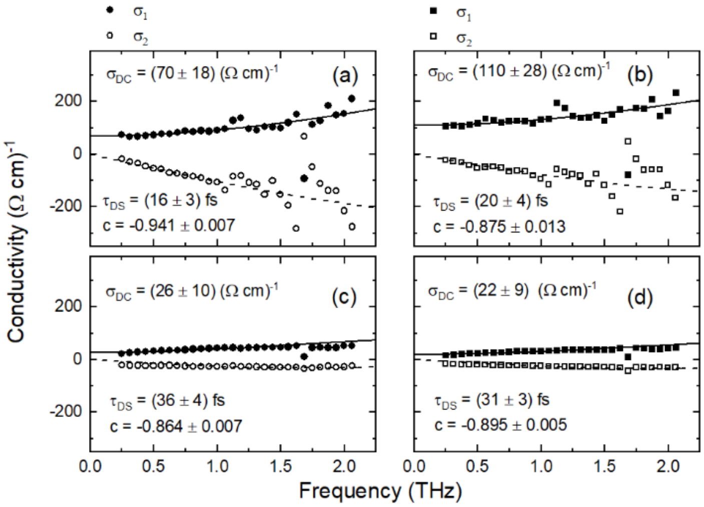

Figure 3-6 THz TDS of $Mo_2Ti_2C_3T_z$, (a) as deposited and (b) after a 200 °C vacuum annealing. (c) same as (a) but for $Mo_2TiC_2T_z$, (d) same as (b) but for $Mo_2TiC_2T_z$. Solid symbols represent real, and open symbols – imaginary conductivity, with lines showing global fits of the experimental data to the Drude-Smith model (Eq. 1) with parameters σ_{DC}, τ_{DS}, and c indicated on individual panels. Reprinted with permission from [3], Copyright (2020) American Chemical Society.

magnitude of the real conductivity (σ_1, solid symbols) in $Mo_2Ti_2C_3T_z$ and $Mo_2TiC_2T_z$, we observe that the increase in the fraction of Mo reduces conductivity in MXene films, an observation that is consistent with DC electronic measurements[35, 121]. Analysis of the spectral shape of complex frequency-resolved conductivity shows that carrier transport in the films is strongly impacted by the nanosheet edges and disorder, which manifests as a real conductivity suppressed at low frequencies and a negative imaginary component. Like in the case of $Ti_3C_2T_z$ film, we analyze the spectral data using the Drude-Smith model (Eqs. 6-8), and find that the c-parameter is ≈ -0.9, consistent with suppression of long-range conduction.[76, 78, 85, 86, 122]

We find that both $Mo_2Ti_2C_3T_z$ and $Mo_2TiC_2T_z$ have considerable densities of free, delocalized carriers that attenuate the THz probe pulses via free carrier absorption. As effective carrier masses for these materials are not yet know, we assume $m^* \approx m_e$ and estimate that intrinsic carrier densities to be ~ $2.5\text{x}10^{20}$ cm^{-3} for $Mo_2Ti_2C_3T_z$ and ~ $0.2\text{x}10^{20}$ cm^{-3} for $Mo_2TiC_2T_z$. DFT calculations for oxygen-terminated Mo-MXenes, $Mo_2Ti_3C_2O_2$, and $Mo_2TiC_2O_2$ yield the density of states at E_F ≈ 3 times higher than the former consistent with the observed trend.[118] While the carrier density values we find in Mo-MXenes are significantly lower compared to $Ti_3C_2T_z$ films,[27, 94] they nonetheless confirm metallic nature in individual sheets.[35, 110] We also estimate that intrinsic, intra-nanosheet mobility in $Mo_2Ti_2C_3T_z$ is $\mu_{short-range}$~ 30 cm^2/Vs, while the long-range, inter-nanosheet mobility is ~ 17 times lower. In $Mo_2TiC_2T_z$ film, $\mu_{short-range}$~ 60 cm^2/Vs, and long-range mobility is ~ 8 times lower. This observation of the suppressed inter-nanosheet transport agrees with the temperature-dependent conventional DC conductivity measurements where a variable-range and thermally-activated hopping model is hypothesized as inter-nanosheet transport mode [35] . We also find that despite a shorter relaxation time and a stronger suppression of inter-nanosheet conductivity, $Mo_2Ti_2C_3T_z$ is more conductive compared to $Mo_2TiC_2T_z$, owing to over an order of magnitude higher free carrier density.

We also observe that, at ~ 30 cm^2/Vs, the intrinsic, intra-nanosheet conductivity of $Mo_2Ti_2C_3T_z$ is half that of $Mo_2TiC_2T_z$. To explain this observation we refer to a recent XPS study on the Mo-based MXenes that showed that the Mo atoms in the outer layers of individual sheets are dissolved during the etching procedure, leaving behind vacancies, [123] and that more Mo atoms are present in outer layers in $Mo_2Ti_2C_3T_z$ where they are susceptible to etching.

Comparing the spectra before and after 200 °C annealing of the films in vacuum, which is known to remove water and other species that become intercalated between the MXene layer, we find that annealing almost doubles the intrinsic conductivity in a $Mo_2Ti_2C_3T_z$ film but has a minimal effect on intrinsic THz conductivity in $Mo_2TiC_2T_z$. From XRD diffraction of the $Mo_2Ti_2C_3T_z$ films before and after annealing (Figure 3-2) we found that the d-spacing decreases from 3.2

nm to 2.0 nm. This change is consistent with the increase in conductivity observed upon annealing. On the other hand, we were not able to reach any conclusions about the effect of annealing on interlayer spacing in the other MXene.

3.4 OPTP: effect of photoexcitation on microscopic conductivity

The transient photoconductivity dynamics after photoexcitation with 800 nm, 100 fs pulses are summarized in Figure 3-7 and Figure 3-8 for $Mo_2Ti_2C_3T_z$, and $Mo_2TiC_2T_z$ films, respectively. The first important observation is the positive sign of the transient conductivity change in both films, in stark contrast to our previous results for the metallic $Ti_3C_2T_z$ (Chapter 2).[27] Both $Mo_2Ti_2C_3T_z$ and $Mo_2TiC_2T_z$ are intrinsically metallic, albeit with a lower free carrier density. This transient increase in conductivity in response to optical excitation suggests that inter-band excitations inject a new population of free carriers (electrons and holes) into delocalized states above (or below, in the case of holes) E_F.

Just like the intrinsic conductivity, the observed photoconductivity peak immediately after optical excitation is higher in $Mo_2Ti_2C_3T_z$ compared to $Mo_2TiC_2T_z$. At the same excitation fluence (256 μJ/cm^2), change in transmission of the THz pulse peak is nearly three times stronger despite the thickness of the film being significantly smaller in the $Mo_2Ti_2C_3T_z$ case. In both films, optical penetration depth at 800 nm is comparable to the film thickness (Figure 3-4), and most of the 800 nm pump is absorbed over the thickness of the film. The smaller peak photoconductivity in $Mo_2TiC_2T_z$ suggests that a large fraction of photo-injected free carriers is trapped or recombine over time scales that are beyond the time resolution of our measurements, ~ 300 fs. Overall, comparing

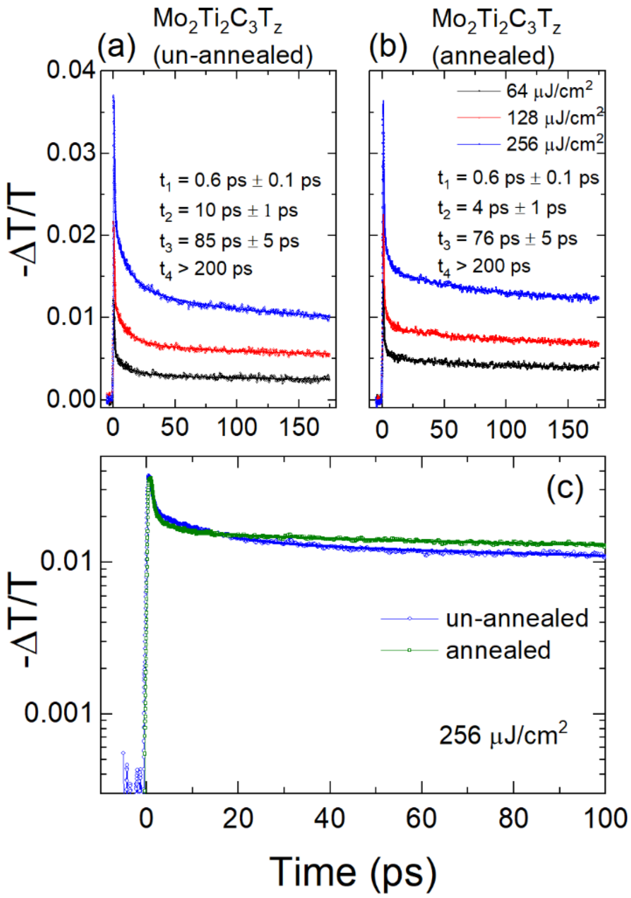

Figure 3-7 Transient photoconductivity in $Mo_2Ti_2C_3T_z$ ($-\Delta T/T \propto \Delta\sigma$) : photoconductivity decays following excitation with 800 nm, 100 fs pulses with different fluence values, as indicated in the legend, for (a) un-annealed, as-deposited film and (b) film annealed in vacuum at 200°C. Experimental data are fitted to a multi-exponential decay, and resulting decay times, which are fluence-independent, are given in panels. (c) Comparison of the transient photoconductivity decay for un-annealed and annealed films. Reprinted with permission from [3], Copyright (2020) American Chemical Society

the transient photoconductivity for the un-annealed $Mo_2Ti_2C_3T_z$ and $Mo_2TiC_2T_z$ films, we find that the lifetimes of the photoexcited excess free carriers is much longer in $Mo_2Ti_2C_3T_z$, with a photoconductivity at 100 ps after the excitation at nearly a third of the peak value. In the $Mo_2TiC_2T_z$ film, that value is < 10% which suggests a higher density of defect trap states that can efficiently capture photoexcited free carriers in this film.

In both films, we find that photoconductivity relaxation can be described by a multi-exponential decay, suggesting existence of multiple relaxation channels such as carrier-carrier scattering, thermalization with the intrinsic carriers, trapping at defect sites, and eventually, recombination.

The fastest decay component, $t_1 \sim 0.6$ ps in both samples, becomes more pronounced with increased excitation fluence (and thus number of optically injected free carriers) and is un-affected by annealing. We attribute it to rapid, carrier density-dependent processes such as carrier-carrier scattering and, possibly, Auger recombination.

In $Mo_2Ti_2C_3T_z$, we resolve three more decay slower components, one on the order of ps, another, on the order of tens of ps, and a significantly slower one (>200 ps) that we cannot measure accurately as it extends well beyond our experimental range. The specific decay times are not affected by the excitation fluence in the studied range, and the contribution of the individual exponential components scale linearly with the fluence. In $Mo_2TiC_2T_z$, two more decay components are observed in addition to the fastest, ~ 0.6 ps decay. One of them decays over tens of picoseconds, and another one – over >200 ps. It is reasonable to expect that similar carrier relaxation and trapping processes are present in both materials; in this case, the relaxation process that we do not directly

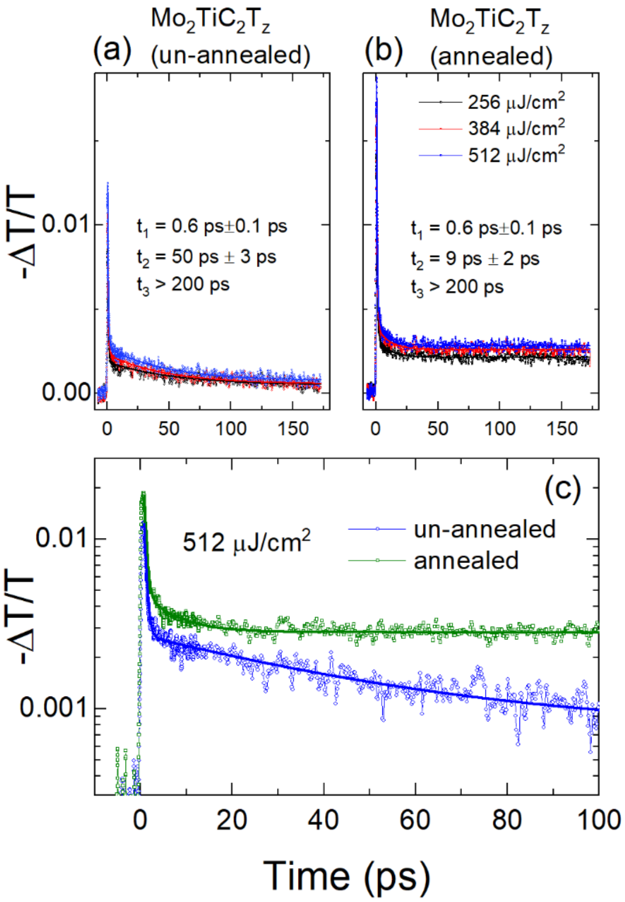

Figure 3-8 Transient photoconductivity in $Mo_2TiC_2T_z$ ($-\Delta T/T \propto \Delta\sigma$) : photoconductivity decays following excitation with 800 nm, 100 fs pulses with different fluence values, as indicated in the legend, for (a) un-annealed, as-deposited film and (b) film annealed in vacuum at 200°C. Experimental data are fitted to a multi-exponential decay, and resulting decay times are given in the graphs. (c) Comparison of the transient photoconductivity decay for un-annealed and annealed films. Reprinted with permission from [3], Copyright (2020) American Chemical Society

observe in $Mo_2TiC_2T_z$ may occur over a much shorter time scale, beyond our experimental time resolution.

Finally, annealing at 200°C, which has previously been shown to remove the water molecules and TBA^+ ions trapped between the nanosheets in the film and decrease the inter-nanosheet distance,[35, 110] has only a minor effect on the magnitude of photoconductivity of both films but leads to significant changes in the photoconductivity dynamics and free carrier lifetime. In both films, decay times of the processes that occur over ps to tens of ps shorten, while the slowest component (>200 ps) becomes more pronounced, as can be seen particularly

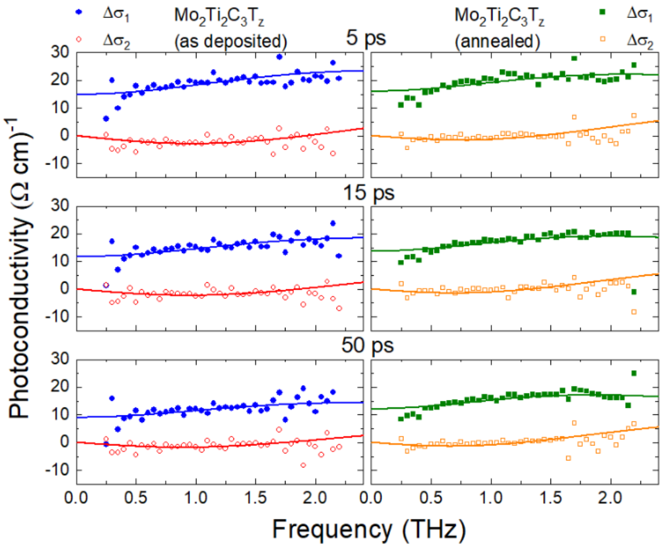

Figure 3-9 Photoinduced change in complex THz conductivity in $Mo_2Ti_2C_3T_z$ at different times after excitation with excitation with ~ 256 µJ/cm^2, 100 fs, 800 nm pulses for an un-annealed (left) and annealed (right) films. Solid and open symbols show real, and imaginary conductivity components, respectively. Lines are fits of experimental data to Drude-Smith model. Reprinted with permission from [3], Copyright (2020) American Chemical Society

clearly in the semi-log plots in Figure 3-7(c) and Figure 3-8(c). The changes are much more dramatic in the case of $Mo_2TiC_2T_z$.

Analyzing the frequency-resolved, complex photoconductivity spectra provides additional insight into the transient photoconductivity (Figure 3-9). Like the intrinsic conductivity, transient conductivity spectra can be analyzed using the Drude-Smith formalism (Eqs. 6-9).

In TRTS, the unexcited sample serves as a reference. The photoconductivity spectra at a specific time after photoexcitation provide information about the excitation-induced changes to the microscopic conductivity due to inter-band

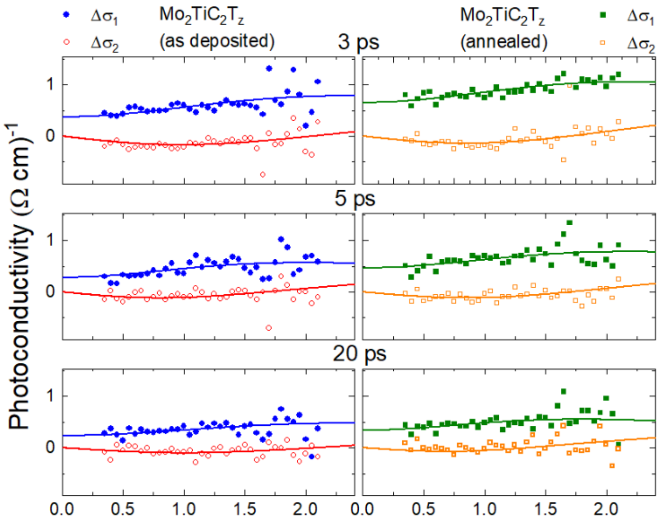

Figure 3-10 Photoinduced change in complex THz conductivity in $Mo_2TiC_2T_z$ at different times after excitation with excitation with ~ 512 $\mu J/cm^2$, 100 fs, 800 nm pulses for an un-annealed (left) and annealed (right) films. Solid and open symbols show real, and imaginary conductivity components, respectively. Lines are fits of experimental data to Drude-Smith model. Reprinted with permission from [3], Copyright (2020) American Chemical Society

excitation of new carriers as well as the changes in mobility of existing carriers by intra-band excitation and thermalization between the intrinsic and photoinjected carriers. The photoconductivity spectra at three different times (5 ps, 15 ps, and 50 ps) after excitation for $Mo_2Ti_2C_3T_z$ films are shown in Figure 3-9 both before annealing (left panels) and after annealing (right). Figure 3-10 shows the photoconductivity spectra at three times (3 ps, 5 ps, and 20 ps) for the un-annealed and annealed $Mo_2TiC_2T_z$ films.

For both MXenes, the shape of the photoconductivity spectra differs from the intrinsic conductivity. Analyzing the photoconductivity spectra using the Drude-Smith model, we find that the photoexcitation injects a population of free, delocalized carriers (electrons and holes) that have longer scattering time compared to the intrinsic free carriers and experience a less negative *c* parameter (-0.67 vs -0.94 for the un-annealed $Mo_2Ti_2C_3T_z$ film, and -0.75 vs -0.86 for $Mo_2TiC_2T_z$ film), demonstrating the higher long-range, inter-nanosheet mobility compared to the intrinsic free carriers.

Over the time scales given by the photoconductivity, those excess carriers become trapped by the available defect states, recombine and eventually relax back to the ground state. Looking more closely at the $Mo_2Ti_2C_3T_z$ film, the magnitude of the photoinduced conductivity at 5 ps in the DC limit after photoexcitation with a 256 $\mu J/cm^2$ pulse is nearly one third of the magnitude of the intrinsic conductivity and changes little up to 50 ps after photoexcitation. At the same time, the excess carrier density, estimated from the Drude-Smith fitting, is only ~1% of the intrinsic carrier density (~ 10^{18} cm^{-3}). This observation emphasizes that optically injected carriers have higher short-range, intra-nanosheet, as well as long-range, inter-nanosheet, mobility and contribute significantly more to conductivity. Annealing causes subtle changes in the spectral shape. Fitting the data to the Drude-Smith model, we find that annealing result in a small but detectable increase in the *c*-parameter experienced by the photoexcited carriers from 0.67±0.02 to -0.62±0.02. This implies that, like for the intrinsic carriers, annealing enhances intra-nanosheet transport for photoexcited carriers. This results presumably from the reduced intra-nanosheet spacing as confirmed by XRD diffraction. The scattering time

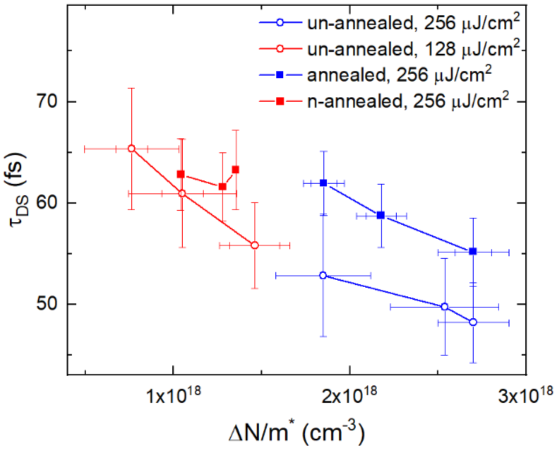

Figure 3-11 Scattering time τ_{DS} as a function of photoexcited carrier density in $Mo_2Ti_2C_3T_z$ scaled by the effective mass, extracted by fitting the complex photoconductivity spectra at different times after excitation and different excitation fluence values for un-annealed (open symbols) and annealed (solid symbols) samples. Reprinted with permission from [3], Copyright (2020) American Chemical Society

(and therefore the average photoexcited carrier mobility) varies between ~ 75 fs to ~ 50 fs with time and excitation.

Figure 3-11 plots the scattering time, τ_{DS}, as a function of photoexcited carrier density scaled by the effective mass that has been extracted from the Drude-Smith fitting of data at different times and excitation fluence values. We find that the scattering is shortest at high carrier densities when carrier-carrier scattering plays an important role.[95, 124] Annealing increases carrier scattering time in $Mo_2Ti_2C_3T_z$. We hypothesize that the increase in carrier scattering time (and intra-nanosheet, short-range carrier mobility) results from removal of intercalated species present on surfaces of the nanosheets, which affect the motion of carries in the conductive core regions of the nanosheets by causing potential fluctuations. The combined effect of improved intra-nanosheet and inter-nanosheet carrier mobility, represented by the changes in both scattering time τ_{DS} and c-parameter, explains improved carrier transport in annealed $Mo_2Ti_2C_3T_z$. These observed, annealing-induced, changes in mobility of free carriers and their ability to move between neighboring nanosheets may help explain changes in dynamics. If the intermediate time-scale photoconductivity decay components, ~ 10 ps and ~ 85 ps (~ 4 ps and 76 ps after annealing), represent trapping of mobile carriers by defects near nanosheet edges, then the higher mobility and improved inter-nanosheet transport accelerates this process. Carrier trapping and recombination at point defects *within* the individual nanosheets is likely responsible for the slowest, >200 ps, decay component and it is slowed after annealing, suggesting that mild annealing may 'heal' some of the point defects or lessen their effect by removing water and other intercalants from their vicinity if those species are co-located with the point defects that facilitate carrier trapping.

The photoinduced conductivity in the $Mo_2TiC_2T_z$ films is an order of magnitude smaller than in the $Mo_2Ti_2C_3T_z$ films, even at early times as presumably most photoexcited carriers recombine or become localized over very short time scales. For a small fraction of photoexcited delocalized carriers that remain after the initial fast decay, the photoconductivity spectra share many similarities with $Mo_2Ti_2C_3T_z$. Again, carrier scattering time (and therefore the intra-nanosheet mobility) is higher than that for the intrinsic free carriers (60 ± 5 fs vs 36 ± 4 fs). This scattering time is unchanged for different times after excitation and excitation fluence values, as the low photoinjected carrier density does not allow for a significant carrier-carrier scattering contribution. Moreover, unlike the $Mo_2Ti_2C_3T_z$ film, annealing does not significantly impact the carrier scattering time in $Mo_2TiC_2T_z$. It does, however, improve inter-nanosheet transport, as evidenced by changes in c-parameter from -0.75 ± 0.02 to -0.69 ± 0.02 after annealing. Again, this c-parameter is less negative than the one characterizing the intrinsic, not photoexcited, carriers, suggesting that photoexcitation generated a new population of delocalized carriers that travel easier between nanosheets. Annealing is also found to have a much more dramatic effect on the lifetime of photoexcited carriers in $Mo_2TiC_2T_z$ than $Mo_2Ti_2C_3T_z$, which may imply a larger density of defects both at the nanosheet edges and point defects within the nanosheets. Presumed edge trapping time reduces considerably in the annealed film, from ~ 50 ps to ~ 9 ps, as inter-nanosheet hopping is enhanced, evidenced by the change in c-parameter. The longer time scale component is also dramatically slowed, as can be best seen in Figure 3-8(c), suggesting that $Mo_2TiC_2T_z$ nanosheets are more susceptible to the deleterious effects of point defects and intercalated species on the lifetime of photoinduced carriers.

3.5 Summary and Conclusions

The overall picture of the microscopic carrier mobility and carrier dynamics in Mo-containing MXenes emerges from these results and earlier temperature-dependent transport measurements[35]. Intrinsically metallic, individual 2D $Mo_2Ti_2C_3T_z$ and $Mo_2TiC_2T_z$ nanosheets have high intrinsic carrier density (on the order of 10^{20} cm^{-3}). These intrinsic free carriers, as well as excess carriers injected by intra-band optical excitations, experience band-like, delocalized transport within individual nanosheets. However, the inter-nanosheet boundaries strongly suppress long-range inter-nanosheet transport in the films, as the long-range, inter-nanosheet mobility of intrinsic carriers is nearly an order of magnitude lower than short-range, intra-nanosheet mobility.

We demonstrated that optical excitation with 1.55 eV photons increases conductivity of both $Mo_2Ti_2C_3T_z$ and $Mo_2TiC_2T_z$ films, in stark contrast to $Ti_3C_2T_z$

where optical excitation suppresses conductivity, as discussed in Chapter 2. Both short-range (intra-nanosheet) and long-range (inter-nanosheet) mobility is higher for the carriers injected by the inter-band optical excitation compared to the intrinsic carriers, possibly because they reside in higher energy states with different average band curvatures. A fraction of photoexcited carriers survive for substantially longer periods, well over 200 ps, and possibly even longer.

Annealing further improves short- and long-range carrier transport of photoexcited carriers in both studied films. We hypothesize that trapping at point defects within the nanosheets and at the nanosheets edges and interfaces rapidly reduces the photoexcited carrier density within the first tens of ps, and these processes are even faster after annealing when inter-nanosheet transport is improved. More work is needed to fully understand the interactions between electronic transport and defects in MXenes. However, our finding of high photoinduced conductivity, optical absorption across the visible and near-infrared range, and long lifetime of photoexcited carriers makes Mo-based MXenes attractive for a whole host of optoelectronic, sensing and photoelectrochemical applications.

Acknowledgments

Mo-based MXene films for this work were provided by V. Natu and M. Barsoum at Drexel University. MXene fabrication and characterization at Drexel University was funded by NSF (DMR 1740795). We thank Dr. T. Ouisse for insightful discussions, M. M. Shalmani for assistance with annealing of samples, Dr. B. Giri for assistance with and SEM imaging, and Dr. T. Shi for assistance with THz measurements.

4 Applications of MXenes in THz devices

High electrical conductivity and strong absorption of electromagnetic radiation in the THz frequency range by metallic 2D MXene $Ti_3C_2T_z$ make it a promising material for electromagnetic interference shielding, THz detectors and transparent conducting electrodes. In Chapter 2, we discovered that ultrafast 400 nm and 800 nm optical pulses induce transient broadband THz transparency that persists for nanoseconds. We also demonstrated that this optically-induced transient THz transparency is independent of temperature from 95 K to 290 K. Here, we discuss possible applications of 2D $Ti_3C_2T_z$ MXene is THz photonic devices: an optically switchable electromagnetic interference shielding material and a THz polarizer.

4.1 Optical controllable EMI shielding

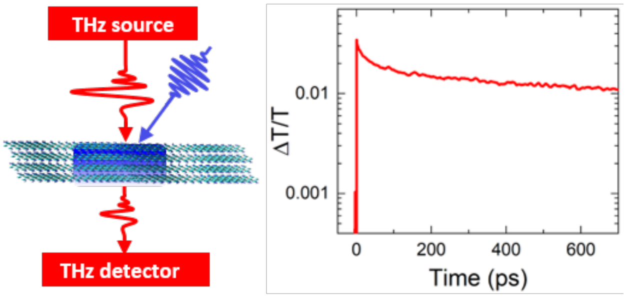

Figure 4-1 Schematic graph of optically controlable EMI shielding mechanism (left), THz transmissiom through $Ti_3C_2T_z$ MXene film is enhanced by ultrafast optical pump, this enhancement last more than 800 ps (right). Reprinted with permission from [4], Copyright (2019) American Chemical Society

Highly conductive and flexible, $Ti_3C_2T_z$ MXene has been recently suggested as a promising material for EMI shielding in the 8-18 GHz frequency microwave range, with EMI shielding efficiency (SE) of >50 decibels (dB) for a 2.5-micrometer film which is superior to graphene, graphite, copper and aluminum foils with lighter weight.[23, 25] An increasing demand for higher bandwidth and rates of data transfer will in the near future shift communications to the higher frequency range, necessitating extending EMI shielding into the newly designated 6G band (up to 3 THz).[125-128]

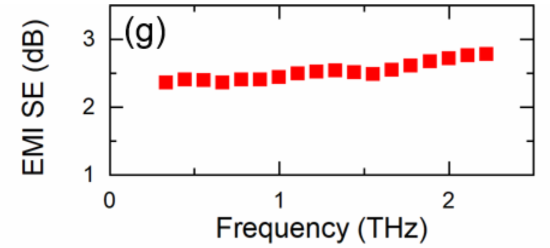

Figure 4-2. EMI SE calculated from data in Figure 1-9 (b). Adapted with permission from [4], Copyright (2019) American Chemical Society

Here, we focus on EMI shielding properties of $Ti_3C_2T_z$ in the THz frequency range.[27] From THz TDS measurements on a 25 nm-thick $Ti_3C_2T_z$ film discussed in Chapter 2, we calculate the absorption coefficient of the film to be ~2.2 x 10^5 cm^{-1} in the THz range (Figure 4-3), only ~ factor of 2 lower than theoretically predicted by Jhon et al in [24]. We find that high free carrier density and conductivity result in the high EMI shielding efficiency(SE), defined as $-20\log\left(\frac{E_{transmitted}}{E_{incident}}\right)$, as shown in Figure 4-2. At ~ 2.5 dB for a 25 nm film, it is comparable to the SE reported for carbon nanotube films and composites, multilayer graphene, as well as to the high THz EMI SE that has been reported recently for metallic MXenes.[21, 129, 130] The relatively low density of $Ti_3C_2T_z$ (ca. 2.39 g cm^{-3})[25] makes it particularly attractive for EMI SE applications, as high SE can be achieved without adding much extra weight to devices that are being shielded. We calculate specific SE (SSE) per unit thickness, defined as SE divided by density and thickness, to be ~ 4 x 10^5 dB cm^2 g^{-1}(Figure 4-3). Although not many reports exist on EMI SE characteristics of materials in the THz range, this number is 1-2 orders of magnitude higher than for metals (Al, Cu) in the GHz range.[25]

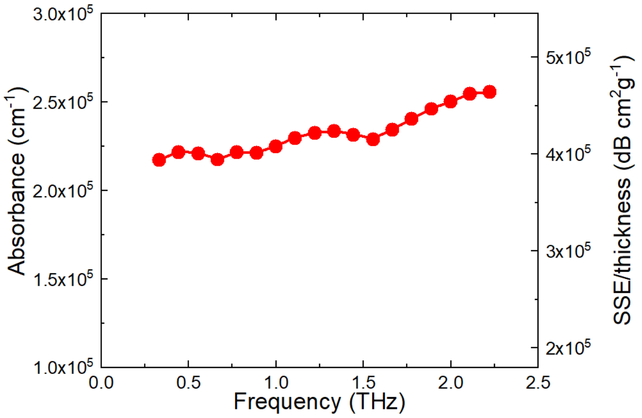

Figure 4-3 THz absorbance (left) and corresponding specific EMI shielding per unit thickness, defined as SE divided by density and thickness (right) for a $Ti_3C_2T_z$ film. Reprinted with permission from [4], Copyright (2019) American Chemical Society

In Chapter 2, we have discussed that both 800 nm and 400 nm light pulses induce long-lived enhanced transmission of the THz pulses, suggesting that optical pulses can be used to manupulate EMI SE in the THz range. As shown in Figure 4-4, the frequency-resolved transient change in EMI SE at different times after excitation with 800 nm pulse reveals that EMI SE is suppressed over the entire bandwidth of the THz probe (0. 25 – 2.25 THz), with the magnitude of the effect exhibiting a slow monotonical increase with frequency. This EMI SE suppression is a direct result of the photoinduced transient decrease in the real conductivity component σ_1 over the entire experimental frequency range (Figure 2-5), as power absorption of electromagnetic radiation is directly proportional to the real part of the conductivity in the corresponding frequency range.[131]

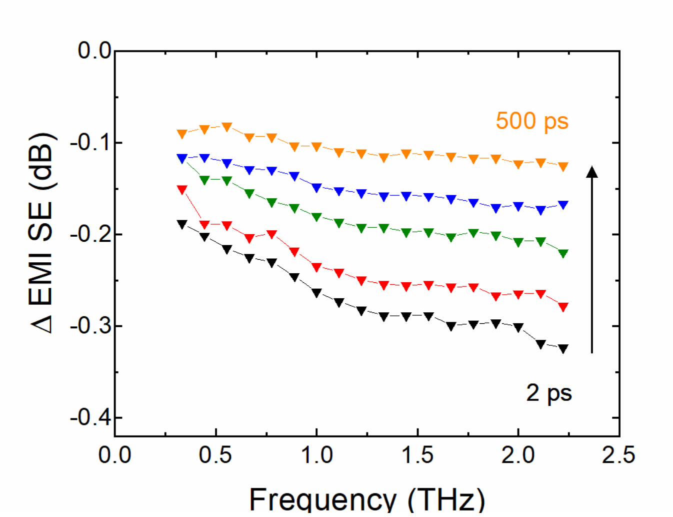

Figure 4-4 Photoinduced change in EMI SE at different times following excitation with 800 nm, 950 μJ/cm²pulse. Reprinted with permission from [4], Copyright (2019) American Chemical Society

We find that the real component of intrinsic THz conductivity, as well as the dynamics of the transient THz transmission enhancement recovery, are temperature-independent over a broad temperature range (95 K - 295 K). This temperature stability, combined with easy processibility, high mechanical performance with small mass makes it a good candidate for optically switchable THz shielding material. Possible applications include tunable EMI shielding, where on-demand communications in the THz range is enabled by optical gating, as illustrated in Figure 4-1, as well as sensitive, gated THz detection. In the future, with capability of control the composition of the surface terminations[132] and DFT simulations we will understand the mechanism better in order to engineer to achieve a higher modulate depth.

4.2 THz Polarizers Based on 2D $Ti_3C_2T_z$ MXene

Over the past two decades, rapid improvement in tabletop sources of terahertz, THz, radiation have inspired growth in THz technology applications for materials characterization, pharmaceuticals, imaging, communications and sensing among others.[93, 125, 126, 133, 134] In addition to reliable sources and detectors, these applications require other active/passive THz optical components, such as linear polarizers for which high extinction ratios, ERs, and low insertion losses (IL).[135] Currently, commercially available THz polarizers are either free-standing or supported metallic wire grids. Free-standing polarizers have high, ~ 20-40 dB power ERs and low insertion losses, but are expensive and fragile.[135] Substrate-supported metal, typically Al, wire grid polarizers are more robust and can be produced by photolithography,[136, 137] hot embossing,[138] etching[139] or nanoimprinting.[140] Some of these have recently been successfully demonstrated on flexible substrates, an important step towards conformable THz devices.[141] Inherent anisotropic conductivity of 1D nanostructures such as semiconducting or metallic nanowires, or carbon nanotubes, inspired THz polarizers based on highly aligned nanowire or nanotube arrays.[142-146] These structures achieve high performance characteristics, and, in the case of semiconductor nanowires, are dynamically switchable.[146] However, achieving high degrees of alignment of nanowires or nanotubes over macroscopic regions remains challenging. Here, we propose broadband THz polarizers based on a hydrophilic 2D MXene with metallic conductivity, MXene patterning had previously been carried out using laser printers,[147] or microcontact printing techniques,[148] with large feature sizes. MXene photodetectors that outperform more standard gold-based ones have been fabricated by spin-coating transparent $Ti_3C_2T_z$.[149] Here, we use a similar approach to fabricate a THz photonic structure.

In a proof of principle, we experimentally demonstrate that very thin (~ 30 nm), 10-20 μm wide striations of spin coated $Ti_3C_2T_z$, consisting of overlapping nanosheets that are 1-3 μm in laterial dimensions, exhibit excellent polarization properties over the 0.3 – 2.0 THz spectral range, with electric field ERs of up to 3 dB, corresponding to power ERs of 6 dB. Using Comsol Multiphysics simulations, we further show that increasing the line thicknesses to 1.5–2 μm, and optimizing the periods and fill factors of the periodic strications can increase ER to >16 dB for electric field or > 32 dB for power, while maintaing low insertion losses.

4.2.1 Synthesis of $Ti_3C_2T_z$ Colloidal Suspension and Pattern Production using Photolithography

The $Ti_3C_2T_z$ MXene polarizer devices were fabricated at Drexel University by Kiana Montazeri in Bahram Nabet group. 2 by 2 mm^2 comprised of parallel line patterns were deposited on quartz substrates using conventional photolithography and a simple fabrication process, illustrated schematically in Figure 4-5.

First, the Ti_3AlC_2 MAX phase (Figure 4-5 (a)) was etched and delaminated to obtain a colloidal aqueous suspension of $Ti_3C_2T_z$ single flakes (Figure 4-5 (b)). Several patterns of striations with various width (w = 10 μm and 20 μm), separated by spaces, s = 10 μm, 30 μm and 40 μm were formed using photoresist and conventional contact lithography on quartz substrates (Figure 4-5 (c)) and developed (Figure 4-5 (d)).

In brief, the MXene colloidal suspension, prepared using the same procedure as used for the film discussed in Chapter 2, was then spin cast on the substrate, where a polarizer pattern was photolithographically defined using positive photolithography with 2 μm thick S1813 photoresist Figure 4-5(e). Once deposited, the film temperature was raised to 115° C for 150 s using a hot-plate. Microposit UV exposure at 170 J/cm^2 for 5 s using a contact mask aligner was performed. Chemical development was carried out using Microposit MF CD-26 developer for 60 s, rinsed and dried. Films of $Ti_3C_2T_z$ were spin-cast on all substrates at 800 rpm for 30 s using a colloidal suspension of single flakes (≈ 23 g/L). The photoresist was removed by immersion of the sample

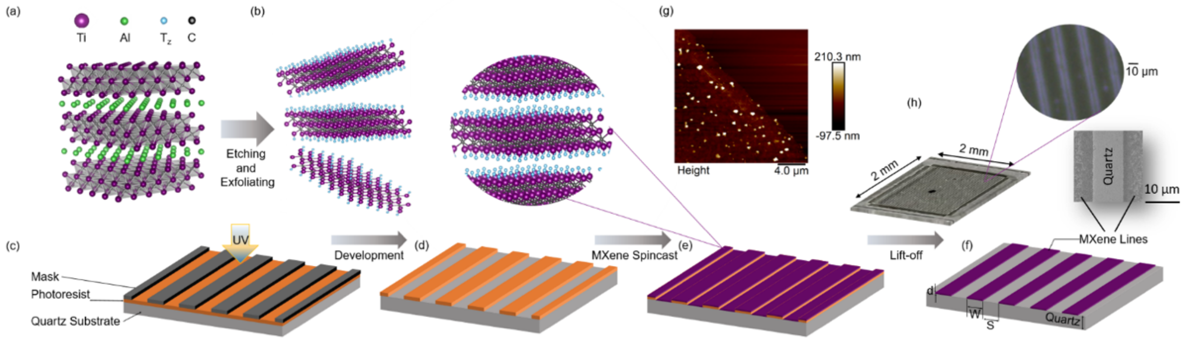
(a)
Ti
Al
T$_z$
C
(b)
Etching and Exfoliating
(g)
210.3 nm
-97.5 nm
Height
4.0 µm
(h)
10 µm
2 mm
2 mm
Quartz
10 µm
(c)
UV
Mask
Photoresist
Quartz Substrate
Development
(d)
MXene Spincast
(e)
Lift-off
(f)
MXene Lines
d
W
S
Quartz

Figure 4-5 Fabrication process of MXene wire-grid polarizer. (a, b) Preparation of MXene colloidal suspension. In (c) and (d), conventional photolithography is performed resulting in exposed areas for striations. (e) MXene aqueous colloidal suspension is spin-coated, and (f) lifted off by immersion in acetone. (g) AFM of a striation edge. (h) optical image of the final device and SEM close-up of striations. Copyright 2020 The Authors of [2]. Published by Wiley-VCH GmbH

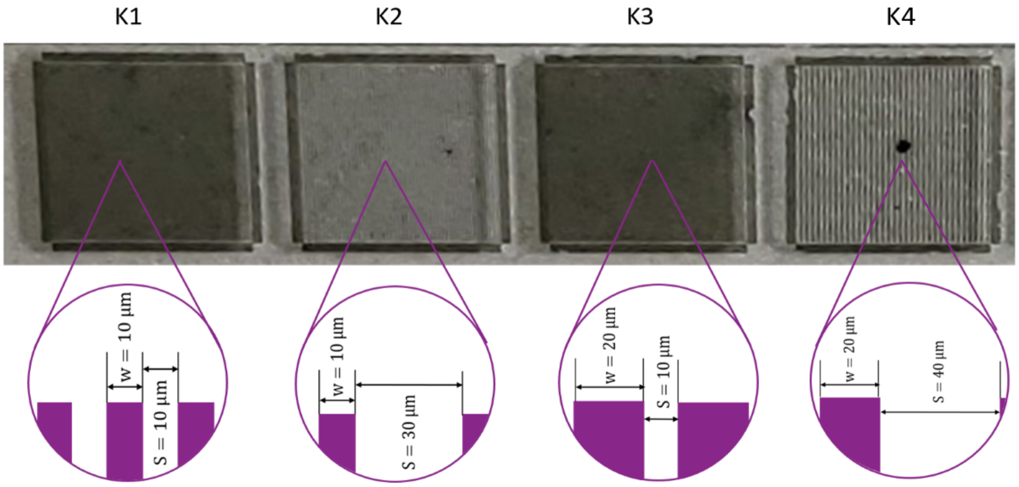
K1
K2
K3
K4
w = 10 µm
S = 10 µm
w = 10 µm
S = 30 µm
w = 20 µm
S = 10 µm
w = 20 µm
S = 40 µm

Figure 4-6 Optical Images of four polarizer patterns tested herein. Copyright 2020 The Authors of [2]. Published by Wiley-VCH GmbH

in acetone for 30 s, and sonicated in an ice bath for 10 s, then dried, resulting in the printed MXene structures. The thicknesses of the resulting lines were measured by AFM using a tapping of the probe at ambient conditions and was found to be ~ 30 nm Figure 4-5(g). The sharpness of the edges, seen in AFM and

SEM Figure 4-5(h) images indicate that the resolution of this method is primarily limited by lithography. This procedure is performed at room temperature, does not require high vacuum, high temperature deposition chambers, nor plasma (dry) etching capabilities. It is also compatible with common microfabrication techniques including photonic integrated circuits and silicon photonics. Four different patterns were created, as shown in Figure 4-6: K1 (w = 10 µm, s = 10 µm), K2 (w = 10 µm, s = 30 µm), K3 (w =20 µm, s = 10 µm), and K4 (w = 20 µm, s = 40 µm).

4.2.2 Performance test: Extinction ratio and insertion loss

We evaluated the performance of the polarizers using a conventional THz TDS setup (Figure 1-8). The wire-grid polarizer (Microtech Instruments; field extinction ratio of 0.01) ensured that only the component of the transmitted

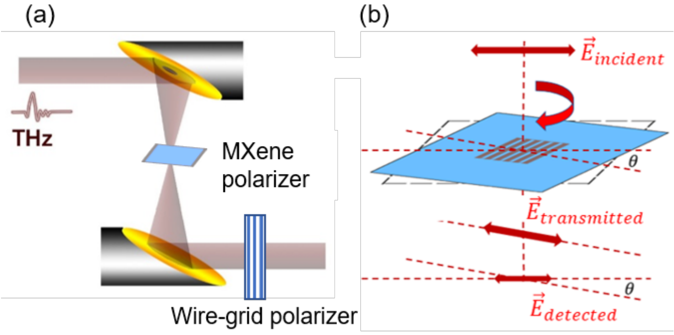

Figure 4-7 (a) Schematic diagram of experiment: Incident THz pulse is focused to a ~ 1.5 mm spot on the polarizer using an off-axis polarizer; another polarizer collects the transmitted pulse, which goes through a commercial wire-grid polarizer before being detected. (b) A linearly polarized THz pulse is normally incident on a MXene polarizer, which can be rotated around the normal; only a component that is parallel to the incident pulse polarization is detected. Copyright 2020 The Authors of [2]. Published by Wiley-VCH GmbH pulse that was parallel to the incident pulse polarization was detected. The orientations of the samples were varied by rotating the samples by an angle θ Figure 4-7(b).

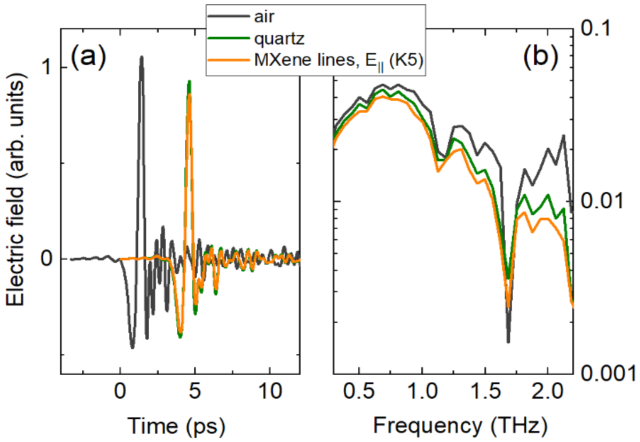

Figure 4-8 (a) Reference THz waveform (transmitted through air), and THz waveforms transmitted through quartz substrate and through one of the polarizer devices (K4) with lines oriented along incident THz polarization. (b) Corresponding THz amplitude as a function of frequency. Dips in frequency are due to absorption by water vapor. Copyright 2020 The Authors of [2]. Published by Wiley-VCH GmbH

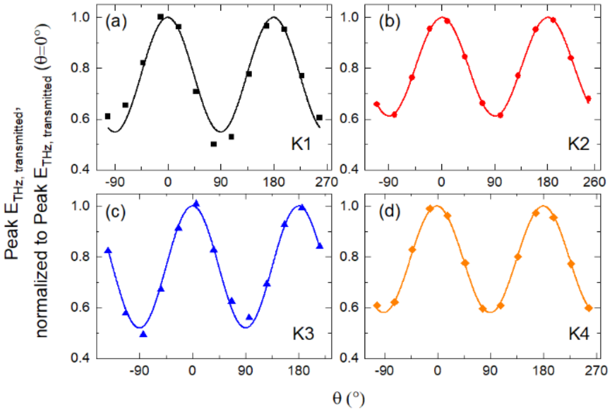

Figure 4-9 Peak of transmitted THz pulses, normalized to its value for $\theta = 0°$, as a function of θ, for polarizer structures (a) K1, (b) K2 (c) K3 and (d) K4. Symbols show experimental data, and lines – Malus's law fits. Copyright 2020 The Authors of [2]. Published by Wiley-VCH GmbH

An example reference THz pulse that propagated through air without the sample in its path, along with the pulses transmitted through the quartz substrate and through one of the polarizer structures with lines oriented along the polarization of the THz probe pulse is shown in Figure 4-7(a). The corresponding THz amplitude is shown in Figure 4-8(b). The ~ 1 mm thick quartz substrate with a refractive index of 2.156 at 1 THz[150] introduces a significant delay in the arrival of the probe pulse, and attenuates the transmitted pulse due to reflection losses. The insertion loss due to a quartz substrate, defined as $IL_{quartz} = -10\log(E_{quartz}/E_{ref})$, is ~ 0.6 dB at 1 THz, as shown later in Figure 4-10. For future applications, THz-transparent flexible substrates with lower refractive indices will be used to minimize insertion losses. In the following analysis, we focus on

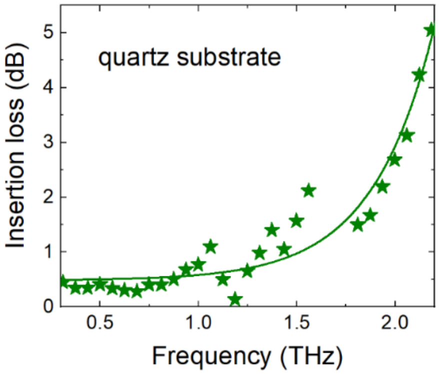

Figure 4-10 Insertion loss of a quartz substrate. Symbols – experimental points calculated from data in Fig. 2(b), line – guide to the eye. At 1 THz, the insertion loss is ~ 0.6 dB, in agreement with predicted value due to air-quartz reflection, given n_{quartz}=2.156. At frequencies > 1.8 THz, impurity absorption and higher-lying phonon modes contribute to the measured insertion loss. Copyright 2020 The Authors of [2]. Published by Wiley-VCH GmbH

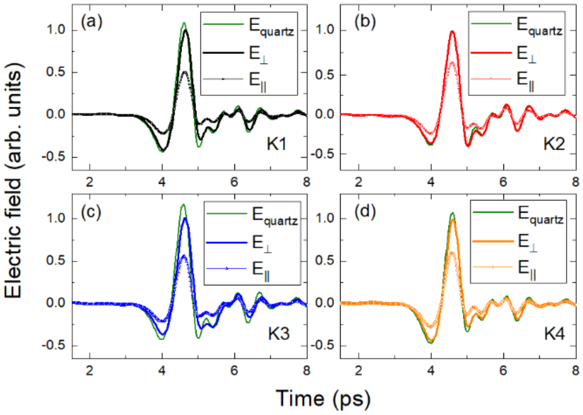

Figure 4-11 Transmitted THz pulses in time domain for incident THz pulse polarization parallel and perpendicular to the lines, for polarizer structures K1 (a), K2 (b), K3 (c), and K4 (d). Reference THz pulses transmitted through the quartz substrate are also shown. Copyright 2020 The Authors of [2]. Published by Wiley-VCH GmbH

the insertion loss introduced by the MXene structures alone, treating the THz pulses transmitted through the quartz substrate as a reference. Dips in the THz amplitudes at ~ 1.15 THz and ~ 1.7 THz are due to strong absorption of THz radiation by water vapor in ambient air which results in a reduction of the signal to noise ratio in the vicinity of those frequencies.

Rotation of the polarizer structure about the normal through an angle θ results in a characteristic Malus's law $cos^2(\theta)$ dependence, as shown in Figure 4-9 which plots the peak of the transmitted pulse as a function of θ for four different polarizer structures. The resulting peak degrees of polarization, defined as $(E_{\perp} - E_{||})/(E_{\perp} + E_{||})$, range from ~ 30 % for K1 and K3, down to 27 % for K4 and 24 % for K2. The entire time domain waveforms for the electric field of the incident THz pulse parallel and perpendicular to the polarizer lines, for all four structures, are shown in Figure 4-11where the reference THz pulses transmitted through the quartz substrate are also shown. The frequency-resolved THz amplitudes of the waveforms in Figure 4-11 are then used to

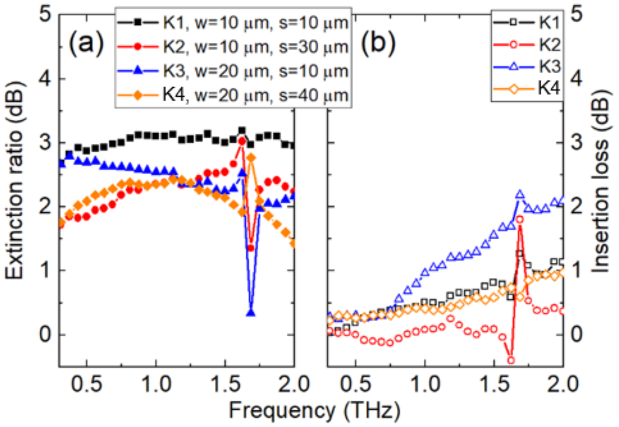

Figure 4-12(a) Electric field extinction ratios, and (b) insertion losses for four THz polarizer devices. Copyright 2020 The Authors of [2]. Published by Wiley-VCH GmbH

calculate the electric field ERs ($ER = 10\log(E_{\perp}/E_{||})$) and insertion losses $IL = -10\log(E_{\perp}/E_{quartz})$, which are plotted in Figure 4-12 as a function of frequency. While the demonstrated ER values are significantly lower than those for commercially available structures (10-20 dB for electric field, or 20-40 dB for power), we stress here that the thickness of the MXene lines in the polarizers studied here is only ~ 30 nm, compared to ~ 20-40 μm thick metal wires that are typically used in commertial wire-grids. In fact, for the best performing structure (K1), ER is only ~ factor of 2 lower that that demonstrated for single layer, 2 μm thick carbon nanotube polarizers.[142, 143] Comparing the performance of the four structures, we observe that the narrower lines (10 μm vs. 20 μm), and narrow gaps (10 μm) yield the best compromise between ER and IL. The wider lines with the same gap (K3), result in a higher area filling fraction (2/3 vs 1/2), IL increases without gain in ER. For the lower filling fractions, ER is reduced.

4.2.3 FDTD Simulation of $Ti_3C_2T_z$ MXene based THz polarizers on Comsol

Finite-difference time-domain (FDTD) simulations of our $Ti_3C_2T_z$ polarizer performance at 1 THz as a function of period (w+s), fill factor (w/(w+s)), and line thicknesses were carried out using the RF module of the commercial solver Comsol Multiphysics. As discussed in Chapter 2, the properties of $Ti_3C_2T_z$ in the THz range can be parameterized using a Drude-Smith model,[75, 78] following previous reports.[4, 27, 151] Depending on the preparation and morphology, the carrier densities in $Ti_3C_2T_z$ films can reach ~ $2x10^{21}$ cm^{-3}, scattering times are on the order of tens of fs, and the c-parameter ranges from -0.97 in films, with < 1 μm flakes separated by gaps to -0.69 in continuous films of overlapping flakes.[4, 27] Here, we have established the model parameters by fitting the THz conductivity conductivty in the K3 polarizer with the highest area coverage, using THz probe pulses that are parallel to the $Ti_3C_2T_z$ lines in order to probe the motion of carriers within the lines. The complex conductivity is shown in Figure 4-13. The fitting parameters are given on the figure, and are consistent with previous reports. Carrier density was determined using a zone-center electron effective mass of 0.2845 m_e.[28] To model the polarizers, we assumed a carrier density of 4×10^{20} cm^{-3}, a scattering time of 40 fs, and a Drude-Smith c-parameter of - 0.75, representing the effect of $Ti_3C_2T_z$ nanoflake boundaries and disorder on the long-range electron transport. Our simulation also accounts for the THz absorption by quartz substrate (Figure 4-10).

The FDTD simulations were performed using Comsol Multiphysics assuming periodic boundary conditions and perfectly matched layers (PML). Response of $Ti_3C_2T_z$ to the incident plane monochromatic electromagnetic waves was modeled within the framework of the Drude-Smith conductivity model, as discussed earlier. Response of the quartz substrate was modelled assuming the average refractive index is 2.156 in the 0.5–1.5 THz range,[150] and a negligible absorption coefficient. Neglecting substrate absorption allowed us to set the thickness of the quartz layer in the simulations to 10 μm to avoid Fabri-Perot interference effects when simulating the response of the polarizer structure to plane monochromatic

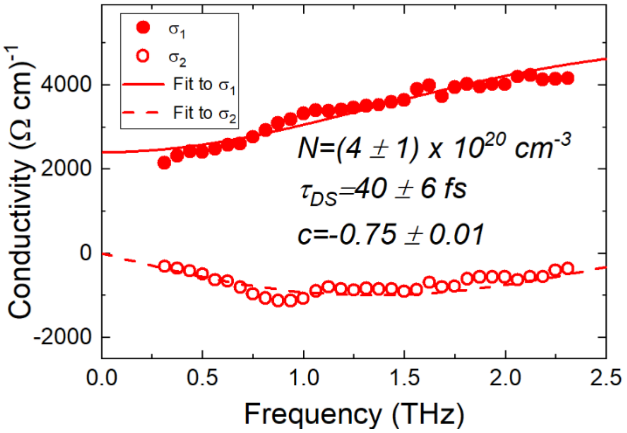

Figure 4-13 Complex THz conductivity (solid symbols represent real and open symbols – imaginary conductivity components; lines show a global fit of both components to the Drude-Smith model with fit parameters given in the legend. Copyright 2020 The Authors of [2]. Published by Wiley-VCH GmbH

waves. Response of real structures was measured using short THz pulses, and Fabri-Perot effects play no role as pulses reflected multiple times at quartz interfaces were well separated in the time domain. Since the thickness for the MXene layer is small comparing with the lateral line width and gap between the lines, transition boundary conditions were assumed to decrease the calculation times. The linearly polarized THz waves - with fixed frequencies in the THz range - were incident via PML1, and exit through PML2, respectively. Figure 4-14 (b,c) shows an example of the instantaneous electric field distribution in x-y and x-z planes for the incident wave that is polarized at 45° with respect to the MXene lines. In Figure 4-14 (b), a significant reduction in electric field is seen behind the wires (blue areas) due predominantly to the THz absorption and reflection by

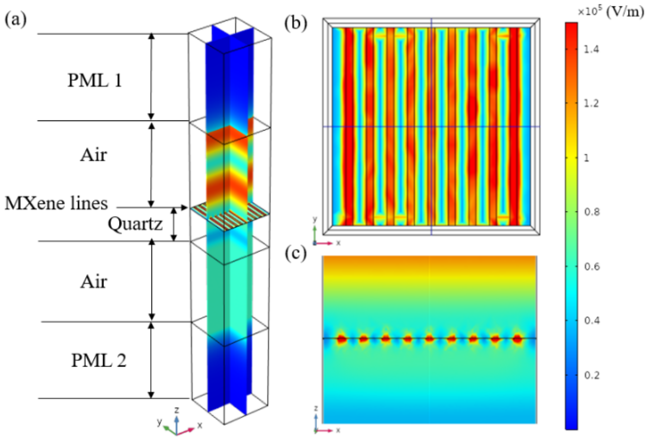

Figure 4-14 (a) FDTD simulation geometry of MXene polarizer. PML is perfect matched layer. PML 1 acts as a THz wave input, and PML 2 as THz wave output. (b), (c) Electrical field distribution in x-y plane (b) and x-z plane (c) when the polarization of the incident THz wave incident makes 45^O angle with the x-axis. Copyright 2020 The Authors of [2]. Published by Wiley-VCH GmbH the MXene lines. Enhancement of the electric field in the gaps between the lines is also seen.

For periods of 20 μm, filling fractions of 0.5 and line thicknesses of 30 nm - corresponding to the K1 polarizer geometry - our simulations yield ER of 2.6 dB

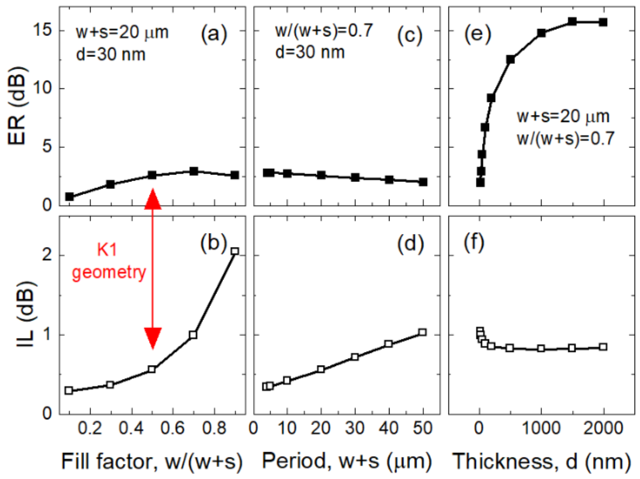

Figure 4-15. Simulated ER (a, c, e) and IL (b, d, f) at 1 THz as a function of fill factor (a, b), period (c,d) and thickness (e,f). Parameters that were fixed in a simulation are given in the top panels (a, d, e). Copyright 2020 The Authors of [2]. Published by Wiley-VC.

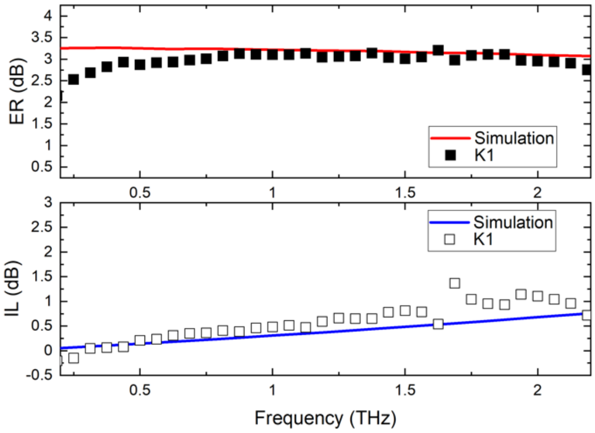

Figure 4-16 Frequency-resolved extinction ratios and insertion losses for THz polarizer K1. Symbols are experimental data, and the red and blue lines are the simulation results.

and IL of 0.6 dB (Figure 4-15), in good agreement with experimental results (Figure 4-12). We attribute the small deviations of the experimental results from the simulations to inhomogeneities in the fabricated devices.

As expected, we find that increasing the filling factor by increasing the line width w, while keeping the period constant, increases the insertion losses. The ER increases up to filling fraction of ~ 0.5-0.7 (Figure 4-15 (a). If the filling fraction is fixed at the near optimal value of 0.7, we find that narrower lines are more desirable, as they minimize ILs alongside a modest improvement in ERs. Finally, we find that increasing the line thickness dramatically improves polarizer performance, with electric field ER saturating at ~ 16 dB for a thickness of ~ 1 μm (Figure 4-15 (e)). The optimal MXene polarizer thickness agrees well with a

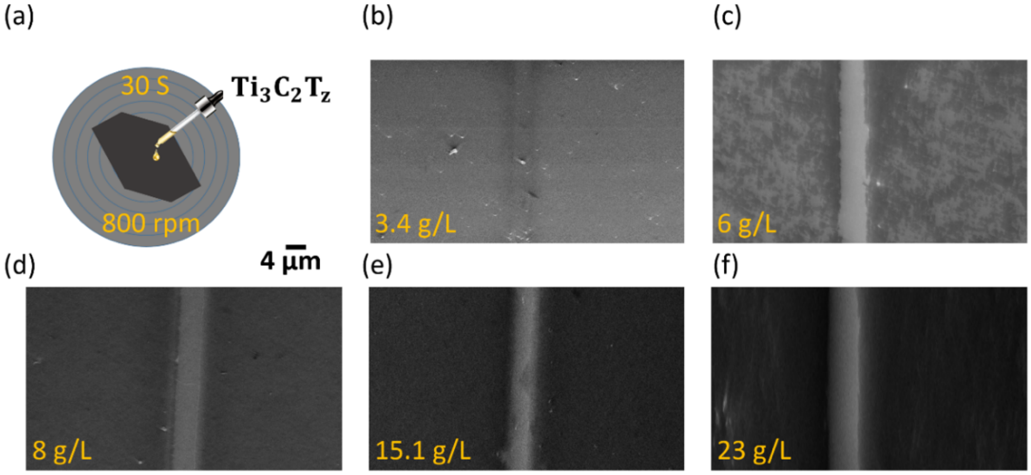

Figure 4-17. Spin-casting and lifting off of various concentration of solids in $Ti_3C_2T_z$, (a) Spin cast was performed in 30 seconds with 800 rpm rotation speed. SEM images of the resulting striations with spacing s=4μm spacing between the lines for (b) 3.4 g/L, (c) 6 g/L, (d) 8 g/L, (e) 15.1 g/L, and (f) 23 g/L concentration. Copyright 2020 The Authors of [2]. Published by Wiley-VCH GmbH

calculated $Ti_3C_2T_z$ skin depth at 1 THz, $\delta = \sqrt{2/(\omega\mu_0\sigma)} \approx 0.9\,\mu m$, where μ_0 is the vacuum permittivity, $\omega/2\pi$=1 THz, σ(1 THz) ~ 5000 (Ω cm)$^{-1}$ (Figure 4-13).

Work is ongoing to achieve thicker polarizer structures with high ER. To date, we have attempted to fabricate them by spin casting thicker films starting with various $Ti_3C_2T_z$ concentrations in the colloids, as higher solid concentrations, results in thicker films. However, the resulting films and patterns, were nonuniform and lower yields of the desired patterns on the quartz (Figure 4-6). Further study on the best methods of deposition for producing thick uniform films is needed. We are currently working on spray coating a low concentration suspension for longer times to achieve uniform, but tightly aligned MXene flakes which will offer better conductivity along with more thickness of the patterns of the wafer. Another technique for achieving thicker wires is to encapsulate the wires in PDMS and stack up multiple layers to get an effectively thicker wires in the polarizer.

4.2.4 Conclusion

We demonstrated a proof-of-concept THz polarizer based on parallel lines of overlapping $Ti_3C_2T_z$ nanosheets that are solution-processed and can be deposited on a variety of substrates. Lines only 30 nm thick yield electric field ERs of up to 3 dB, or power ERs of up to 6 dB. Simulations show that ERs can be increased up to > 16 dB for electric field, for power by increasing the line thickness to 1.5-2 μm, with line widths of 10 μm or less, and area filling fractions in the 0.5-0.7 range giving the optimal results. The projected performance is comparable to commercial polarizers at a fraction of the cost and thickness. We propose to increase the thickness of the optimized devices by stacking multiple layers of MXene lines on THz-transparent, flexible substrates such as PDMS or TPX, which can also serve to encapsulate the MXene structures to prevent their oxidation. Finally, as discussed in Chapter 2 and Chapter 4.1, ultrashort optical pulses can dynamically reduce the THz conductivity of $Ti_3C_2T_z$ MXene, raising the possibility of dynamically-tunable MXene polarizers for high-speed THz modulator devices.

Acknowledgements

MXene fabrication, deposition, and structural characterization of polarizers was carrierd out by K. Montazeri, M.B. Barsoum and B. Nabet at Drexel University and was supported by NSF DMR 1740795. Work at WPI was supported via Transformative Research and Innovation, Accelerating Discovery (TRIAD) seed grant. We also thank J. Bouchard for helpful discussions of Comsol simulations.

5 Future Work and Conclusions

5.1 Development of an intense THz source and Preliminary data: Nonlinear THz spectroscopy of MXenes

In addition to using THz pulses as a minimally perturbative probe of carrier dynamics in MXenes and other nanomaterials, it is now possible to generate THz pulses sufficiently intense to be used as a source of excitation[152]. Intense THz pulses have pulse energies on the order of μJ and can deliver peak electric fields that reach hundreds of kV/cm in a contact-free way when focused to a ~ mm size spot. Electric fields of such magnitudes can be used to coherently drive low-frequency lattice vibrations, switch ferroelectric domains, resonantly control spin polarization, drive intra-exciton transition and field ionization[153-155]. In 2D materials like graphene, nonlinear effects such as multiple harmonics generations have been observed at THz frequencies[156]. Metallic MXenes have high densities of free carriers which can be driven out of equilibrium by the intense THz fields, potentially leading to nonlinear THz effects. One of the promising future directions in THz spectroscopy of 2D MXenes is, therefore, nonlinear THz spectroscopy. With that goal in mind, this final Chapter discusses development and characterization of the intense THz pulse source.

Over the past decade, various methods of generating intense THz pulses have been developed such as quantum cascade lasers[54], photoconductive antennas[56], free-electron lasers, and synchrotrons. An approach to intense THz pulse generation that has been implemented in our laboratory is optical rectification in $LiNbO_3$ crystals. $LiNbO_3$ has a high nonlinear optical coefficient for optical rectification (d_{eff}=168 pm/V vs 69 pm/V for ZnTe). As discussed in Chapter 1, phase matching in $LiNbO_3$ can be achieved in a noncollinear geometry, using tilted pulse front excitation from an amplified Ti:Sapphire laser (Figure 1-7) [61, 157].

The first step in using intense THz pulses for nonlinear spectroscopy is characterization of the source by measuring the THz pulse energy, pulse duration and bandwidth, and peak THz electric field at the beam focus.

To measure the THz pulse energy, we have used Gentec QE8SP-B-MT-INT pyroelectric detector with black absorptive coating. The generated THz beam is collimated and focused onto the detector by a pair of off-axis parabolic mirrors. Black polyethylene filter is used to block residual 800 nm light. The beam is modulated at 25.2 Hz by an analog optical chopper, and lock-in detection is used to measure THz signal at the detector and distinguish it from thermal noise. The THz pulse energy of 1.3 μJ has been achieved, in agreement with the 800 nm to THz conversion efficacy of ~ 0.001 reported in other records from a tilted-pulse front $LiNbO_3$ source[158]. It should be noted here that accurate THz absorbance calibration of the black absorptive coating used in Gentec pyroelectric detector is not currently available and will have to be cross-checked in the future with other detectors.

We have also used two methods to calculate the peak THz electrical field at the focus of the beam: opto-electrical sampling in ZnTe and calculation using the pulse energy measured by the pyroelectric THz detector and the beam size measured using a thermal imager.

Using the first method, we can relate the ellipticity of the sampling beam induced by the THz electric field when the sampling beam traverses ZnTe detector crystal simultaneously with the THz pulse. Induced ellipticity angle is θ, and in the limit

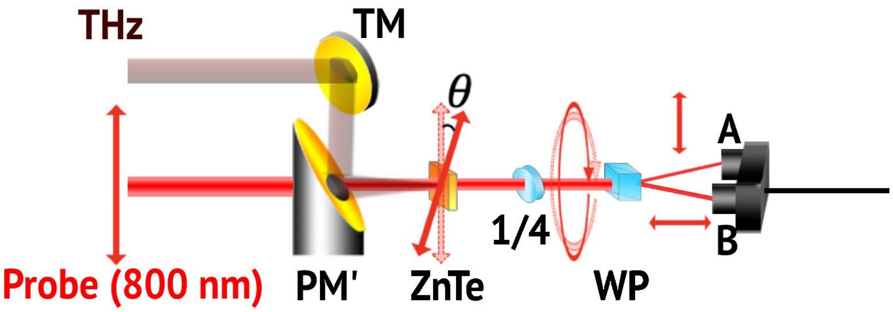

Figure 5-2 THz electrical field measured by opto-electrical sampling technique

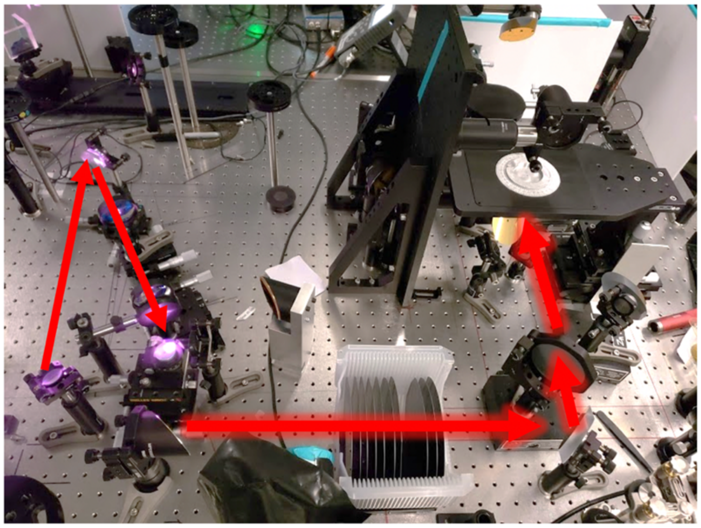

Figure 5-1 optical path of Intense THz attenuated by silicon wafers before detection of small modulation $\sin(\theta) \sim \theta$. To stay in the linear detection range, we attenuate the THz beam using multiple Si wafers before the ZnTe detection crystal. Then, THz electrical field E_{THz} can be calculated as[159]

$$E_{THz} = \sin^{-1}(\frac{A-B}{A+B}) * \lambda_0 \,/ (2\pi n_0^3 r_{41} t_{\mathrm{ZnTe}} t_{\mathrm{Si}}^N L), \qquad (\mathrm{Eq.}\,13)$$

where A = 32.0, B = 26.5 are the voltages measured by the balanced detectors when THz pulse and detection pulse peaks are overlapping, $\frac{A-B}{A+B} = \theta,\ \lambda_0 = 800\,nm$, $n_0 = 2.87$ is the refractive index of ZnTe, $r_{41} = 4.04$ pm V^{-1} is the electro-optical coefficient of ZnTe, $t_{ZnTe} = \frac{2}{n_{THz}+1}$ is Fresnel transmission coefficients of ZnTe crystal , t_{Si} = 0.7 is Fresnel transmission coefficient of one silicon wafer, L =0.5 mm is the thickness of the detection ZnTe crystal, N=8 is the number of high-

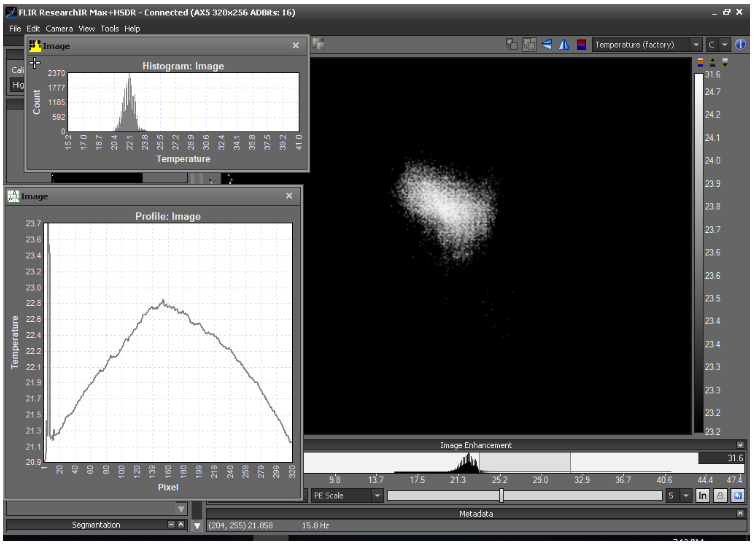
FLIR ResearchIR Max+HSDR - Connected (AX5 320x256 ADBits: 16)
File Edit Camera View Tools Help
Image
Histogram: Image
Count
2370
1777
1185
592
0
15.2 17.0 18.7 20.4 22.1 23.8 25.5 27.2 28.9 30.6 32.4 34.1 35.8 37.5 39.2 41.0
Temperature
Image
Profile: Image
Temperature
23.7 23.6 23.4 23.2 23.0 22.8 22.6 22.4 22.2 22.1 21.9 21.7 21.5 21.3 21.1 20.9
1 20 40 60 80 100 120 139 160 180 199 219 240 259 279 299 320
Pixel
Temperature (factory)
C
31.6 24.7 24.2 24.1 24.0 23.9 23.8 23.7 23.6 23.6 23.5 23.4 23.4 23.3 23.3 23.2 23.2
Image Enhancement
31.6
9.8 13.7 17.5 21.3 25.2 29.0 32.9 36.7 40.6 44.4 47.4
PE Scale
5
In
Metadata
Segmentation
(204, 255) 21.858
15.8 Hz

Figure 5-3 The profile of THz focus spot is captured by the Flir A35 thermographic camera with a 320 × 256 pixels (pixel pitch of 2.5 µm) sensor, the sensor dimension is 8.0 mm X 6.4 mm. The diameter of focused THz spot is estimated to be 1.5 mm.

resistivity silicon wafer used. Using this method, we obtain peak electric field of 90 KV/cm. We can also use thermal imaging camera (Flir A35) to estimate the electrical field of THz pulse E_{THz} at the focus by measuring the size of the THz spot (Figure 5-3) as

$$\left|E_{THz}^{peak}\right| = \sqrt{\frac{4Z_0W}{\tau_{FWHM}A}} \qquad \text{(Eq. 14)}$$

where Z_0 is the vacuum impendence, W is the THz pulse energy (1.3 μJ), THz pulse width τ_{FWHM} is ~ 1.4 ps, $A = \pi R^2$ is the area of focus spot. With this approach, the calculated peak THz electric field is 256 KV/cm.

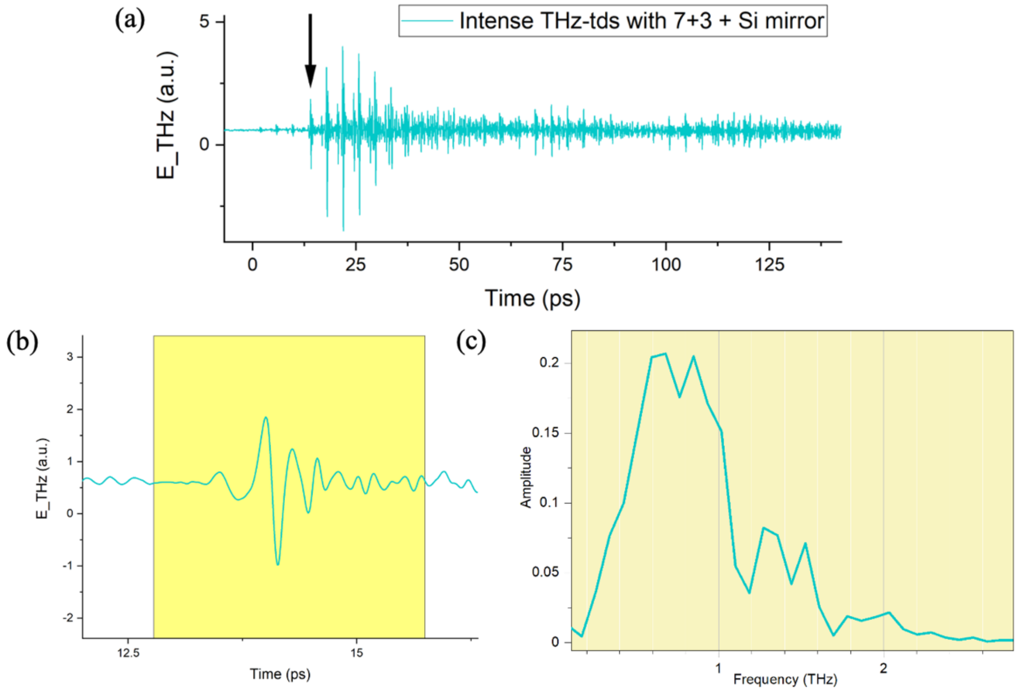

Figure 5-4 (a) The waveform of THz pulse attenuated by ten silicon wafers and one silicon mirror (45 degree). After the primary pulse, the later higher pulses are due to the interference between multireflection. (b) (c) are the first/primary THz pulse waveform in time domain and frequency domain by FFT.

Figure 5-4 (a) shows THz pulses in the time domain. Multiple pulses arise from reflections in Si wafers used as attenuators. To characterize the duration and bandwidth, we analyze the time-windowed first pulse in the sequence, indicated by an arrow in Figure 5-4 (a). The bandwidth of the pulse shown in Figure 5-4 (b) is 0.2 - 2.1 THz Figure 5-4 (c)), narrower than that of the ZnTe source. In the future, this source can be used to study nonlinear THz transmission of MXene films.

I have carried out a preliminary nonlinear THz spectroscopy measurement that have motivated the construction of the THz source on the $Ti_3C_2T_z$ sample at Max Plank Institute for Polymer Research in Mainz, Germany, in the laboratory of D. Turchinovich and in collaboration with H. Hafez. A small but discernable enhanced transmission at higher peak THz field is observed, suggesting that

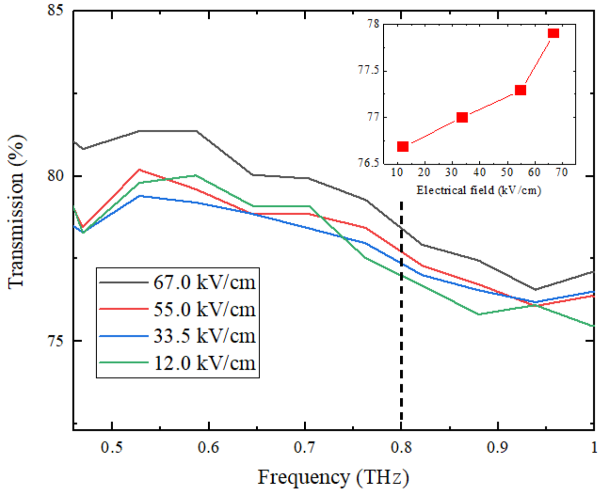

Figure 5-5 Intense THz transmission of $Ti_3C_2T_z$*, the insert shows the transmission at 0.8 THz depending on THz electrical field (Data taken by thesis author at MAX Plank Institute for Polymer Research, 2018)*

saturable absorption might occur at higher electric fields (Figure 5-5). Higher THz electrical field that can be achieved with the newly constructed source will allow investigations of $Ti_3C_2T_z$ and other 2D MXenes. Saturable absorption in the THz range makes MXenes promising for applications in THz modulators and other nonlinear devices.

Collinear THz pump THz probe (TPTP)

In order to study nonlinear properties of MXenes in the THz range, two experimental configurations are proposed and described below: THz pump-THz probe spectroscopy and z-scan measurements.

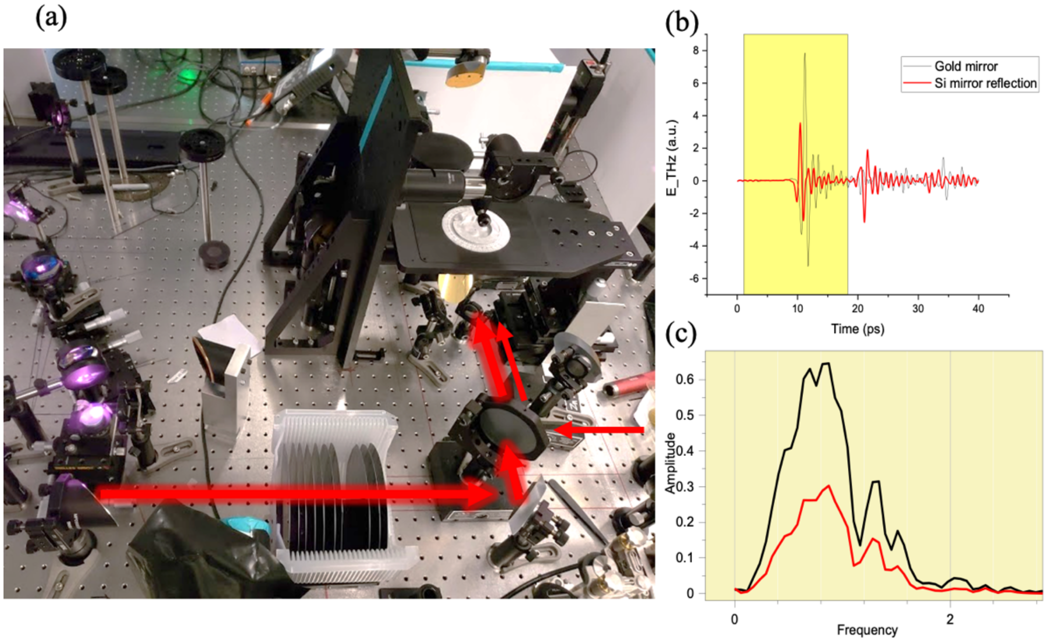

Figure 5-6 (a) Collinear THz pump THz probe setup, (b) (c) show the silicon mirror is optimized for reflecting THz probe pulse, where the reflection from it is about half of the reflection from original gold mirror

In THz pump-THz probe measurements, an intense THz pulse is used as an excitation, and a time-delayed second, weaker THz pulse is used as a probe. To overlap both pulses on the sample, we use an insulating silicon wafer as a THz beam splitter. The THz probe is reflected to parabolic mirror and focused on the sample, while the intense THz pulse is transmitted through the wafer is collinearly focused on the sample as well (see Figure 5-6).

Like in the case of OPTP, we can control the delay time of intense THz pump and THz probe and monitor the intense THz pulse induced carrier dynamics. The first few picoseconds the resulting signal is a convolution of the pump and the probe, but after the initial time window corresponding to the pump duration, the observed dynamics can be interpreted similarly to OPTP.

Intense THz Z-scan in MXenes

The open aperture Z-scan method has been applied to characterizing the nonlinear optical properties of materials. In this configuration, the sample is

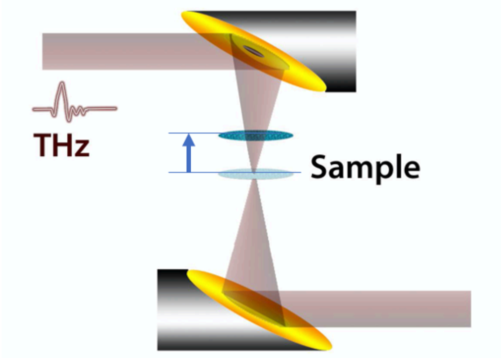

Figure 5-7 THz Z-scan schematic graph

moved through the focus of the THz beam (Figure 5-7). This way, the incident pulse energy is constant, but the sample can experience varying peak THz field as the size of the beam changes. The resulting curve is the total transmitted THz pulse energy through the measured sample as a function of sample position relative to the focus. The nonlinear optical absorption can result from intervalley scattering or multiphoton absorption[160, 161]. For example, this method has been used to study nonlinear absorption bleaching due to intervalley scattering in n-doped semiconductors and absorption enhancement due to impact ionization effects in an undoped InSb[162]. Applying it to MXene films will allow characterization of their nonlinear response at the THz frequencies.

5.2 Conclusions

This thesis reports on the first detailed investigation of optoelectronic properties of a new class of 2D materials, MXenes, in the THz range of electromagnetic spectrum. Specifically, selection of three specific MXene chemistries for which synthesis has been well established: $Ti_3C_2T_z$, $Mo_2Ti_2C_3T_z$ and $Mo_2TiC_2T_z$, allowed us to uncover the relationships between the chemical composition (M=Ti vs Mo), layer structure (M_4C_3 vs M_3C_2), intrinsic microscopic conductivity, and the photoexcited carrier dynamics. We have established that while all three MXenes are metallic, replacing some of Ti with Mo significantly decreases free carrier density and changes response to photoexcitation from conductivity suppression to enhancement, demonstrating a wide range of properties that can be accessed by engineering the chemical composition. We have also demonstrated that charge carrier transport and optical properties in MXene films can be tuned by the presence of intercalated species in the van der Waals gaps. This work provides the framework for investigating other MXene chemistries and identifying MXenes that hold promise for various electronic and photonic applications. Here, we have proposed applications of $Ti_3C_2T_z$ in dynamically tunable THz electromagnetic interference shielding and in THz polarizers. Finally, this work lays the foundations for investigation of nonlinear properties of MXenes in THz frequency range. The list of MXenes that have been successfully fabricated grows rapidly, from one in 2011 to over 30 ten year later, and the experiments described in this thesis set the stage for applications of linear and nonlinear THz spectroscopy to elucidating their properties and identifying new avenues for MXene applications.

Appendix:

Simulation parameters for THz polarizer on COMSOL Multiphysics 5.5:

Name	Expression	Description
d_0	$500\ \mu m$	PML layer up
d_1	$500\ \mu m$	Up Air layer thickness
d_2	$200\ \mu m$	Substrate thickness
d_3	$500\ \mu m$	Down air thickness
d_4	$500\ \mu m$	PML layer down
N_L	10	Line number
f_{min}	0.2 THz	THz frequency range $[f_{min}, f_{max}]$, the resolution can be tuned with f_{step}
f_{step}	0.1 THz	
f_{max}	2.5 THz	
w	$20\ \mu m$	This is an example of the width, thickness, spacing of the MXene lines, where w, s are scanned from 5 to 40 μm, d is scanned in from 10 nm to 2 μm
d	$30\ \mu m$	
s	$10\ \mu m$	
c	-0.7	c parameter of Drude Smith model
N	$2 \times 10^{21}\ cm^{-3}$	Carrier density in MXene lines
τ_{DS}	6 fs	Carrier scattering time
m_{eff}	$m_e * 0.2845$	Carrier effective mass
E_x	$sin\ (\theta)$	Incident polarization of THz electrical field, which can be scanning $[0, \pi/2]$
E_y	$cos\ (\theta)$	

Publications during PhD program:

[1] **Guangjiang Li,** Kateryna Kushnir, Yongchang Dong, Sergii Chertopalov, Apparao M Rao, Vadym Mochalin, Ramakrishna Podila, Lyubov Titova. Equilibrium and non-equilibrium free carrier dynamics in two-dimensional $Ti_3C_2T_x$ MXenes: THz spectroscopy study, **2D Materials** (2018) (link)

[2] **Guangjiang Li,** Naaman Amer, Hassan A. Hafez, Shuohan Huang, Dmitry Turchinovich, Vadym N. Mochalin, Frank A. Hegmann, and Lyubov V. Titova. Dynamical control over Terahertz electromagnetic interference shielding with 2D $Ti_3C_2T_y$ MXene by ultrafast optical pulses, **Nano Letters,** (2019) (link)

[3] **Guangjiang Li,** Varun Natu, Teng Shi, Michel W. Barsoum, and Lyubov V. Titova**.** Two-dimensional MXenes $Mo_2Ti_2C_3T_z$ and $Mo_2TiC_2T_z$: Microscopic conductivity and dynamics of photoexcited carriers, **ACS Applied Energy Materials**, (2020) (link)

[4] **Guangjiang Li,** Kiana Montazeri, Mostafa K. Ismail, Michel W. Barsoum, Bahram Nabet, Lyubov V. Titova**.** Terahertz polarizers based on 2D $Ti_3C_2T_z$ MXene: spin cast from aqueous suspensions, **Advanced Photonics Research**, (2020) (link) (featured on inside cover)

[5] Kateryna Kushnir, Ying Qin, Yuxia Shen, **Guangjiang Li**, Benjamin M. Fregoso, Sefaattin Tongay, Lyubov V Titova. Ultrafast zero-bias surface photocurrent in Germanium Selenide: promise for Terahertz devices and photovoltaics, **ACS Applied Materials & Interfaces**, (2019) (link)

[6] Lite Zhou, Edan Bainglass, Maryam Masroor, Binod Giri, **Guangjiang Li**, Alexander Carl, Ronald L. Grimm, Muhammad N. Huda, Lyubov V. Titova and Pratap M. Rao. Synthesis and optoelectronic properties of a promising quaternary metal oxide light absorber $CuBiW_2O_8$. **J. Mater. Chem. A**, (2021) (link)

Conference presentations:

1. Poster: Equilibrium and non-equilibrium free carrier dynamics in 2D $Ti_3C_2T_x$ MXenes: THz spectroscopy study, **2017** MRS (Materials Research Society), Boston, MA
2. Poster: Zero-Valent Cu and Sn Intercalation into GeS Nanoribbons—Tailoring Ultrafast Photoconductive Response, **2018** MRS, Boston, MA
3. Poster: Free Carrier Dynamics in Two-Dimensional $Ti_3C_2T_x$ MXenes: THz Spectroscopy Study, **2019** OTST (Optical Terahertz Science and Technology), Santa Fe, NM
4. Oral presentation: Long-lived negative THz photoconductivity in $Ti_3C_2T_x$ MXene thin Film, **2019** New England Energy Research Forum, Worcester, MA
5. Oral presentation: Microscopic conductivity and ultrafast carrier dynamics in molybdenum-based MXenes: THz spectroscopy study, **2020** Photonics West, San Francisco, CA
6. Oral presentation: A Novel THz Electromagnetic Interference Shielding Material: 2D $Ti_3C_2T_y$ MXene, **2020** IRMMW-THz, Buffalo, NY(Online)

6 Reference

1. Naguib, M.; Mashtalir, O.; Carle, J.; Lu, J.; Hultman, L.; Gogotsi, Y.; Barsoum, M. W., Two-Dimensional Transition Metal Carbides. *ACS Nano* **2012,** *6*, 1322-1331.

2. Li, G.; Montazeri, K.; Ismail, M. K.; Barsoum, M. W.; Nabet, B.; Titova, L. V., Terahertz Polarizers Based on 2D Ti3C2Tz MXene: Spin Cast from Aqueous Suspensions. *Advanced Photonics Research* **2020,** *1* (2), 2000084.

3. Li, G.; Natu, V.; Shi, T.; Barsoum, M. W.; Titova, L. V., Two-Dimensional MXenes Mo2Ti2C3Tz and Mo2TiC2Tz: Microscopic Conductivity and Dynamics of Photoexcited Carriers. *ACS Applied Energy Materials* **2020,** *3* (2), 1530-1539.

4. Li, G.; Amer, N.; Hafez, H. A.; Huang, S.; Turchinovich, D.; Mochalin, V. N.; Hegmann, F. A.; Titova, L. V., Dynamical Control over Terahertz Electromagnetic Interference Shielding with 2D Ti3C2Ty MXene by Ultrafast Optical Pulses. *Nano Letters* **2019**.

5. Naguib, M.; Kurtoglu, M.; Presser, V.; Lu, J.; Niu, J. J.; Heon, M.; Hultman, L.; Gogotsi, Y.; Barsoum, M. W., Two-Dimensional Nanocrystals Produced by Exfoliation of Ti3AlC2. *Adv Mater* **2011,** *23* (37), 4248-4253.

6. Anasori, B.; Xie, Y.; Beidaghi, M.; Lu, J.; Hosler, B. C.; Hultman, L.; Kent, P. R. C.; Gogotsi, Y.; Barsoum, M. W., Two-Dimensional, Ordered, Double Transition Metals Carbides (MXenes). *ACS Nano* **2015,** *9* (10), 9507-9516.

7. Li, R. Y.; Zhang, L. B.; Shi, L.; Wang, P., MXene Ti3C2: An Effective 2D Light-to-Heat Conversion Material. *Acs Nano* **2017,** *11* (4), 3752-3759.

8. Li, L. F.; Wang, F.; Zhu, J. F.; Wu, W. L., The facile synthesis of layered Ti2C MXene/carbon nanotube composite paper with enhanced electrochemical properties. *Dalton T* **2017,** *46* (43), 14880-14887.

9. Anasori, B.; Shi, C. Y.; Moon, E. J.; Xie, Y.; Voigt, C. A.; Kent, P. R. C.; May, S. J.; Billinge, S. J. L.; Barsoum, M. W.; Gogotsi, Y., Control of electronic properties of 2D carbides (MXenes) by manipulating their transition metal layers. *Nanoscale Horiz* **2016,** *1* (3), 227-234.

10. Zhou, J.; Zha, X. H.; Chen, F. Y.; Ye, Q.; Eklund, P.; Du, S. Y.; Huang, Q., A Two-Dimensional Zirconium Carbide by Selective Etching of Al3C3 from Nanolaminated Zr3Al3C5. *Angew Chem Int Edit* **2016,** *55* (16), 5008-5013.

11. Zhang, M.; Chen, X. F.; Sui, J. Y.; Abraha, B. S.; Li, Y.; Peng, W. C.; Zhang, G. L.; Zhang, F. B.; Fan, X. B., Improving the performance of a titanium carbide MXene in supercapacitors by partial oxidation treatment. *Inorg Chem Front* **2020,** *7* (5), 1205-1211.

12. Shuck, C. E.; Sarycheva, A.; Anayee, M.; Levitt, A.; Zhu, Y. Z.; Uzun, S.; Balitskiy, V.; Zahorodna, V.; Gogotsi, O.; Gogotsi, Y., Scalable Synthesis of Ti3C2Tx MXene. *Adv Eng Mater* **2020,** *22* (3).

13. Eom, W.; Shin, H.; Ambade, R. B.; Lee, S. H.; Lee, K. H.; Kang, D. J.; Han, T. H., Large-scale wet-spinning of highly electroconductive MXene fibers. *Nat Commun* **2020,** *11* (1).

14. Zhao, X. F.; Vashisth, A.; Prehn, E.; Sun, W. M.; Shah, S.; Habib, T.; Chen, Y. X.; Tan, Z. Y.; Lutkenhaus, J.; Radovic, M.; Green, M. J., Antioxidants

Unlock Shelf-Stable Ti3C2Tx (MXene) Nanosheet Dispersions. *Matter* **2019,** *1* (2), 513-526.

15. Dong, Y.; Chertopalov, S.; Maleski, K.; Anasori, B.; Hu, L.; Bhattacharya, S.; Rao, A. M.; Gogotsi, Y.; Mochalin, V. N.; Podila, R., Saturable Absorption in 2D Ti_3C_2 MXene Thin Films for Passive Photonic Diodes. *Adv Mater* **2018,** *30* (10), 1705714.

16. Naguib, M.; Kurtoglu, M.; Presser, V.; Lu, J.; Niu, J.; Heon, M.; Hultman, L.; Gogotsi, Y.; Barsoum, M. W., Two Dimensional Nanocrystals Produced by Exfoliation of Ti3AlC2. *Advan. Mater.* **2011,** *23*, 4248-4253.

17. Naguib, M.; Mashtalir, O.; Carle, J.; Presser, V.; Lu, J.; Hultman, L.; Gogotsi, Y.; Barsoum, M. W., Two-Dimensional Transition Metal Carbides. *ACS Nano* **2012,** *6* (2), 1322-1331.

18. Verger, L.; Natu, V.; Carey, M.; Barsoum, M. W., MXenes: An Introduction of Their Synthesis, Select Properties, and Applications. *Trends in Chemistry* **2019**.

19. Khazaei, M.; Mishra, A.; Venkataramanan, N. S.; Singh, A. K.; Yunoki, S., Recent advances in MXenes: From fundamentals to applications. *Current Opinion in Solid State and Materials Science* **2019,** *23* (3), 164-178.

20. Naguib, M.; Mochalin, V. N.; Barsoum, M. W.; Gogotsi, Y., 25th Anniversary Article: MXenes: A New Family of Two-Dimensional Materials. *Adv. Mater.* **2014,** *26* (7), 992-1005.

21. Choi, G.; Shahzad, F.; Bahk, Y. M.; Jhon, Y. M.; Park, H.; Alhabeb, M.; Anasori, B.; Kim, D. S.; Koo, C. M.; Gogotsi, Y.; Seo, M., Enhanced Terahertz

Shielding of MXenes with Nano-Metamaterials. *Advanced Optical Materials* **2018,** *6* (5), 1701076.

22. Dillon, A. D.; Ghidiu, M. J.; Krick, A. L.; Griggs, J.; May, S. J.; Gogotsi, Y.; Barsoum, M. W.; Fafarman, A. T., Highly Conductive Optical Quality Solution-Processed Films of 2D Titanium Carbide. *Adv. Funct. Mater.* **2016,** *26* (23), 4162-4168.

23. Feng, W.; Luo, H.; Wang, Y.; Zeng, S.; Deng, L.; Zhou, X.; Zhang, H.; Peng, S., Ti3C2 MXene: a promising microwave absorbing material. *RSC Advances* **2018,** *8* (5), 2398-2403.

24. Jhon, Y. I.; Seo, M.; Jhon, Y. M., First-principles study of a MXene terahertz detector. *Nanoscale* **2018,** *10* (1), 69-75.

25. Shahzad, F.; Alhabeb, M.; Hatter, C. B.; Anasori, B.; Man Hong, S.; Koo, C. M.; Gogotsi, Y., Electromagnetic interference shielding with 2D transition metal carbides (MXenes). *Science* **2016,** *353* (6304), 1137-1140.

26. Zhang, C.; Anasori, B.; Seral-Ascaso, A.; Park, S. H.; McEvoy, N.; Shmeliov, A.; Duesberg, G. S.; Coleman, J. N.; Gogotsi, Y.; Nicolosi, V., Transparent, Flexible, and Conductive 2D Titanium Carbide (MXene) Films with High Volumetric Capacitance. *Adv. Mater.* **2017,** *29* (36), 1702678.

27. Li, G.; Kushnir, K.; Dong, Y.; Chertopalov, S.; Rao, A. M.; Mochalin, V. N.; Podila, R.; Titova, L. V., Equilibrium and non-equilibrium free carrier dynamics in 2D Ti 3 C 2 T x MXenes: THz spectroscopy study. *2D Materials* **2018,** *5* (3), 035043.

28. Hu, T.; Zhang, H.; Wang, J.; Li, Z.; Hu, M.; Tan, J.; Hou, P.; Li, F.; Wang, X., Anisotropic electronic conduction in stacked two-dimensional titanium carbide. *Scientific Reports* **2015,** *5*, 16329.

29. Khazaei, M.; Ranjbar, A.; Arai, M.; Sasaki, T.; Yunoki, S., Electronic properties and applications of MXenes: a theoretical review. *J. Mater. Chem. C* **2017,** *5* (10), 2488-2503.

30. Ibragimova, R.; Erhart, P.; Rinke, P.; Komsa, H. P., Surface Functionalization of 2D MXenes: Trends in Distribution, Composition, and Electronic Properties. *J Phys Chem Lett* **2021,** *12* (9), 2377-2384.

31. Xiong, K. W.; Wang, P. H.; Yang, G.; Liu, Z. F.; Zhang, H. J.; Jin, S. W.; Xu, X., Functional Group Effects on the Photoelectronic Properties of MXene (Sc2CT2, T = O, F, OH) and Their Possible Photocatalytic Activities. *Scientific Reports* **2017,** *7*.

32. Miranda, A.; Halim, J.; Barsoum, M. W.; Lorke, A., Electronic properties of freestanding Ti3C2Tx MXene monolayers. *Applied Physics Letters* **2016,** *108* (3).

33. Lipatov, A.; Alhabeb, M.; Lukatskaya, M. R.; Boson, A.; Gogotsi, Y.; Sinitskii, A., Effect of Synthesis on Quality, Electronic Properties and Environmental Stability of Individual Monolayer Ti3C2 MXene Flakes. *Adv Electron Mater* **2016,** *2* (12).

34. Lipatov, A.; Alhabeb, M.; Lu, H. D.; Zhao, S. S.; Loes, M. J.; Vorobeva, N. S.; Dall'Agnese, Y.; Gao, Y.; Gruverman, A.; Gogotsi, Y.; Sinitskii, A.,

Electrical and Elastic Properties of Individual Single-Layer Nb4C3Tx MXene Flakes. *Adv Electron Mater* **2020,** *6* (4).

35. Halim, J.; Moon, E. J.; Eklund, P.; Rosen, J.; Barsoum, M. W.; Ouisse, T., Variable range hopping and thermally activated transport in molybdenum-based MXenes. *Physical Review B* **2018,** *98* (10), 104202.

36. Hart, J. L.; Hantanasirisakul, K.; Lang, A. C.; Anasori, B.; Pinto, D.; Pivak, Y.; van Omme, J. T.; May, S. J.; Gogotsi, Y.; Taheri, M. L., Control of MXenes' electronic properties through termination and intercalation. *Nat Commun* **2019,** *10.*

37. Berdiyorov, G. R., Optical properties of functionalized Ti3C2T2 (T=F, O, OH) MXene: First-principles calculations. *Aip Adv* **2016,** *6* (5).

38. Ma, C. Y.; Huang, W. C.; Wang, Y. Z.; Adams, J.; Wang, Z. H.; Liu, J.; Song, Y. F.; Ge, Y. Q.; Guo, Z. Y.; Hu, L. P.; Zhang, H., MXene saturable absorber enabled hybrid mode-locking technology: a new routine of advancing femtosecond fiber lasers performance. *Nanophotonics-Berlin* **2020,** *9* (8), 2451-2458.

39. In, J. Y.; Joonhoi, K.; Babak, A.; Minah, S.; Han, L. J.; Yury, G.; Min, J. Y., Metallic MXene Saturable Absorber for Femtosecond Mode-Locked Lasers. *Adv Mater* **2017,** *29* (40), 1702496.

40. Sarycheva, A.; Polemi, A.; Liu, Y. L.; Dandekar, K.; Anasori, B.; Gogotsi, Y., 2D titanium carbide (MXene) for wireless communication. *Sci Adv* **2018,** *4* (9).

41. Zhao, S.; Zhang, H. B.; Luo, J. Q.; Wang, Q. W.; Xu, B.; Hong, S.; Yu, Z. Z., Highly Electrically Conductive Three-Dimensional Ti3C2TX MXene/Reduced Graphene Oxide Hybrid Aerogels with Excellent Electromagnetic Interference Shielding Performances. *Acs Nano* **2018,** *12* (11), 11193-11202.

42. Li, X. L.; Yin, X. W.; Liang, S.; Li, M. H.; Cheng, L. F.; Zhang, L. T., 2D carbide MXene Ti2CTX as a novel high-performance electromagnetic interference shielding material. *Carbon* **2019,** *146*, 210-217.

43. Zou, Q.; Guo, W. Y.; Zhang, L.; Yang, L. T.; Zhao, Z. Y.; Liu, F.; Ye, X.; Zhang, Y.; Shi, W. Z., MXene-based ultra-thin film for terahertz radiation shielding. *Nanotechnology* **2020,** *31* (50).

44. Choi, G.; Shahzad, F.; Bahk, Y. M.; Jhon, Y. M.; Park, H.; Alhabeb, M.; Anasori, B.; Kim, D. S.; Koo, C. M.; Gogotsi, Y.; Seo, M., Enhanced Terahertz Shielding of MXenes with Nano-Metamaterials. *Adv Opt Mater* **2018,** *6* (5).

45. Wu, Q.; Zhang, M.; Jin, X.; Chen, S.; Jiang, Q.; Jiang, X.; Zheng, Z.; Zhang, H., 104 fs mode-locked fiber laser with a MXene-based saturable absorber. *Conf Laser Electr* **2019**.

46. Yi, J.; Du, L.; Li, J.; Yang, L. L.; Hu, L. Y.; Huang, S. H.; Dong, Y. C.; Miao, L. L.; Wen, S. C.; Mochalin, V. N.; Zhao, C. J.; Rao, A. M., Unleashing the potential of Ti2CTx MXene as a pulse modulator for mid-infrared fiber lasers. *2d Mater* **2019,** *6* (4).

47. Huang, D. P.; Xie, Y.; Lu, D. Z.; Wang, Z. Y.; Wang, J. Y.; Yu, H. H.; Zhang, H. J., Demonstration of a White Laser with V2C MXene-Based Quantum Dots. *Adv Mater* **2019,** *31* (24).

48. Velusamy, D. B.; El-Demellawi, J. K.; El-Zohry, A. M.; Giugni, A.; Lopatin, S.; Hedhili, M. N.; Mansour, A. E.; Di Fabrizio, E.; Mohammed, O. F.; Alshareef, H. N., MXenes for Plasmonic Photodetection. *Adv Mater* **2019,** *31* (32).

49. Shahzad, F.; Alhabeb, M.; Hatter, C. B.; Anasori, B.; Hong, S. M.; Koo, C. M.; Gogotsi, Y., Electromagnetic interference shielding with 2D transition metal carbides (MXenes). *Science* **2016,** *353* (6304), 1137-1140.

50. Gamzina, D.; Li, X.; Hurd, C.; Tang, Y.; Huang, X. J.; Zheng, Y.; Himes, L.; Gonzalez, M.; Li, H. Y.; Pan, P.; Letizia, R.; Feng, J. J.; Luhmann, N. C.; Paoloni, C., Backward wave oscillator for high power generation at THz frequencies. *Proc Spie* **2017,** *10383.*

51. Paoloni, C.; Gamzina, D.; Letizia, R.; Zheng, Y.; Luhmann, N. C., Millimeter wave traveling wave tubes for the 21st Century. *J Electromagnet Wave* **2021,** *35* (5), 567-603.

52. Kumar, N.; Singh, U.; Bera, A.; Sinha, A. K., A review on the sub-THz/THz gyrotrons. *Infrared Phys Techn* **2016,** *76*, 38-51.

53. Tan, P.; Huang, J.; Liu, K. F.; Xiong, Y. Q.; Fan, M. W., Terahertz radiation sources based on free electron lasers and their applications. *Sci China Inform Sci* **2012,** *55* (1), 1-15.

54. Roben, B.; Lu, X.; Hempel, M.; Biermann, K.; Schrottke, L.; Grahn, H. T., Terahertz quantum-cascade lasers as high-power and wideband, gapless sources for spectroscopy. *Opt Express* **2017,** *25* (14), 16282-16290.

55. Heshmat, B.; Pahlevaninezhad, H.; Pang, Y. J.; Masnadi-Shirazi, M.; Lewis, R. B.; Tiedje, T.; Gordon, R.; Darcie, T. E., Nanoplasmonic Terahertz Photoconductive Switch on GaAs. *Nano Letters* **2012,** *12* (12), 6255-6259.

56. Burford, N. M.; El-Shenawee, M. O., Review of terahertz photoconductive antenna technology. *Opt Eng* **2017,** *56* (1).

57. Koulouklidis, A. D.; Gollner, C.; Shumakova, V.; Fedorov, V. Y.; Pugzlys, A.; Baltuska, A.; Tzortzakis, S., Observation of extremely efficient terahertz generation from mid-infrared two-color laser filaments. *Nat Commun* **2020,** *11* (1).

58. Wagner, H. P.; Kuhnelt, M.; Langbein, W.; Hvam, J. M., Dispersion of the second-order nonlinear susceptibility in ZnTe, ZnSe, and ZnS. *Physical Review B* **1998,** *58* (16), 10494-10501.

59. Ram, R. K.; Kushwaha, S. S.; Rajput, J. S., Optical Investigations of Lattice-Vibrations of Ii-Vi Compound Semiconductors. *J Phys Soc Jpn* **1989,** *58* (11), 4032-4040.

60. Blanchard, F.; Razzari, L.; Bandulet, H. C.; Sharma, G.; Morandotti, R.; Kieffer, J. C.; Ozaki, T.; Reid, M.; Tiedje, H. F.; Haugen, H. K.; Hegmann, F. A., Generation of 1.5 μJ single-cycle terahertz pulses by optical rectification from a large aperture ZnTe crystal. *Opt Express* **2007,** *15* (20), 13212-13220.

61. Hebling, J.; Yeh, K. L.; Hoffmann, M. C.; Bartal, B.; Nelson, K. A., Generation of high-power terahertz pulses by tilted-pulse-front excitation and their application possibilities. *J Opt Soc Am B* **2008,** *25* (7), B6-B19.

62. Cornet, M.; Degert, J.; Abraham, E.; Freysz, E., Terahertz-field-induced second harmonic generation through Pockels effect in zinc telluride crystal. *Opt Lett* **2014,** *39* (20), 5921-5924.

63. Wacker, A.; Bastard, G.; Carosella, F.; Ferreira, R.; Dupont, E., Unraveling of free-carrier absorption for terahertz radiation in heterostructures. *Physical Review B* **2011,** *84* (20).

64. Zhang, C.; Cao, J. C., Calculation of the nonlinear free-carrier absorption of terahertz radiation in semiconductor heterostructures. *Physical Review B* **2004,** *70* (19).

65. Kaindl, R. A.; Hagele, D.; Carnahan, M. A.; Chemla, D. S., Transient terahertz spectroscopy of excitons and unbound carriers in quasi-two-dimensional electron-hole gases. *Physical Review B* **2009,** *79* (4).

66. Xing, X.; Zhao, L. T.; Zhang, Z. Y.; Liu, X. K.; Zhang, K. L.; Yu, Y.; Lin, X.; Chen, H. Y.; Chen, J. Q.; Jin, Z. M.; Xu, J. H.; Ma, G. H., Role of Photoinduced Exciton in the Transient Terahertz Conductivity of Few-Layer WS2 Laminate. *J Phys Chem C* **2017,** *121* (37), 20451-20457.

67. Kampfrath, T.; Sell, A.; Klatt, G.; Pashkin, A.; Mahrlein, S.; Dekorsy, T.; Wolf, M.; Fiebig, M.; Leitenstorfer, A.; Huber, R., Coherent terahertz control of antiferromagnetic spin waves. *Nat Photonics* **2011,** *5* (1), 31-34.

68. Walowski, J.; Munzenberg, M., Perspective: Ultrafast magnetism and THz spintronics. *J Appl Phys* **2016,** *120* (14).

69. Yamaguchi, S.; Tominaga, K.; Saito, S., Intermolecular vibrational mode of the benzoic acid dimer in solution observed by terahertz time-domain spectroscopy. *Phys Chem Chem Phys* **2011,** *13* (32), 14742-14749.

70. Kozina, M.; Fechner, M.; Marsik, P.; van Driel, T.; Glownia, J. M.; Bernhard, C.; Radovic, M.; Zhu, D.; Bonetti, S.; Staub, U.; Hoffmann, M. C., Terahertz-driven phonon upconversion in SrTiO3. *Nat Phys* **2019,** *15* (4), 387-+.

71. Vicario, C.; Trisorio, A.; Allenspach, S.; Ruegg, C.; Giorgianni, F., Narrow-band and tunable intense terahertz pulses for mode-selective coherent phonon excitation. *Applied Physics Letters* **2020,** *117* (10).

72. Ghalgaoui, A.; Fingerhut, B. P.; Reimann, K.; Elsaesser, T.; Woerner, M., Terahertz Polaron Oscillations of Electrons Solvated in Liquid Water. *Phys Rev Lett* **2021,** *126* (9).

73. Joyce, H. J.; Boland, J. L.; Davies, C. L.; Baig, S. A.; Johnston, M. B., A review of the electrical properties of semiconductor nanowires: insights gained from terahertz conductivity spectroscopy. *Semicond Sci Tech* **2016,** *31* (10).

74. Unuma, T.; Fujii, K.; Kishida, H.; Nakamura, A., Terahertz complex conductivities of carriers with partial localization in doped polythiophenes. *Applied Physics Letters* **2010,** *97* (3).

75. Smith, N., Classical generalization of the Drude formula for the optical conductivity. *Physical Review B* **2001,** *64* (15).

76. Cocker, T. L.; Titova, L. V.; Fourmaux, S.; Bandulet, H. C.; Brassard, D.; Kieffer, J. C.; El Khakani, M. A.; Hegmann, F. A., Terahertz conductivity of the metal-insulator transition in a nanogranular VO2 film. *Applied Physics Letters* **2010,** *97* (22).

77. Butler, K. T.; Dringoli, B. J.; Zhou, L.; Rao, P. M.; Walsh, A.; Titova, L. V., Ultrafast carrier dynamics in BiVO4 thin film photoanode material: interplay between free carriers, trapped carriers and low-frequency lattice vibrations. *J. Mater. Chem. A* **2016,** *4* (47), 18516-18523.

78. Cocker, T. L.; Baillie, D.; Buruma, M.; Titova, L. V.; Sydora, R. D.; Marsiglio, F.; Hegmann, F. A., Microscopic Origin of the Drude-Smith Model. *Physical Review B* **2017,** *96* (20), 205439.

79. Jensen, S. A.; Ulbricht, R.; Narita, A.; Feng, X.; Mullen, K.; Hertel, T.; Turchinovich, D.; Bonn, M., Ultrafast photoconductivity of graphene nanoribbons and carbon nanotubes. *Nano Lett* **2013,** *13* (12), 5925-30.

80. Guglietta, G. W.; Diroll, B. T.; Gaulding, E. A.; Fordham, J. L.; Li, S.; Murray, C. B.; Baxter, J. B., Lifetime, Mobility, and Diffusion of Photoexcited Carriers in Ligand-Exchanged Lead Selenide Nanocrystal Films Measured by Time-Resolved Terahertz Spectroscopy. *Acs Nano* **2015,** *9* (2), 1820-1828.

81. Richter, C.; Schmuttenmaer, C. A., Exciton-like trap states limit electron mobility in TiO_2 nanotubes. *Nature Nanotechnology* **2010,** *5*, 769.

82. Alberding, B. G.; DeSario, P. A.; So, C. R.; Dunkelberger, A. D.; Rolison, D. R.; Owrutsky, J. C.; Heilweil, E. J., Static and Time-Resolved Terahertz

Measurements of Photoconductivity in Solution-Deposited Ruthenium Dioxide Nanofilms. *Journal of Physical Chemistry C* **2017,** *121* (7), 4037-4044.

83. Alberding, B. G.; Kushto, G. P.; Lane, P. A.; Heilweil, E. J., Reduced photoconductivity observed by time-resolved terahertz spectroscopy in metal nanofilms with and without adhesion layers. *Applied Physics Letters* **2016,** *108* (22).

84. Walther, M.; Cooke, D. G.; Sherstan, C.; Hajar, M.; Freeman, M. R.; Hegmann, F. A., Terahertz conductivity of thin gold films at the metal-insulator percolation transition. *Physical Review B* **2007,** *76* (12).

85. Titova, L. V.; Cocker, T. L.; Cooke, D. G.; Wang, X.; Meldrum, A.; Hegmann, F. A., Ultrafast percolative transport dynamics in silicon nanocrystal films. *Physical Review B* **2011,** *83* (8).

86. Cooke, D. G.; Meldrum, A.; Uhd Jepsen, P., Ultrabroadband terahertz conductivity of Si nanocrystal films. *Applied Physics Letters* **2012,** *101* (21), 211107.

87. Dadrasnia, E.; Lamela, H.; Kuppam, M. B.; Garet, F.; Coutaz, J. L., Determination of the DC Electrical Conductivity of Multiwalled Carbon Nanotube Films and Graphene Layers from Noncontact Time-Domain Terahertz Measurements. *Adv Cond Matter Phys* **2014,** *2014*.

88. Whelan, P. R.; Zhou, B. B.; Bezencenet, O.; Shivayogimath, A.; Mishra, N.; Shen, Q.; Jessen, B. S.; Pasternak, I.; Mackenzie, D. M. A.; Ji, J.; Sun, C. Z.; Seneor, P.; Dlubak, B.; Luo, B. R.; Osterberg, F. W.; Huang, D. P.; Shi, H. F.; Luo, D.; Wang, M. H.; Ruoff, R. S.; Conran, B.; McAleese, C.;

Huyghebaert, C.; Brems, S.; Booth, T. J.; Napal, I.; Strupinski, W.; Petersen, D. H.; Forti, S.; Coletti, C.; Jouvray, A.; Teo, K. B. K.; Centeno, A.; Zurutuza, A.; Legagneux, P.; Jepsen, P. U.; Boggild, P., Case studies of electrical characterisation of graphene by terahertz time-domain spectroscopy. *2d Materials* **2021,** *8* (2).

89. Cocker, T. L.; Baillie, D.; Buruma, M.; Titova, L. V.; Sydora, R. D.; Marsiglio, F.; Hegmann, F. A., Microscopic origin of the Drude-Smith model. *Phys Rev B* **2017,** *96* (20).

90. Lloyd-Hughes, J.; Jeon, T.-I., A Review of the Terahertz Conductivity of Bulk and Nano-Materials. *Journal of Infrared, Millimeter, and Terahertz Waves* **2012,** *33* (9), 871-925.

91. Mathis, T. S.; Maleski, K.; Goad, A.; Sarycheva, A.; Anayee, M.; Foucher, A. C.; Hantanasirisakul, K.; Shuck, C. E.; Stach, E. A.; Gogotsi, Y., Modified MAX Phase Synthesis for Environmentally Stable and Highly Conductive Ti3C2 MXene. *Acs Nano* **2021,** *15* (4), 6420-6429.

92. Ghidiu, M.; Lukatskaya, M. R.; Zhao, M.-Q.; Gogotsi, Y.; Barsoum, M. W., Conductive two-dimensional titanium carbide ‘clay’ with high volumetric capacitance. *Nature* **2014,** *516*, 78.

93. Jepsen, P. U.; Cooke, D. G.; Koch, M., Terahertz Spectroscopy and Imaging–Modern Techniques and Applications. *Laser & Photonics Reviews* **2011,** *5* (1), 124-166.

94. Miranda, A.; Halim, J.; Barsoum, M. W.; Lorke, A., Electronic properties of freestanding $Ti_3C_2T_x$ MXene monolayers. *Applied Physics Letters* **2016,** *108* (3), 033102.

95. Mics, Z.; D'Angio, A.; Jensen, S. A.; Bonn, M.; Turchinovich, D., Density-dependent electron scattering in photoexcited GaAs in strongly diffusive regime. *Applied Physics Letters* **2013,** *102* (23), 231120.

96. Demsar, J.; Dekorsy, T., Carrier dynamics in bulk semiconductors and metals after ultrashort pulse excitation. In *Optical Techniques for Solid-State Materials Characterization*, 2016; pp 291-328.

97. Block, A.; Liebel, M.; Yu, R.; Spector, M.; Sivan, Y.; García de Abajo, F. J.; van Hulst, N. F., Tracking ultrafast hot-electron diffusion in space and time by ultrafast thermomodulation microscopy. *Science Advances* **2019,** *5* (5), eaav8965.

98. Smith, A. N.; Norris, P. M., Influence of intraband transitions on the electron thermoreflectance response of metals. *Applied Physics Letters* **2001,** *78* (9), 1240-1242.

99. Averitt, R. D.; Lobad, A. I.; Kwon, C.; Trugman, S. A.; Thorsmølle, V. K.; Taylor, A. J., Ultrafast Conductivity Dynamics in Colossal Magnetoresistance Manganites. *Phys Rev Lett* **2001,** *87* (1), 017401.

100. Hohlfeld, J.; Wellershoff, S. S.; Güdde, J.; Conrad, U.; Jähnke, V.; Matthias, E., Electron and lattice dynamics following optical excitation of metals. *Chemical Physics* **2000,** *251* (1), 237-258.

101. Ivanov, I.; Bonn, M.; Mics, Z.; Turchinovich, D., Perspective on terahertz spectroscopy of graphene. *EPL (Europhysics Letters)* **2015,** *111* (6), 67001.

102. Jnawali, G.; Rao, Y.; Yan, H.; Heinz, T. F., Observation of a transient decrease in terahertz conductivity of single-layer graphene induced by ultrafast optical excitation. *Nano Lett* **2013,** *13* (2), 524-30.

103. Jensen, S. A.; Mics, Z.; Ivanov, I.; Varol, H. S.; Turchinovich, D.; Koppens, F. H. L.; Bonn, M.; Tielrooij, K. J., Competing Ultrafast Energy Relaxation Pathways in Photoexcited Graphene. *Nano Letters* **2014,** *14* (10), 5839-5845.

104. Hintermayr, V. A.; Polavarapu, L.; Urban, A. S.; Feldmann, J., Accelerated Carrier Relaxation through Reduced Coulomb Screening in Two-Dimensional Halide Perovskite Nanoplatelets. *Acs Nano* **2018,** *12* (10), 10151-10158.

105. Gholivand, H.; Fuladi, S.; Hemmat, Z.; Salehi-Khojin, A.; Khalili-Araghi, F., Effect of surface termination on the lattice thermal conductivity of monolayer Ti3C2Tz MXenes. *J Appl Phys* **2019,** *126* (6), 065101.

106. Chen, L.; Shi, X.; Yu, N.; Zhang, X.; Du, X.; Lin, J., Measurement and Analysis of Thermal Conductivity of Ti3C2Tx MXene Films. *Materials* **2018,** *11* (9), 1701.

107. Liu, R.; Li, W., High-Thermal-Stability and High-Thermal-Conductivity Ti3C2Tx MXene/Poly(vinyl alcohol) (PVA) Composites. *ACS Omega* **2018,** *3* (3), 2609-2617.

108. Hemmat, Z.; Yasaei, P.; Schultz, J. F.; Hong, L.; Majidi, L.; Behranginia, A.; Verger, L.; Jiang, N.; Barsoum, M. W.; Klie, R. F.; Salehi-Khojin, A., Tuning

Thermal Transport Through Atomically Thin Ti3C2Tz MXene by Current Annealing in Vacuum. *Adv. Funct. Mater.* **2019,** *29* (19), 1805693.

109. Halim, J.; Lukatskaya, M. R.; Cook, K. M.; Lu, J.; Smith, C. R.; Näslund, L.-Å.; May, S. J.; Hultman, L.; Gogotsi, Y.; Eklund, P.; Barsoum, M. W., Transparent Conductive Two-Dimensional Titanium Carbide Epitaxial Thin Films. *Chem. Mater.* **2014,** *26* (7), 2374-2381.

110. Hart, J. L.; Hantanasirisakul, K.; Lang, A. C.; Anasori, B.; Pinto, D.; Pivak, Y.; van Omme, J. T.; May, S. J.; Gogotsi, Y.; Taheri, M. L., Control of MXenes' electronic properties through termination and intercalation. *Nature Communications* **2019,** *10* (1), 522.

111. Berdiyorov, G. R., Effect of surface functionalization on the electronic transport properties of Ti3C2 MXene. *EPL (Europhysics Letters)* **2015,** *111* (6), 67002.

112. Persson, I.; Näslund, L.-Å.; Halim, J.; Barsoum, M. W.; Darakchieva, V.; Palisaitis, J.; Rosen, J.; Persson, P. O. Å., On the organization and thermal behavior of functional groups on Ti3C2 MXene surfaces in vacuum. *2D Materials* **2017,** *5* (1), 015002.

113. Schultz, T.; Frey, N. C.; Hantanasirisakul, K.; Park, S.; May, S. J.; Shenoy, V. B.; Gogotsi, Y.; Koch, N., Surface Termination Dependent Work Function and Electronic Properties of Ti3C2Tx MXene. *Chemistry of Materials* **2019**.

114. Karlsson, L. H.; Birch, J.; Halim, J.; Barsoum, M. W.; Persson, P. O. Å., Atomically Resolved Structural and Chemical Investigation of Single MXene Sheets. *Nano Letters* **2015,** *15* (8), 4955-4960.

115. Huang, S.; Mochalin, V. N., Hydrolysis of 2D Transition-Metal Carbides (MXenes) in Colloidal Solutions. *Inorganic Chemistry* **2019,** *58* (3), 1958-1966.

116. Bai, Y.; Zhou, K.; Srikanth, N.; Pang, J. H. L.; He, X.; Wang, R., Dependence of elastic and optical properties on surface terminated groups in two-dimensional MXene monolayers: a first-principles study. *RSC Advances* **2016,** *6* (42), 35731-35739.

117. Halim, J.; Kota, S.; Lukatskaya, M. R.; Naguib, M.; Zhao, M.-Q.; Moon, E. J.; Pitock, J.; Nanda, J.; May, S. J.; Gogotsi, Y.; Barsoum, M. W., Synthesis and Characterization of 2D Molybdenum Carbide (MXene). *Adv. Funct. Mater.* **2016,** *26* (18), 3118-3127.

118. Anasori, B.; Shi, C.; Moon, E. J.; Xie, Y.; Voigt, C. A.; Kent, P. R. C.; May, S. J.; Billinge, S. J. L.; Barsoum, M. W.; Gogotsi, Y., Control of electronic properties of 2D carbides (MXenes) by manipulating their transition metal layers. *Nanoscale Horizons* **2016,** *1* (3), 227-234.

119. Khazaei, M.; Ranjbar, A.; Arai, M.; Yunoki, S., Topological insulators in the ordered double transition metals $M_2'M''C_2$ MXenes (M'=Mo, W; M''=Ti, Zr, Hf). *Physical Review B* **2016,** *94* (12), 125152.

120. Halim, J.; Persson, I.; Moon, E. J.; Kühne, P.; Darakchieva, V.; Persson, P. O. Å.; Eklund, P.; Rosen, J.; Barsoum, M. W., Electronic and optical

characterization of 2D Ti2C and Nb2C (MXene) thin films. *Journal of Physics: Condensed Matter* **2019,** *31* (16), 165301.

121. Ouisse, T.; Barsoum, M. W., Magnetotransport in the MAX phases and their 2D derivatives: MXenes. *Materials Research Letters* **2017,** *5* (6), 365-378.

122. Baxter, J. B.; Schmuttenmaer, C. A., Conductivity of ZnO nanowires, nanoparticles, and thin films using time-resolved terahertz spectroscopy. *Journal of Physical Chemistry B* **2006,** *110* (50), 25229-25239.

123. Halim, J.; Cook, K. M.; Eklund, P.; Rosen, J.; Barsoum, M. W., XPS of cold pressed multilayered and freestanding delaminated 2D thin films of Mo2TiC2Tz and Mo2Ti2C3Tz (MXenes). *Applied Surface Science* **2019,** *494*, 1138-1147.

124. Sharma, G.; Al-Naib, I.; Hafez, H.; Morandotti, R.; Cooke, D. G.; Ozaki, T., Carrier density dependence of the nonlinear absorption of intense THz radiation in GaAs. *Opt Express* **2012,** *20* (16), 18016-18024.

125. Ma, J.; Shrestha, R.; Adelberg, J.; Yeh, C.-Y.; Hossain, Z.; Knightly, E.; Jornet, J. M.; Mittleman, D. M., Security and eavesdropping in terahertz wireless links. *Nature* **2018,** *563* (7729), 89-93.

126. Kürner, T.; Priebe, S., Towards THz Communications - Status in Research, Standardization and Regulation. *Journal of Infrared, Millimeter, and Terahertz Waves* **2014,** *35* (1), 53-62.

127. Akyildiz, I. F.; Jornet, J. M.; Han, C., Terahertz band: Next frontier for wireless communications. *Physical Communication* **2014,** *12*, 16-32.

128. Federici, J.; Moeller, L., Review of terahertz and subterahertz wireless communications. *J Appl Phys* **2010,** *107* (11), 111101.

129. Seo, M. A.; Yim, J. H.; Ahn, Y. H.; Rotermund, F.; Kim, D. S.; Lee, S.; Lim, H., Terahertz electromagnetic interference shielding using single-walled carbon nanotube flexible films. *Applied Physics Letters* **2008,** *93* (23), 231905.

130. Liu, L.; Das, A.; Megaridis, C. M., Terahertz shielding of carbon nanomaterials and their composites – A review and applications. *Carbon* **2014,** *69*, 1-16.

131. Dressel, M.; Grüner, G., *Electrodynamics of Solids: Optical Properties of Electrons in Matter*. Cambridge University Press: Cambridge, 2002.

132. Kamysbayev, V.; Filatov, A. S.; Hu, H. C.; Rui, X.; Lagunas, F.; Wang, D.; Klie, R. F.; Talapin, D. V., Covalent surface modifications and superconductivity of two-dimensional metal carbide MXenes. *Science* **2020,** *369* (6506), 979-+.

133. Mittleman, D. M., Frontiers in terahertz sources and plasmonics. *Nature Photonics* **2013,** *7* (9), 666-669.

134. Tonouchi, M., Cutting-edge terahertz technology. *Nat Photonics* **2007,** *1* (2), 97-105.

135. Yan, F.; Yu, C.; Park, H.; Parrott, E. P. J.; Pickwell-MacPherson, E., Advances in Polarizer Technology for Terahertz Frequency Applications. *Journal of Infrared, Millimeter, and Terahertz Waves* **2013,** *34* (9), 489-499.

136. Yamada, I.; Takano, K.; Hangyo, M.; Saito, M.; Watanabe, W., Terahertz wire-grid polarizers with micrometer-pitch Al gratings. *Opt Lett* **2009,** *34* (3), 274-276.

137. Huang, Z.; Parrott, E. P. J.; Park, H.; Chan, H. P.; Pickwell-MacPherson, E., High extinction ratio and low transmission loss thin-film terahertz polarizer with a tunable bilayer metal wire-grid structure. *Opt Lett* **2014,** *39* (4), 793-796.

138. Partanen, A.; Väyrynen, J.; Hassinen, S.; Tuovinen, H.; Mutanen, J.; Itkonen, T.; Silfsten, P.; Pääkkönen, P.; Kuittinen, M.; Mönkkönen, K.; Venäläinen, T., Fabrication of terahertz wire-grid polarizers. *Appl. Opt.* **2012,** *51* (35), 8360-8365.

139. Deng, L. Y.; Teng, J. H.; Zhang, L.; Wu, Q. Y.; Liu, H.; Zhang, X. H.; Chua, S. J., Extremely high extinction ratio terahertz broadband polarizer using bilayer subwavelength metal wire-grid structure. *Applied Physics Letters* **2012,** *101* (1), 011101.

140. Takano, K.; Yokoyama, H.; Ichii, A.; Morimoto, I.; Hangyo, M., Wire-grid polarizer sheet in the terahertz region fabricated by nanoimprint technology. *Opt Lett* **2011,** *36* (14), 2665-2667.

141. Ferraro, A.; Zografopoulos, D. C.; Missori, M.; Peccianti, M.; Caputo, R.; Beccherelli, R., Flexible terahertz wire grid polarizer with high extinction ratio and low loss. *Opt Lett* **2016,** *41* (9), 2009-2012.

142. Ren, L.; Pint, C. L.; Arikawa, T.; Takeya, K.; Kawayama, I.; Tonouchi, M.; Hauge, R. H.; Kono, J., Broadband terahertz polarizers with ideal

performance based on aligned carbon nanotube stacks. *Nano Lett* **2012,** *12* (2), 787-90.

143. Ren, L.; Pint, C. L.; Booshehri, L. G.; Rice, W. D.; Wang, X.; Hilton, D. J.; Takeya, K.; Kawayama, I.; Tonouchi, M.; Hauge, R. H.; Kono, J., Carbon Nanotube Terahertz Polarizer. *Nano Letters* **2009,** *9* (7), 2610-2613.

144. Kyoung, J.; Jang, E. Y.; Lima, M. D.; Park, H.-R.; Robles, R. O.; Lepró, X.; Kim, Y. H.; Baughman, R. H.; Kim, D.-S., A Reel-Wound Carbon Nanotube Polarizer for Terahertz Frequencies. *Nano Letters* **2011,** *11* (10), 4227-4231.

145. Xiang, W.; Huang, X.; Li, D.; Zhou, Q.; Guo, H.; Li, J., High extinction ratio terahertz broadband polarizer based on the aligned Ni nanowire arrays. *Opt Lett* **2020,** *45* (7), 1978-1981.

146. Baig, S. A.; Boland, J. L.; Damry, D. A.; Tan, H. H.; Jagadish, C.; Joyce, H. J.; Johnston, M. B., An Ultrafast Switchable Terahertz Polarization Modulator Based on III–V Semiconductor Nanowires. *Nano Letters* **2017,** *17* (4), 2603-2610.

147. Hu, H.; Hua, T., An easily manipulated protocol for patterning of MXenes on paper for planar micro-supercapacitors. *Journal of Materials Chemistry A* **2017,** *5* (37), 19639-19648.

148. Xu, B.; Zhu, M.; Zhang, W.; Zhen, X.; Pei, Z.; Xue, Q.; Zhi, C.; Shi, P., Ultrathin MXene-Micropattern-Based Field-Effect Transistor for Probing Neural Activity. *Adv Mater* **2016,** *28* (17), 3333-3339.

149. Montazeri, K.; Currie, M.; Verger, L.; Dianat, P.; Barsoum, M. W.; Nabet, B., Beyond Gold: Spin-Coated Ti_3C_2-Based MXene Photodetectors. *Adv. Mater.* **2019,** *31* (43), 1903271.

150. Grischkowsky, D.; Keiding, S.; van Exter, M.; Fattinger, C., Far-infrared time-domain spectroscopy with terahertz beams of dielectrics and semiconductors. *J. Opt. Soc. Am. B* **1990,** *7* (10), 2006-2015.

151. Li, G.; Natu, V.; Shi, T.; Barsoum, M. W.; Titova, L. V., Two-Dimensional MXenes $Mo_2Ti_2C_3T_z$ and $Mo_2TiC_2T_z$: Microscopic Conductivity and Dynamics of Photoexcited Carriers. *ACS Applied Energy Materials* **2020**.

152. Kampfrath, T.; Sell, A.; Klatt, G.; Pashkin, A.; Mährlein, S.; Dekorsy, T.; Wolf, M.; Fiebig, M.; Leitenstorfer, A.; Huber, R., Coherent terahertz control of antiferromagnetic spin waves. *Nat Photonics* **2011,** *5* (1), 31-34.

153. Li, X.; Qiu, T.; Zhang, J.; Baldini, E.; Lu, J.; Rappe, A. M.; Nelson, K. A., Terahertz field–induced ferroelectricity in quantum paraelectric SrTiO<sub>3</sub>. *Science* **2019,** *364* (6445), 1079-1082.

154. Shimano, R.; Watanabe, S.; Matsunaga, R., Intense Terahertz Pulse-Induced Nonlinear Responses in Carbon Nanotubes. *Journal of Infrared, Millimeter, and Terahertz Waves* **2012,** *33* (8), 861-869.

155. Salén, P.; Basini, M.; Bonetti, S.; Hebling, J.; Krasilnikov, M.; Nikitin, A. Y.; Shamuilov, G.; Tibai, Z.; Zhaunerchyk, V.; Goryashko, V., Matter manipulation with extreme terahertz light: Progress in the enabling THz technology. *Physics Reports* **2019,** *836-837*, 1-74.

156. Hafez, H. A.; Kovalev, S.; Deinert, J.-C.; Mics, Z.; Green, B.; Awari, N.; Chen, M.; Germanskiy, S.; Lehnert, U.; Teichert, J.; Wang, Z.; Tielrooij, K.-J.; Liu, Z.; Chen, Z.; Narita, A.; Müllen, K.; Bonn, M.; Gensch, M.; Turchinovich,

D., Extremely efficient terahertz high-harmonic generation in graphene by hot Dirac fermions. *Nature* **2018,** *561* (7724), 507-511.

157. Zhang, B. L.; Li, S. Q.; Chai, S. S.; Wu, X. H.; Ma, J. L.; Chen, L. M.; Li, Y. T., Nonlinear distortion and spatial dispersion of intense terahertz generation in lithium niobate via the tilted pulse front technique. *Photonics Res* **2018,** *6* (10), 959-964.

158. Stepanov, A. G.; Bonacina, L.; Chekalin, S. V.; Wolf, J.-P., Generation of 30 μJ single-cycle terahertz pulses at 100 Hz repetition rate by optical rectification. *Opt Lett* **2008,** *33* (21), 2497-2499.

159. Ibrahim, A.; Férachou, D.; Sharma, G.; Singh, K.; Kirouac-Turmel, M.; Ozaki, T., Ultra-high dynamic range electro-optic sampling for detecting millimeter and sub-millimeter radiation. *Scientific Reports* **2016,** *6* (1), 23107.

160. Hoffmann, M. C.; Turchinovich, D., Semiconductor saturable absorbers for ultrafast terahertz signals. *Applied Physics Letters* **2010,** *96* (15), 151110.

161. Gu, B.; Fan, Y.-X.; Wang, J.; Chen, J.; Ding, J.; Wang, H.-T.; Guo, B., Characterization of saturable absorbers using an open-aperture gaussian-beam Z scan. *Physical Review A* **2006,** *73.*

162. Wen, H.; Wiczer, M.; Lindenberg, A. M., Ultrafast electron cascades in semiconductors driven by intense femtosecond terahertz pulses. *Physical Review B* **2008,** *78* (12), 125203.